



HAL
open science

Magneto-inertial navigation: principles and application to an indoor pedometer

Eric Dorveaux

► **To cite this version:**

Eric Dorveaux. Magneto-inertial navigation: principles and application to an indoor pedometer. Automatic. École Nationale Supérieure des Mines de Paris, 2011. English. NNT : 2011ENMP0062 . pastel-00677137

HAL Id: pastel-00677137

<https://pastel.hal.science/pastel-00677137>

Submitted on 7 Mar 2012

HAL is a multi-disciplinary open access archive for the deposit and dissemination of scientific research documents, whether they are published or not. The documents may come from teaching and research institutions in France or abroad, or from public or private research centers.

L'archive ouverte pluridisciplinaire **HAL**, est destinée au dépôt et à la diffusion de documents scientifiques de niveau recherche, publiés ou non, émanant des établissements d'enseignement et de recherche français ou étrangers, des laboratoires publics ou privés.

École doctorale n°432: Sciences des Métiers de l'Ingénieur (SMI)

Doctorat ParisTech

T H È S E

pour obtenir le grade de docteur délivré par

l'École Nationale Supérieure des Mines de Paris

Spécialité "Mathématique et Automatique"

présentée et soutenue publiquement par

Éric DORVEAUX

le 10 novembre 2011

Navigation Magnéto-Inertielle
Principes et application à un système podométrique indoor

Directeur de thèse: **Nicolas PETIT**

Jury

M. Pascal MORIN, Chargé de recherche HDR, INRIA

M. Carlos SILVESTRE, Professeur, Instituto Superior Tecnico et Université de Macau

M. Simon LACROIX, Directeur de recherche, CNRS, LAAS

Mme Françoise LAMNABHI-LAGARRIGUE, Directeur de recherche, CNRS, LSS

M. Alain RIONDET, Ingénieur, DGA

M. Nicolas PETIT, Professeur, MINES ParisTech

Mme Sylvie LAMY, Ingénieur, CEA-LIST

M. David VISSIÈRE, Docteur, SYSNAV

Rapporteur

Rapporteur

Examineur

Examinatrice

Examineur

Directeur de thèse

Invitée

Invité

MINES ParisTech

Centre Automatique et Systèmes (CAS)

60, Bd Saint Michel - 75006 Paris - France

**T
H
È
S
E**

Graduate School n°432: Sciences des Métiers de l'Ingénieur (SMI)

ParisTech

PHD THESIS

To obtain the Doctor's degree from

École Nationale Supérieure des Mines de Paris

Speciality "Mathématique et Automatique"

defended in public by

Éric DORVEAUX

on November 10th, 2011

Magneto-Inertial Navigation
Principles and application to an indoor pedometer

Thesis advisor: **Nicolas PETIT**

Comitee

M. Pascal MORIN, Chargé de recherche HDR, INRIA
M. Carlos SILVESTRE, Professor, Instituto Superior Tecnico and University of Macau
M. Simon LACROIX, Directeur de recherche, CNRS, LAAS
Mme Françoise LAMNABHI-LAGARRIGUE, Directeur de recherche, CNRS, LSS
M. Alain RIONDET, Engineer, DGA
M. Nicolas PETIT, Professor, MINES ParisTech
Mme Sylvie LAMY, Engineer, CEA-LIST
M. David VISSIÈRE, Doctor, SYSNAV

Referee
Referee
Examiner
Examiner
Examiner
Advisor
Guest
Guest

MINES ParisTech
Centre Automatique et Système (CAS)
60, Bd Saint Michel - 75006 Paris - France

**T
H
È
S
E**

ÉRIC DORVEAUX

Centre Automatique et Systèmes
Unité Mathématiques et Systèmes
MINES ParisTech
60 bd St Michel 75272 Paris Cedex 06
France.

E-mail: eric.dorveaux@mines-paris.org

Key words. - inertial navigation, indoor navigation, indoor positioning

Mots clés. - navigation inertielle, navigation dans les bâtiments, positionnement dans les bâtiments

November 10th, 2011

À ma famille

Remerciements

Je voudrais en premier lieu remercier ici mon directeur de thèse, Nicolas Petit de m'avoir confié cette thèse il y a 3 ans. Toujours disponible, Nicolas a su grâce à son écoute, ses conseils, son sens pratique et son inébranlable enthousiasme, me soutenir et me guider durant ces trois années.

Je tiens également à remercier particulièrement David qui m'a laissé un domaine de recherche passionnant, à la suite de sa thèse, et m'a soutenu tout au long de ces années. J'aurai plaisir à continuer l'aventure Sysnav avec eux deux, Pierre-Jean, Quentin, Mathieu et tous ceux qui sont impliqués dans le développement de l'entreprise.

I wish to thank Professor Carlos Silvestre and Pascal Morin for the great interest they showed about my work by accepting to review the manuscript and for their precise and constructive remarks. A special thank to Carlos Silvestre who came all along from Macau for my defense. Je souhaite également remercier Simon Lacroix, Françoise Lammabhi-Lagarrigue, Alain Riondet et Sylvie Lamy de l'intérêt qu'ils ont porté à mon travail en acceptant de participer à mon jury.

Je remercie également les différents chercheurs du Centre Automatique et Systèmes, Pierre, Laurent, Philippe et Jean, ainsi qu'Alain à la DGA pour leur lumières sur certains sujets et pour leurs conseils scientifiques.

Je tiens à remercier Quentin pour son aide précieuse sur l'électronique embarquée dans les différents versions des prototypes tout au long de ma thèse, et Mathieu, qui, avec un regard neuf sur la magnéto-inertie, a su me poser les questions pertinentes.

Merci aux doctorants Pierre-Jean, Caroline et Florent qui m'ont épaulé durant ces années. J'avais plaisir à vous retrouver tous les jours. Merci à tous les membres du CAS et de Sysnav, que j'aurai plaisir à retrouver bientôt, pour leur soutien, et pour les moments partagés aux Mines, à Aubevoye, Madère, Shanghai, San Francisco ou ailleurs, ou simplement autour d'un baby-foot : Paul, Delphine, Nadège, Zaki, Erwan, Nicolas, Flavien, Emi, Manu, Georges, Pierre, Hadis, Lionel, Stéphane, Thomas, François, Alain,.

Je souhaite également remercier les stagiaires dont j'ai pu suivre une partie du travail, Thomas et Augustin.

J'ai une pensée pour les membres du projet Locindoor qui ont suivi avec bienveillance l'évolution de mes travaux.

Enfin, j'ai une attention particulière pour toute ma famille qui m'a, entre autre, toujours soutenu dans mes choix et dans les moments de doute.

Magneto-Inertial Navigation
Principles and application to an indoor
pedometer

Make things as simple as possible but not any simpler.
A. E.

RÉSUMÉ

Cette thèse présente la technique de navigation magnéto-inertielle (MINAV) qui utilise les perturbations du champ magnétique en complément de capteurs inertiels (accéléromètres et gyromètres) pour la localisation d'un corps rigide en mouvement. On étudie des règles de conception, ainsi que des procédures opératoires nécessaires à la mise en pratique dans des conditions réelles. Un exemple de système complet, le "podomètre magnéto-inertiel", permettant la localisation d'un piéton évoluant dans des zones où le GPS est indisponible, est présenté.

ABSTRACT

This thesis presents the magneto-inertial navigation technique (MINAV) using magnetic disturbances and inertial sensors (accelerometers and gyroscopes) to address the positioning problem of a rigid body in motion. The manuscript provides design guidelines and procedures enabling the creation of a system implementing this technique in real conditions. An example of operational system, the "magneto-inertial pedometer", providing a GPS-free indoor navigation solution is presented.

Contents

Introduction	xvii
Nomenclature - Notations	xxi
1 Presentation of inertial navigation principles	1
1.1 The navigation problem	1
1.2 The solution of high-precision inertial navigation	2
1.3 Limitations of low-precision inertial navigation	3
1.4 Usually considered solutions to reduce or bound navigation errors	3
1.4.1 Flaws minimization, data fusion, and dynamics modeling	4
1.4.2 Correction of DR position estimate with position information.	5
1.4.3 Application to indoor navigation	6
1.5 Conclusion on these solutions and presentation of the contribution of this thesis	6
2 Principles of magneto-inertial navigation (MINAV)	9
2.1 A tutorial presentation	9
2.1.1 The basic 1-dimensional problem	9
2.1.2 The general 3-dimensional problem	12
2.2 Asymptotic reconstruction of velocity in the general case	18
2.3 Properties of the magnetic field of importance for the MINAV technique . . .	22
2.3.1 A disturbed field with easily measurable gradients	22
2.3.2 Differential calculus properties	24
2.3.3 Relations with the electric field	24
2.3.4 A field exploitable at various spatial scales	27
3 Design of MINAV systems	29
3.1 Preliminary requirement: timestamping of the digital measurements	31
3.2 Identification of the distance between sensors	35
3.3 Error analysis of velocity equation	36
3.4 Impact of the time-discretization	40
3.4.1 Order of the singularity created by the spatial discretization	42
3.4.2 Evaluation of the integral through Euler-MacLaurin formula	43
3.4.3 Importance of the Cauchy principal value integral	47
3.5 One Practical Implementation: the magneto-inertial pedometer	50

4	Alignment and calibration of MINAV sensors: problems and methods	53
4.1	Errors model for the 3-axis sensors under consideration	54
4.2	Individual 3-axis sensor calibration	55
4.2.1	Background on table-free calibration methods	55
4.2.2	Classical two-step algorithm for magnetometers and accelerometers calibration	56
4.2.3	An iterative algorithm for magnetometers and accelerometers calibration	58
4.3	Calibration of a 3-axis gyrometer with respect to an accelerometer	61
4.4	Calibration of a set of 3-axis magnetometers	65
4.5	Harmonization of inertial and magnetic sensors	66
4.5.1	Identification and correction of trajectory errors due to an harmonization error	69
4.5.2	Practical calibration results and limitations	72
4.6	Proposed operational procedure to calibrate a MINAV system	76
5	Real case study: the MINAV pedometer	77
5.1	State of the art of indoor positioning and navigation techniques	78
5.2	Implementing the MINAV methodology	81
5.2.1	Hardware	81
5.2.2	Software	84
5.3	Experimental results	86
5.3.1	1-dimensional in-lab experiments	86
5.3.2	3-dimensional experiments in various urban environments	87
A	Unbiased calibration problem of a single sensor in 2-dimensions	95
B	A technical result	99
C	Proof of convergence in the linear time varying case	101
D	Observability of accelerometer biases	105
E	More on sensor set calibration	109
E.1	Method 1: first sensor taken as reference	109
E.2	Method 2: two independent calibrations followed by an harmonization step .	110
E.3	Impact of experimental inaccuracies	110
E.3.1	Method 1	111
E.3.2	Method 2	113
E.3.3	Global iterative method	113
E.3.4	Comparison of the proposed methods	113
F	A Kalman filter for attitude determination	115
G	Details on Adams-Bashforth integration scheme	119
G.1	General principle	119
G.2	Determining the weights for a regular time grid	120
G.3	Coefficients in case of a missing sample	121
H	Publications	123

Introduction

L'émergence, puis la vulgarisation du GPS depuis le début des années 2000 a fortement modifié la perception que le grand public a de la localisation et de la navigation. Il est devenu quasiment inconcevable de ne pas pouvoir se localiser dans la vie de tous les jours. Pourtant, en pratique, aucun système réellement universel n'existe, qui permettrait d'avoir une information de position précise à un coût abordable quel que soit l'environnement. Parce qu'elles utilisent des signaux radiofréquences, la plupart des technologies les plus courantes, dont le GPS [67], présentent d'importantes faiblesses. Le GPS est ainsi insuffisamment disponible, facile à brouiller, relativement imprécis et inutilisable pour les applications à l'intérieur de bâtiments tels que les grands centres commerciaux, les parkings souterrains, le métro, voire même en forêt, pour ne citer que quelques exemples.

De manière simultanée, le développement des capteurs MEMS (microsystèmes électromécaniques) leur a permis d'atteindre les marchés grand public. Des capteurs inertiels tels que les accéléromètres et les gyroscopes, qui étaient, à l'origine, l'apanage des systèmes de haute-précision à bord d'avions ou de sous-marins, se retrouvent maintenant dans de nombreux appareils électroniques comme les téléphones portables, les appareils photo numériques ou les consoles de jeu. Leur précision reste cependant loin des standards des techniques de la navigation inertielle conventionnelle [25, 38, 39]. De coûteux capteurs de classe "navigation" peuvent être utilisés pour obtenir des estimations de position, mais, sur le long terme, les dérives sont inévitables. Avec des capteurs bas-coût, estimer la position n'est tout simplement pas possible. En effet, les biais deviennent très vite prépondérants sur les signaux utiles. Toutefois, l'attitude peut être (au moins partiellement) reconstituée [27]. D'autres capteurs doivent être ajoutés pour réduire ou même borner les erreurs de navigation. La plupart de ces capteurs complémentaires nécessitent le déploiement d'une infrastructure pour être opérationnels. On peut citer à titre d'exemple les points d'accès Wifi, les marqueurs visuels ou les amers magnétiques. Installer ces équipements avec une précision suffisante et les maintenir en condition opérationnelle peut se révéler très lourd financièrement, et le temps nécessaire à leur déploiement peut vite devenir prohibitif pour de nombreuses applications. Dans cette thèse, nous considérons une technique de navigation, utilisant des capteurs bas-coût ne nécessitant aucune infrastructure: la navigation magnéto inertielle (MINAV) [109, 110, 111, 112].

Le manuscrit est organisé de la façon suivante. Le principe de la technique MINAV est exposé en détail dans le Chapitre 2. Comme son nom l'indique, elle s'appuie sur une combinaison de capteurs magnétiques et inertiels. On établira, avec des notations précises et appropriées, que la dynamique du champ magnétique exprimée dans le repère des capteurs s'écrit, sous une écriture simplifiée,

$$\dot{B} = -\Omega \times B + J(B)V$$

où B est le champ magnétique, Ω le vecteur rotation instantanée, $J(B)$ la Jacobienne du champs magnétique, i.e. la matrice composée des dérivées partielles du champ magnétique, et V la vitesse que l'on souhaite estimer. En pratique, B et \dot{B} sont déduits des mesures magnétiques, $J(B)$ est mesurée par un gradiomètre ad hoc consistant en un jeu de magnétomètres spatialement répartis, et Ω est mesuré par un gyroscope. Le seul terme inconnu dans cette équation est la vitesse V , que l'on peut donc estimer lorsque les autres termes sont connus.

La conception d'un système de mesure adapté à l'implémentation de la technique MINAV est étudiée en détail dans le chapitre 3. L'implémentation du gradiomètre magnétique ad hoc pose certaines contraintes en termes de datation des mesures et d'espacement entre les magnétomètres. On apporte des solutions pratiques à ces problèmes. Les impacts de l'échantillonnage et de la discrétisation spatiale sont également analysés dans le cadre du gradiomètre. Finalement, ces règles de conception sont appliquées à un système de mesure complet, conçu pour la navigation du piéton en intérieur.

Le Chapitre 4 traite d'un problème qui revêt une importance pratique capitale: la calibration du système de mesure. Chaque capteur 3-axes présente divers défauts, qui, cumulés, ont des effets désastreux. L'orthogonalité entre les axes du capteur peut être prise en défaut, les facteurs d'échelle peuvent varier d'un axe à l'autre, et des couplages entre les axes peuvent apparaître. L'alignement de tous les repères est nécessaire, particulièrement lorsqu'il s'agit de calculer précisément les gradients magnétiques. Toutes les solutions proposées dans ce manuscrit pour minimiser l'impact de ces défauts ont en commun d'être assez facilement utilisables sur le terrain, en suivant des procédures légères.

Enfin, le Chapitre 5 propose l'application de la technique MINAV à la navigation et à la localisation du piéton en intérieur. Les spécificités de cette application et les principales techniques concurrentes et complémentaires que l'on peut trouver dans la littérature sont passées en revue avant de détailler plus avant l'implémentation de la technique MINAV. De la réalisation matérielle à la modélisation retenue, un prototype complet, utilisé expérimentalement, est décrit: le "podomètre magnéto-inertiel". Les résultats expérimentaux obtenus sur plusieurs scénarii et dans divers environnements urbains soulignent la performance du système présenté.

The emergence and the later spread of GPS to a large public since the years 2000 has deeply modified the general perception of positioning and navigation. In everyday's life, it has become hardly conceivable not to be able to locate oneself even if, in practice, no universal system really exists that would yield accurate and affordable positioning solutions in every possible type of environment. Because most current positioning technologies use radio-frequency signals, GPS being a prime example [67], they have major vulnerabilities. In particular, GPS is insufficiently available, easy to jam, relatively inaccurate and useless for indoors applications in environments such as malls, parking lots, subways, or forests, to name a few.

Meanwhile, the development of MEMS (Micro Electro-Mechanical Systems) sensors has enabled them to reach mass markets. Inertial sensors such as accelerometers and gyroscopes, which were originally devoted to high precision navigation tasks aboard aircrafts or submarines, are now included in many electronic devices such as cellphones, digital cameras, or game consoles. Their accuracy however is vastly below the standards of conventional inertial navigation techniques [25, 38, 39]. Costly navigation grade sensors can be used to generate position estimations but, in the long run, drifts are unavoidable. With low-cost sensors, estimating the position is simply not possible. In facts, the drifts are too overwhelming. Yet, the attitude can still be (at least partially) reconstructed [27]. Others sensors have to be added to reduce or even bound navigation errors. Most of these additional sensors require the deployment of an infrastructure to operate. Examples are WiFi-base stations, visual markers, magnetic portals among others. Deploying with a good level of accuracy, and maintaining this infrastructure can reveal extremely costly, and the induced set-up time can turn prohibitive in numerous cases of applications. In this thesis, we consider a navigation technique using low-cost sensors, which does not require any sort of such infrastructure: the magneto-inertial navigation (MINAV) [109, 110, 111, 112].

The manuscript is organized as follows. The principle of the MINAV technique is explained in details in Chapter 2. As its name calls to mind, it relies on a combined usage of magnetic and inertial sensors. One will establish, with appropriate and precise notations, that the dynamics of the magnetic field expressed in the frame of the sensors writes, under a form loosely reported here,

$$\dot{B} = -\Omega \times B + J(B)V$$

where B stands for the magnetic field, Ω for the rate of turn, $J(B)$ for the Jacobian of the magnetic field, i.e. the matrix gathering the partial derivatives of the vector magnetic field, and V the velocity one wishes to estimate. In practice, B and \dot{B} are deduced by magnetometer measurements, $J(B)$ is measured by a custom-built magnetic gradiometer consisting of a set of spatially distributed magnetometers, and Ω is measured by a gyrometer. The only unknown term in this equation is the velocity V , which can thus be estimated based on the knowledge of the other terms.

The design of a measuring system relevant to implement the MINAV technique is studied in details in Chapter 3. The implementation of the custom-built magnetic gradiometer sets requirements on the timing of the measurements, and on the spacing between the magnetometers. Practical ways of solving these issues are provided. The achievable accuracy of such a system is estimated. The impact of the sampling and of the spatial discretization for the gradiometer is also investigated. Finally, a complete measurement system designed for the application to indoor pedestrian navigation is studied as an example.

Chapter 4 deals with a problem which reveals to be of paramount practical importance: the calibration of the measurement system. Each individual 3-axis sensor presents various flaws that, put together, can have disastrous effects. They can have defects in the orthogonality between axes, the scale factors may vary from one axis to the other, and cross-coupling between axes may occur. The alignment of all the sensor frames is required, especially to compute accurate magnetic gradients. All the solutions proposed to minimize the impacts of these flaws have in common to be rather easily achievable on-the-field according to simple procedures.

Finally, in Chapter 5, the application to indoor pedestrian navigation and positioning is reported. The specificities of this application and the possible competing and complementary techniques found in the literature are mentioned before detailing the implementation of the MINAV technique. From the modeling to the hardware, a complete prototype system, “the magneto-inertial pedometer” is described, which is used experimentally. Results obtained in several test-cases and urban environments stress the performance of the presented system.

Nomenclature - Notations

∇B	gradient of a scalar field B (column vector)
$\left(\frac{\partial B}{\partial X}\right)$	Jacobian of the vector field B
$\mathcal{R}_i = (0_i, \mathcal{B}_i)$	inertial frame of reference
$\mathcal{R}_b = (0_b, \mathcal{B}_b)$	body frame of reference
$\Omega_{b/i}$	vector rate of turn of \mathcal{R}_b with respect to \mathcal{R}_i
x	(scalar) position
X	vector position
$(X)_i$	coordinate of X in \mathcal{R}_i
V	velocity vector
$\left(B_x \ B_y \ B_z\right)^T$	vector of measurements along the x -axis, y -axis and z -axis
$\left(u \ v \ w\right)^T$	vector of coordinates of the velocity vector projected onto \mathcal{R}_b
$\left(\frac{\partial B_x}{\partial \mathcal{B}_b}\right)$	transpose of the gradient of the scalar field B_x projected onto \mathcal{R}_b
$\left(\frac{\partial (B)_b}{\partial \mathcal{B}_b}\right)$	Jacobian of the vector field B projected onto \mathcal{R}_b
$P_{i \rightarrow b}$	matrix of the linear operator transforming the vectors of \mathcal{B}_i into \mathcal{B}_b
$\left(p \ q \ r\right)^T$	readings of the gyrometer embedded onto the body
$[(\Omega)_b]$	matrix corresponding to the left-hand-side cross product by $\left(p \ q \ r\right)^T$
$\Delta_x, \Delta_y, \Delta_z$	distances between sensors along the x -axis, y -axis and z -axis
f	sampling frequency
T	sampling time
M_{min}	sensor resolution

Chapter 1

Presentation of inertial navigation principles

Présentation des principes de la navigation inertielle

Après avoir posé le problème général de la navigation en Section 1.1, ce premier chapitre propose, en Section 1.2, une description succincte de la solution offerte par la navigation inertielle haute-précision. Obtenir une estimation de position est possible, mais les erreurs s'accumulent avec le temps. Pour la navigation inertielle avec des capteurs bas-coûts, dont il est question en Section 1.3, les erreurs croissent si vite qu'il est impossible d'utiliser cette seule technique pour obtenir une estimation de la position. En Section 1.4, les principales méthodes de limitations de ces dérives inhérentes aux systèmes inertiels sont présentées, illustrées par quelques exemples.

1.1 The navigation problem

Informally, the general navigation problem is to determine, over time, the position of a rigid body with respect to an inertial frame of reference. As it concerns the general question of positioning for a moving object, this problem is of practical interest in various fields of engineering such as vehicular technology [103], aerospace [55], naval engineering [11, 87], and in academia as well, e.g. in robotics. Navigation information can be used for observation purposes only, or, in a closed-loop approach to determine future decisions board autonomous systems. In the problem stated above, various frames of reference can be considered. For example, positioning information can be expressed with respect to known locations or objects, defining problems of relative navigation.

Nowadays, numerous technologies are available to address navigation problems. We refer the interested reader to [51, 68] for an overview of existing electronic systems (such as GPS, radio-navigation, radar-navigation among others), and to [71] for an historical perspective on this problem (dating back to the early days of celestial navigation).

Mathematically, the navigation problem is relatively easy to describe. Let $\mathcal{R}_i = (0_i, \mathcal{B}_i)$ be an *inertial frame of reference*, where \mathcal{B}_i is a direct orthonormal triaxis equipped with the Euclidean norm, and 0_i is a fixed origin. Consider a rigid body, and a *body frame of reference* $\mathcal{R}_b = (0_b, \mathcal{B}_b)$ attached to it, where 0_b is a given point of the rigid body, and \mathcal{B}_b is another direct orthonormal triaxis. We note $X = 0_i 0_b$ the vector position of the rigid body, and note X_i its coordinates in the inertial frame of reference. Define the rotation operator $R_{i \rightarrow b}$ as the linear operator transforming the vectors of \mathcal{B}_i into the vectors of \mathcal{B}_b . The general navigation problem is to determine both X_i and $R_{i \rightarrow b}$, i.e. determine the position and orientation of the rigid body with respect to the inertial frame of reference.

1.2 The solution of high-precision inertial navigation

One of the main technologies to solve navigation problems is high-precision inertial navigation. *Inertial navigation systems* (INS) use a *dead-reckoning* (DR) type solution to solve the problem described above. Dead-reckoning is the process of estimating the current position by iteratively projecting course and speed from a known initial point. In inertial navigation, the course and speed are determined by a process of integrating a combination of measurements from embedded accelerometers and gyroscopes [90]. These inertial sensors are usually included in an Inertial Measurement Unit (IMU). The main advantage of inertial navigation is that only aboard measurements are used, so that no external information is required. Yet, as is explained below, its main disadvantage is that inertial navigations errors are cumulative.

The main principle used in INS is to integrate the sensed accelerations of the rigid body under consideration in order to obtain velocity and position based on initial conditions (usually a known position and a zero velocity). In high accuracy INS, the gyroscopes of the IMU provide the rigid body attitude and can be used to orient the accelerometers platform (see [39]) in a conventional local coordinate frame (e.g., as explained in [39]). A key point is that accelerometers do not sense accelerations, as could erroneously be deduced from the terminology, but specific forces. In other words, accelerometers sense the sum of external forces divided by the mass *minus* gravitational acceleration. This particularity is the culprit for many problems. To determine the trajectory of the rigid body, the gravitational acceleration must be added to the sensed acceleration. Therefore, all INS include a compensation of gravity. In numerous applications of high accuracy inertial navigation, gravity is not a constant, but depends on the position of the rigid body, which itself, is unknown. As is exposed in [39], errors on the position propagates through the integration process discussed above, in connection with projection errors, under the form of a forced oscillating second order system, which frequency can be analytically determined, e.g. for ballistic missiles [39] by the Schüler effect formula (T=84 min). Oscillations can be attenuated using complementary information stemming from additional sensors such as Doppler radars providing an estimate of the velocity [39].

In such high-precision INS, the position error steadily grows over time. The main limiting factors are the biases of the accelerometers, while the biases of the gyroscopes play a role in the oscillating dynamics of the stabilized platform INS (see [39, 90, 96]). Even though the biases are small in high-precision IMUs, the drift is unavoidable. Typically, the position drift increases by one nautical mile¹ every hour.

¹In details, the variance of uncertainty grows by one nautical mile each hour.

1.3 Limitations of low-precision inertial navigation

Alternatively to the above presented stabilized inertial platforms, which are of common use in accuracy demanding applications such as aeronautical or submarine navigation, other sensor technologies have been considered.

By removing most of the mechanical complexity allowing inertial sensors to be mechanically isolated from the rotational motion of the rigid body, the *strapdown technology* has yielded substantial cost and size reduction, and improved reliability. As a result, small and light weight INS are now incorporated in numerous applications ranging from military vehicles [104], intelligent weapons, to robotics, UAVs [16] among others. We refer the reader to [105] or [96], for a detailed presentation of the strapdown technology. As exposed in this reference, strapdown technology suffers from several drawbacks among which is the increase of computing complexity, which is only a relative issue as embedded computational power is now relatively affordable.

In strapdown technology, numerous classes of sensors exists. Accelerometers can be mechanical, solid-state, vibrating quartz, vibrating optic fiber. Gyroscopes can be vibratory, electrostatic, optical. Further, in low-cost INS the sensors used, which are usually MEMS sensors (Microelectromechanical systems), are by several orders of magnitude less accurate than the previously discussed sensors. Besides, the rotational sensors must be capable of measuring high rates of turn. As a result of this requirement and the previously mentioned flaws, the gyroscopes are considered to be capable of providing only rate-of-turn information and not rotation angles². This fact introduces extra errors in the projection of accelerations and in the DR process, in turn.

With MEMS INS, inertial navigation cannot be used to determine position of the rigid body, due to overwhelming drifts. It can provide partial information on the attitude, yet. As has been exposed in [74, 107], under the assumption that the rigid body is not accelerating, readings from the accelerometers can be used to determine its inclination, i.e. two independent angles of its attitude, while the heading information (which is given by the measure of the rotation of the Earth in high-end INS) can not be obtained. Gyroscopes can be used, in a complementary filter, to infer the attitude dynamics. This point is largely described in [54].

As for high-end INS, the position error using low-cost MEMS INS grows over time. Again, the main culprits are the biases of the accelerometers. The biases of low-cost IMUs are by several orders of magnitude larger than those of high-end IMUs. Typically, the position drift increases by several hundred meters each minute. Again, additional techniques must be used to limit this detrimental effect.

1.4 Usually considered solutions to reduce or bound navigation errors

As previously discussed, any INS drifts over time. It can be a matter of days (with high-end IMUs) or seconds (with lower-grade IMUs) before the navigation estimates gets too erroneous to be used in any way. Therefore, complementary solutions are required to prevent this drift from becoming too large. All the complementary solutions add some information

²For this reason, they are often referred to as rate gyroscopes or gyrometers.

to the INS system, but in different ways. A first approach, pictured in Figure 1.1, consists in regularly correcting (totally or partially) the position estimated by the DR system by using a dependable position information. From this, the cumulative error of the DR system can be reset, ideally to zero, or more often to a bounded value, as frequently as the new information permits. Implicitly, the time horizon over which the DR error is integrated is thus a lot shortened. Provided that this correction occurs often enough, the error can be kept within certain bounds, virtually indefinitely. Illustrative examples are given in Section 1.4.2. Between two corrections, however, the DR error is not improved. The second and complementary approach is to add some information in the DR system itself, e.g. by modeling the sensors biases, combining sources of information, or modeling the dynamics of the body in motion. The error of the DR system can then be lowered further. As a result, the position estimation keeps drifting, but at a slower rate. The error is thus kept under given limits for a longer period of time. Examples are shown in Section 1.4.1. Both techniques are not exclusive and complete each other very well.

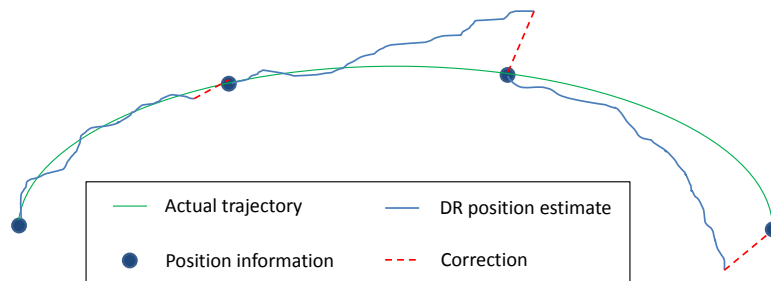


Figure 1.1: The DR estimate is regularly corrected by a position information.

1.4.1 Flaws minimization, data fusion, and dynamics modeling

Consider raw measurements of high-end INS sensors. Many techniques can be used to improve the accuracy of the final position estimate. First, raw measurements can be partially corrected. The sensors always present mechanical flaws resulting from the assembly. These can be estimated and corrected up to a certain point. Due to setup or usage, their sensitivity may become slightly altered overtime. Their responses often vary with the temperature or even the pressure or the humidity. All those flaws may be partially accounted for by relevant calibration techniques and procedures, which may require the use of other sensors (e.g. temperature sensors) to serve as external references. Placing the sensors at one position or another in the vehicle of interest may also impact its accuracy. Inertial sensors are, for instance, most often (partially) isolated from vibrations.

Another classical source of improvement is data fusion. It consists in combining multiple sources of information, having various uncertainties, to determine a potentially more accurate position estimate. On many vehicles where inertial systems have been used for a long time, velocity measurements have been added. Locks used aboard ships measure the fluid flow velocity, i.e. the velocity of the ship with respect to the water. Aboard aircrafts, Pitot probes have been added to measure air velocity. The error made by the DR system on the velocity

is thus reduced, and the error on position is lowered accordingly. In low-cost INS using IMUs such as [5, 80, 115], the heading information cannot be obtained by the measurement of the Earth rotation through the gyroscopes³. Their information can be integrated, but, as already mentioned drifts significantly. The heading is also inferred from the readings of a compass which is incorporated in the IMU.

Finally, some a priori knowledge can be incorporated in the DR estimation process by modeling. Ships, aircrafts [2] and cars [91] have very different dynamics. Many forces and torques can be derived from physical laws (e.g. from the fluid dynamics [79]) and from the knowledge of input signals to the governing equations of the vehicle (e.g. steering angle, propulsion) All this a priori knowledge can be gathered into a dynamical model describing how the system evolves. The measurements (including the input signals) feed the model to yield a more accurate estimation of the position. Improving the model may require additional sensors. Aboard spacecraft for instance, a first approach would be to consider an uniform gravitational field. However, it has been known for a long time that the gravity field is not uniform. The Earth is not exactly a sphere, thus other terms (e.g. J2 harmonics, see e.g. [4] for a precise model of the Earth gravity field) leading to more accurate model can be taken into account. Models and tables have been built to estimate its value with various accuracy depending on the position. But as neither the position estimate nor the model are perfect, it has even be proposed to go further: measuring the variations of the gravitational field through a gradiometer could reveal valuable to get a better interpretation of the accelerometers data as proposed in [64, 97].

Numerous practical DR system incorporate one or several of the above presented techniques. In some cases, blending these techniques can even allow to provide an interesting position estimate by adding a few other low-cost sensors to low-end inertial sensors. In [18], in the case of automotive vehicles, a magnetic velocimeter along with a fine modeling of the various driving phases was proposed to significantly improve the position estimate. In the case of autonomous UAV, embedded cameras have been added to an IMU to guarantee self-stabilization properties [16].

1.4.2 Correction of DR position estimate with position information.

When position information is available, the DR can be more easily corrected. A very simple case of DR, one can think of, is the one of a train traveling between two stations. After the train departure and before the arrival, one may wish to have an estimation of its position, e.g. for safety reasons, or to lower the energy consumption in an active control strategy cutting down the propulsion to progressively slow down before the station. For this purpose, a DR system can be mounted on the train. As cumulative errors of inertial navigation (or odometry) quickly become large, magnetic anchors are put along the rails at known locations. When the train arrives at one such anchor, the device is detected, which allows to correct the position provided by the DR estimate since the last anchor. Thus, the position error can be kept within limits provided the anchors are numerous enough. Figure 1.2 pictures the position computed on a simplified simulation, with DR only, or with DR and the corrections by the anchor positions.

³This is the technique of gyro-compass.

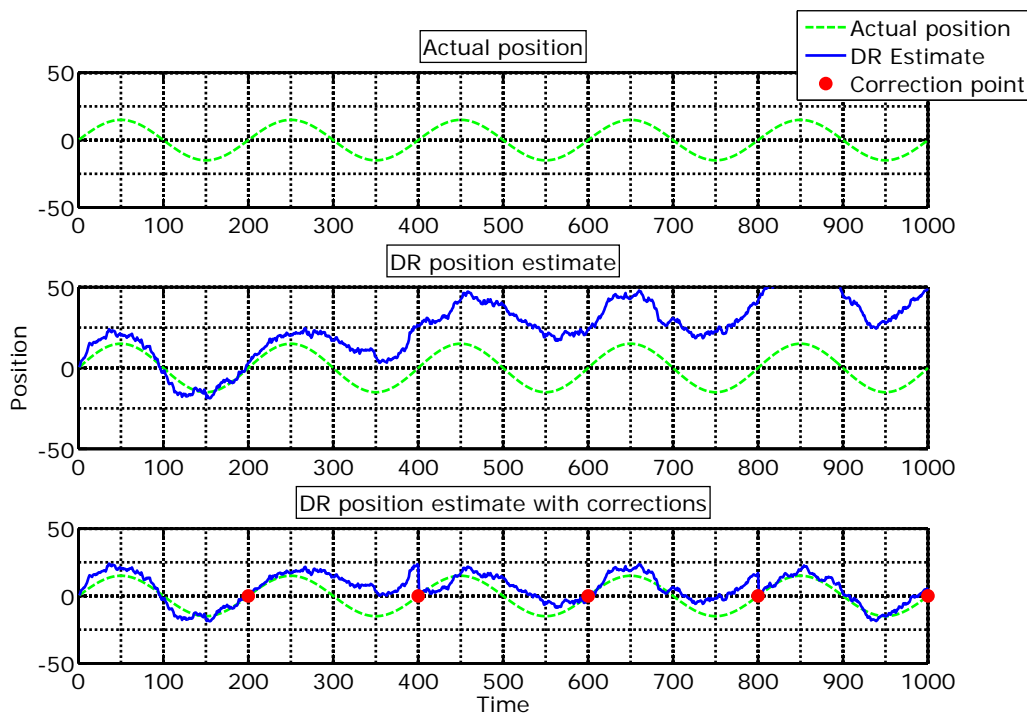


Figure 1.2: The DR estimate is regularly corrected by a position information.

1.4.3 Application to indoor navigation

For indoor positioning applications, many corrections of the previous type can be performed. Absolute positioning information can be obtained via optical systems (requiring markers or projectors to be observed by cameras), radio-frequency (using fingerprinting from fixed transmitters), Radio Frequency IDentification (RFID, fingerprinting from deployed nodes), Ultra Wide Band (UWB, requiring fixed synchronized nodes), cellular networks (requiring base stations as infrastructures), floor sensors (requiring the deployment of special floor tiles), radar (usually requiring fixed transponders). We refer the interested reader to [77] and [76].

1.5 Conclusion on these solutions and presentation of the contribution of this thesis

As has been detailed, most techniques commonly considered to reduce or bound the errors of inertial navigation require some sort of infrastructure, anchors, additional sensors, or external sources of information. These represent strong limitations on the usage of the resulting positioning systems. In this thesis, we use existing sensors in a new way. Combining inertial measurements to magnetic sensors (usually already present in INS), we show how the velocity of a moving rigid body onto which this combined system is mounted can be estimated. This is the MINAV (Magneto-Inertial) technique [109, 110, 111, 112]. Its principles are exposed in the following Chapter 2. In Chapter 3, design rules are detailed. In Chapter 4, practical procedures are exposed to enable usage of the necessary set of sensors. In Chapter 5,

1.5. *CONCLUSION ON THESE SOLUTIONS AND PRESENTATION OF THE
CONTRIBUTION OF THIS THESIS*

experimental results using a navigation system implementing the MINAV technique are reported.

Chapter 2

Principles of magneto-inertial navigation (MINAV)

Principes de la navigation magnéto-inertielle (MINAV)

Ce chapitre propose, en Section 2.1, une présentation tutorielle de la navigation magnéto-inertielle (MINAV) en commençant par le cas mono-dimensionnel d'un mobile se déplaçant le long d'un axe, puis en introduisant les translations en trois dimensions, avant de conclure, en Section 2.2, par le cas général d'un mobile à six degrés de liberté, pouvant simultanément tourner et se traduire dans l'espace. Un observateur simple est proposé permettant d'estimer la vitesse du mobile à partir de mesures du champ magnétique et de sa Jacobienne (matrices des gradients partiels), ainsi que des données d'un gyroscope. Finalement, en Section 2.3, quelques propriétés du champ magnétique, intéressantes pour la technique MINAV, sont étudiées.

In this chapter, we gradually expose the principles of magneto-inertial navigation (MINAV), starting with a tutorial presentation, before addressing the general case and the technique of velocity estimation by a state observer.

2.1 A tutorial presentation

2.1.1 The basic 1-dimensional problem

Following the navigation problem statement of §1.1, we consider, using the notations previously introduced, a one dimensional problem of position estimation. Consider a scalar field B depending on the position on an x -axis along an inertial frame of reference \mathcal{R}_i . Implicitly, this is a stationary field i.e. it does not depend on time. Consider a device moving along this x -axis, and measuring this field B . Its position at time t is noted $x(t)$ with respect to the inertial frame of reference \mathcal{R}_i . The variations of the sensed field can be obtained by a

simple chain rule differentiation. One has

$$\frac{dB(x(t))}{dt} = \frac{dB}{dx}(x(t))\dot{x}(t) \quad (2.1)$$

In words, the time variation of the field seen by the moving device is directly related to the gradient of the field $\frac{dB}{dx}$ and to the speed $\dot{x} \triangleq v$ of the device. Formally, if the device can measure the field B and its gradient $\frac{dB}{dx}$, its speed can be reconstructed by solving Equation (2.1) with respect to v . Practically, various sources of noise prevent one to proceed this way, and rather, an asymptotic observer is used to determine the unknown velocity v . Note B_x the measurement of the device, and $\frac{dB_x}{dx}$ the derivative of the reading of the device with respect to the x -coordinate.

Choosing a vector state with the magnetic field and the velocity $\begin{pmatrix} B_x & v \end{pmatrix}^T$ and assuming a null dynamic for the device, and a constant gradient

$$\frac{dv}{dt} = \sum \text{forces per unit of mass} = 0$$

the considered dynamical system writes in the (autonomous) state-space form

$$\frac{d}{dt} \begin{pmatrix} B_x \\ v \end{pmatrix} = \begin{pmatrix} 0 & \frac{dB}{dx} \\ 0 & 0 \end{pmatrix} \begin{pmatrix} B_x \\ v \end{pmatrix} \quad (2.2a)$$

$$y = \begin{pmatrix} 1 & 0 \end{pmatrix} \begin{pmatrix} B_x \\ v \end{pmatrix} \quad (2.2b)$$

The gradient of the field $\frac{dB}{dx}$ is considered as a measured input, and the measured output is simply the value of the field B_x .

Straightforwardly, the observability matrix \mathcal{O} of this state-space representation is

$$\mathcal{O} = \begin{pmatrix} 1 & 0 \\ 0 & \frac{dB_x}{dx} \end{pmatrix}$$

The system is thus observable wherever the gradient of the field is non trivial. The unknown state v can be reconstructed by means of an asymptotic observer. This means that the velocity can be estimated solely from the measurements of the field (and its gradient) wherever the gradient is non trivial. No further requirement has been made on the non-uniform field under consideration. This scalar field can, in practice and among other possibilities, be a component of the magnetic field or of the electric field, the temperature, the ambient light intensity or the pressure. The precision of the estimated velocity will, obviously, depend greatly on the accuracy of the sensors with respect to the variations of the field along the direction of move. This point is particularly discussed in Section 3.3.

We now go one step further and propose a simple observer to actually estimate the velocity of the device in this one dimensional configuration.

Proposition 1: Consider the following observer for the system (2.2)

$$\begin{aligned} \dot{\hat{B}}_x &= \frac{dB_x}{dx} \left[\hat{v} - \ell_1 \frac{dB_x}{dx} (\hat{B}_x - y) \right] \\ \dot{\hat{v}} &= -\ell_2 \frac{dB_x}{dx} (\hat{B}_x - y) \end{aligned}$$

where $\ell_1 > 0$ and $\ell_2 > 0$ are arbitrary constant gains. This observer asymptotically converges towards the actual field and velocity governed by the dynamics (2.2), provided that $\frac{dB_x}{dx} \neq 0$. \square

Proof: Consider the candidate Lyapunov-function W

$$W = \frac{1}{2} (\hat{B}_x - B_x)^2 + \frac{1}{2\ell_2} \cdot (\hat{v} - v)^2$$

Its time-derivative is

$$\dot{W} = (\hat{B}_x - B_x) \left[\frac{dB_x}{dx} \left(\hat{v} - \ell_1 \frac{dB_x}{dx} (\hat{B}_x - B_x) \right) - \frac{dB_x}{dx} v \right] - (\hat{v} - v) \frac{dB_x}{dx} (\hat{B}_x - B_x)$$

This gives,

$$\dot{W} = -\ell_1 \left(\frac{dB_x}{dx} \right)^2 (\hat{B}_x - B_x)^2$$

Choosing $\ell_1 > 0$ guarantees that \dot{W} is negative semidefinite. If the set \dot{W} contains no other trajectory except the trivial one $(\hat{B}_x - B_x, \hat{v} - v) = (0, 0)$, then, according to LaSalle's invariance principle [69], the origin of the error dynamics is globally asymptotically stable. Let us verify that the invariant set is, in fact, reduced to the origin. Trajectories lying in the set $\dot{W} = 0$ are such that

$$\frac{dB_x}{dx} (\hat{B}_x - B_x) = 0$$

By assumption, $\frac{dB_x}{dx}$ is non-zero, i.e. the field B is non-uniform, we obtain

$$\hat{B}_x - B_x = 0$$

This can be expressed as follows

$$\dot{\hat{B}}_x - \dot{B}_x = \frac{dB_x}{dx} \left[\hat{v} - \ell_1 \frac{dB_x}{dx} (\hat{B}_x - B_x) \right] - \frac{dB_x}{dx} v$$

which yields, in the set $\hat{B}_x - B_x = 0$,

$$0 = \hat{v} - v$$

■

To conclude, if the gradient $\frac{dB_x}{dx}$ is non-zero, and in practice it usually is since the field is assumed to be non-uniform, the observer asymptotically converges towards the actual value of the field and the velocity.

The principle presented above allows to estimate the velocity of a device translating along a single axis by solely measuring any non-uniform field and its gradient along the direction of movement. No inertial measurement is even necessary. In practice, the gradient can be estimated using two sensors aligned with the direction of movement at a known distance one from the other¹. A simulation of the field and the velocity reconstruction with noisy measurements is presented in Figure 2.1. The device is translated of 1 cm every 4 s. The estimated speed is noisy but accurate. Once integrated (which partially gets rid off the noise), it provides a reliable position estimate.

¹A method to accurately identify this distance for a given apparatus is given in Section 3.2.

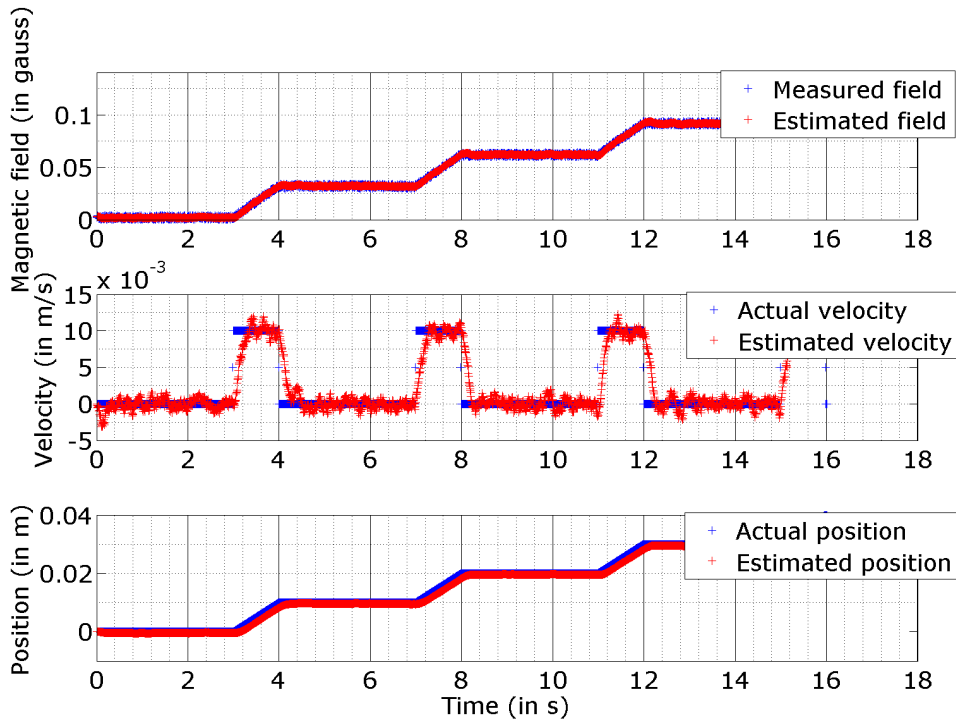


Figure 2.1: Simulation results - The platform is translated step by step in the direction sensors are lined up. One step of 1 cm is made every 4 s.

2.1.2 The general 3-dimensional problem

To extend the principle exposed above in the simple 1-dimensional case to the more general case of a device which can actually rotate and translate in a 3-dimensional space, we proceed in two steps. First, the problem is extended to a device that can translate in all 3 directions. Then, rotations are taken into account.

Translations

Consider a device that can translate in a classical 3-dimensional space. First, a scalar field is considered. In theory, any scalar field such as the temperature, the pressure or the light intensity (see [116]) could be considered. However, the inadequacy of the scalar field will be pointed out, and vector fields will be used instead. From a practical point of view, and considering the sensing technologies available, the magnetic field ranges among them.

Scalar field Consider a scalar field B depending on the position X in a 3-dimensional space with respect to an inertial frame of reference \mathcal{R}_i , and a device that can freely translate in any direction. We note \mathcal{R}_b the body frame of reference attached to the device. Without loss of generality, it can be assumed that the axes of \mathcal{R}_i and \mathcal{R}_b coincide since no rotation is permitted. The position of the device at time t is denoted $X(t)$. We note $V(t)$ its velocity

with respect to \mathcal{R}_i . By a simple chain rule, one has the vector equation

$$\frac{dB(X(t))}{dt} = (\nabla B(X(t)))^T V(t) \quad (2.3)$$

where ∇B is the gradient of B . This expression is similar to Equation (2.1).

A scalar measurement is performed with the device. Without loss of generality, we note it B_x . Further, we note $(u \ v \ w)^T$ the vector containing the coordinates of V projected in \mathcal{R}_b .

Considering the state vector $(B_x \ u \ v \ w)^T$, one can write the dynamics under the state-space form, assuming the body velocity is constant

$$\begin{aligned} \frac{d}{dt} \begin{pmatrix} B_x \\ u \\ v \\ w \end{pmatrix} &= \begin{pmatrix} 0 & \frac{\partial B_x}{\partial \mathcal{B}_b} \\ 0_{3 \times 1} & 0_{3 \times 3} \end{pmatrix} \begin{pmatrix} B_x \\ u \\ v \\ w \end{pmatrix} \\ y &= \begin{pmatrix} 1 & 0 & 0 & 0 \end{pmatrix} \begin{pmatrix} B_x \\ u \\ v \\ w \end{pmatrix} \end{aligned}$$

where $\frac{\partial B_x}{\partial \mathcal{B}_b}$ is the transpose of the gradient of the scalar field B_x projected onto the body reference frame \mathcal{R}_b .

Considering this system as autonomous, the observability matrix \mathcal{O} of the system is

$$\mathcal{O} = \begin{pmatrix} 1 & 0 \\ 0 & \frac{\partial B_x}{\partial \mathcal{B}_b} \\ 0 & 0 \\ 0 & 0 \end{pmatrix}$$

which is obviously of rank 2 when the field is non-uniform and of rank 1 when the field is uniform. The full state cannot be observed, which means that the velocity vector cannot be correctly estimated solely from one scalar measurement. This single measurement is not sufficient to distinguish between the contribution of the three components of the velocity. One has to add other measurements, which naturally leads to the consideration of vector fields.

Vector field Consider a three dimensional vector field B depending on the position X in a 3-dimensional space equipped with an inertial frame of reference \mathcal{R}_i . Consider a device that can freely translate in any direction. We note \mathcal{R}_b the body frame of reference attached to the device. Again, it is considered that the axes of \mathcal{R}_i and \mathcal{R}_b coincide since no rotation is

permitted. The position of the device at time t is denoted $X(t)$. We note $V(t)$ its velocity with respect to \mathcal{R}_i . By a simple chain rule, one has the vector equation

$$\frac{dB(X(t))}{dt} = \left(\frac{\partial B(X(t))}{\partial X} \right) V(t)$$

where $\left(\frac{\partial B}{\partial X} \right)$ is the (matrix) Jacobian of B . This expression is similar to Equation (2.1) and Equation (2.3).

A 3-dimensional measurement is performed with the device. We note it $\left(B_x \ B_y \ B_z \right)^T$. Again, we note $\left(u \ v \ w \right)^T$ the vector containing the coordinates of V projected in \mathcal{R}_b .

The state gathers the measured components of the field and the velocity, $\left(B_x \ B_y \ B_z \ u \ v \ w \right)^T$. Under the state-space form, one considers

$$\frac{d}{dt} \begin{pmatrix} B_x \\ B_y \\ B_z \\ u \\ v \\ w \end{pmatrix} = \begin{pmatrix} 0_{3 \times 3} & \left(\frac{\partial(B)_b}{\partial \mathcal{B}_b} \right) \\ 0_{3 \times 3} & 0_{3 \times 3} \end{pmatrix} \begin{pmatrix} B_x \\ B_y \\ B_z \\ u \\ v \\ w \end{pmatrix} \quad (2.4a)$$

$$y = \begin{pmatrix} I_3 & 0_3 \end{pmatrix} \begin{pmatrix} B_x \\ B_y \\ B_z \\ u \\ v \\ w \end{pmatrix} \quad (2.4b)$$

where $\left(\frac{\partial(B)_b}{\partial \mathcal{B}_b} \right)$ is the Jacobian of the magnetic field projected onto the body reference frame, i.e. the term (1, 2) of $\left(\frac{\partial(B)_b}{\partial \mathcal{B}_b} \right)$, for instance, is the derivative of the component B_x of the magnetic field with respect to the second base-vector of the body frame.

Considering this system as autonomous, the observability matrix \mathcal{O} of the system is now

$$\mathcal{O} = \begin{pmatrix} I_3 & 0_3 \\ 0_3 & \left(\frac{\partial(B)_b}{\partial \mathcal{B}_b} \right) \\ 0_{12 \times 3} & 0_{12 \times 3} \end{pmatrix}$$

which is obviously of rank 6 whenever the Jacobian $\left(\frac{\partial(B)_b}{\partial \mathcal{B}_b} \right)$ is full-rank. In that case, the state is fully observable and the velocity can be reconstructed.

In practice, the field under consideration can be the magnetic field, the electric field... or even any combination of three independent scalar fields. As in the 1-dimensional case, a simple asymptotic observer can be proposed to estimate the velocity.

Proposition 2: Consider the following observer for the autonomous system (2.4)

$$\begin{aligned}\dot{\hat{B}} &= \left(\frac{\partial (B)_b}{\partial \mathcal{B}_b} \right) \left[\hat{V} - \ell_1 \left(\frac{\partial (B)_b}{\partial \mathcal{B}_b} \right)^T (\hat{B} - y) \right] \\ \dot{\hat{V}} &= -\ell_2 \left(\frac{\partial (B)_b}{\partial \mathcal{B}_b} \right)^T (\hat{B} - y)\end{aligned}$$

where $\ell_1 > 0$ and $\ell_2 > 0$ are constant gains. This observer asymptotically converges towards the actual field and velocity satisfying (2.4a), provided that $\left(\frac{\partial (B)_b}{\partial \mathcal{B}_b} \right)$ is non-singular. \square

The proof of this result is a subcase of the proof of Proposition 3 derived in Section 2.2.

Earlier, Proposition 1 estimated the scalar velocity of a device translating along a single axis by measuring a scalar field and its gradient along that axis. The scalar field was not sufficient to extend this result to 3-dimensional translations. The measurement of a vector field is necessary in that case. Proposition 2 proposes to reconstruct the velocity in such a case by solely measuring a vector field and its non singular Jacobian.

Accounting for rotations

The last step to generalize the result is to allow rotations. Due to the rotations, the axes of \mathcal{R}_i and \mathcal{R}_b do not coincide anymore. We note $P_{i \rightarrow b}$ the matrix of the linear operator transforming the vectors of \mathcal{B}_i into the vectors of \mathcal{B}_b , and $\Omega_{b/i}$ the vector rotation of \mathcal{R}_b with respect to \mathcal{R}_i . To measure this rotation, the device is complemented by a rigidly attached gyrometer measuring rates of turn in the \mathcal{R}_b reference frame. A chain rule differentiation with respect to \mathcal{R}_i , i.e. considering the vectors of \mathcal{R}_i as constant, yields

$$\left. \frac{dB}{dt} \right|_{\mathcal{R}_i} = \left(\frac{\partial B}{\partial X} \right) V$$

where

$$V = \left. \frac{dX}{dt} \right|_{\mathcal{R}_i}$$

The dynamics can be transposed with respect to the body frame \mathcal{R}_b . One has, when differentiation is performed by considering the vectors of \mathcal{R}_b as constant,

$$\left. \frac{dB}{dt} \right|_{\mathcal{R}_b} = -\Omega_{b/i} \wedge B + \left. \frac{dB}{dt} \right|_{\mathcal{R}_i}$$

Finally,

$$\boxed{\left. \frac{dB}{dt} \right|_{\mathcal{R}_b} = -\Omega_{b/i} \wedge B + \left(\frac{\partial B}{\partial X} \right) V} \quad (2.5)$$

In this equation, $\left(\frac{\partial B}{\partial X} \right)$ is the Jacobian of the magnetic field, while V is the velocity with respect to \mathcal{R}_i , and finally $\left. \frac{dB}{dt} \right|_{\mathcal{R}_b}$ is the time derivative of the vector B at constant \mathcal{R}_b . The

projection of this vector equation onto the \mathcal{R}_b reference frame gives

$$\boxed{\begin{pmatrix} \dot{B}_x \\ \dot{B}_y \\ \dot{B}_z \end{pmatrix} = - \begin{pmatrix} p \\ q \\ r \end{pmatrix} \wedge \begin{pmatrix} B_x \\ B_y \\ B_z \end{pmatrix} + \left(\frac{\partial(B)_b}{\partial \mathcal{B}_b} \right) \begin{pmatrix} u \\ v \\ w \end{pmatrix}} \quad (2.6)$$

In this expression, the vector $\begin{pmatrix} p & q & r \end{pmatrix}^T$ contains the readings of the embedded gyroscope, $\begin{pmatrix} B_x & B_y & B_z \end{pmatrix}^T$ is the vector containing the readings of the embedded magnetometer, $\left(\frac{\partial(B)_b}{\partial \mathcal{B}_b} \right)$ is the matrix containing the partial derivatives of the readings of the embedded magnetometer with respect to the body reference frame \mathcal{R}_b , $\begin{pmatrix} u & v & w \end{pmatrix}^T$ is the vector containing the coordinates of V projected in \mathcal{R}_b .

The motion of the device is expressed in the body frame by Newton's law. The body frame can rotate with respect to the inertial frame, so one has

$$\dot{V} = -\Omega_{b/i} \times V + F_m \quad (2.7)$$

where F_m is the total force per unit of mass applied to the device. As in the case where only translations were considered, one can model the total force with zero mean, i.e. $F_m = 0$. Other modeling choices are possible (e.g. in Chapter 5). Projecting this vector equation onto the \mathcal{R}_b reference frame yields

$$\begin{pmatrix} \dot{u} \\ \dot{v} \\ \dot{w} \end{pmatrix} = - \begin{pmatrix} p \\ q \\ r \end{pmatrix} \times \begin{pmatrix} u \\ v \\ w \end{pmatrix}$$

For sake of observability analysis, the chosen state is unchanged, $(B_x \ B_y \ B_z \ u \ v \ w)^T$, and the system writes

$$\frac{d}{dt} \begin{pmatrix} B_x \\ B_y \\ B_z \\ u \\ v \\ w \end{pmatrix} = \begin{pmatrix} -[(\Omega)_b] & \left(\frac{\partial(B)_b}{\partial \mathcal{B}_b}\right) \\ 0_{3 \times 3} & -[(\Omega)_b] \end{pmatrix} \begin{pmatrix} B_x \\ B_y \\ B_z \\ u \\ v \\ w \end{pmatrix} \quad (2.8a)$$

$$y = \begin{pmatrix} I_3 & 0_3 \end{pmatrix} \begin{pmatrix} B_x \\ B_y \\ B_z \\ u \\ v \\ w \end{pmatrix} \quad (2.8b)$$

where $[(\Omega)_b]$ is the matrix corresponding to the left-hand-side cross product by $(p \ q \ r)^T$, i.e.

$$[(\Omega)_b] = \begin{pmatrix} 0 & -r & q \\ r & 0 & -p \\ -q & p & 0 \end{pmatrix} \quad (2.9)$$

Considering the system as autonomous, the observability matrix \mathcal{O} of the system is

$$\mathcal{O} = \begin{pmatrix} I_3 & 0_3 \\ -[(\Omega)_b] & \left(\frac{\partial(B)_b}{\partial \mathcal{B}_b}\right) \\ [(\Omega)_b]^2 & -2[(\Omega)_b] \left(\frac{\partial(B)_b}{\partial \mathcal{B}_b}\right) \\ \vdots & \vdots \end{pmatrix}$$

which is obviously of rank 6 whenever the Jacobian is full-rank. In that case, the state is fully observable and the velocity can be reconstructed.

In summary, in the most general case of a rigid body which can simultaneously rotate and translate in a 3-dimensional space, the velocity is observable from the measurements of a non-uniform (stationary) vector field and its gradient, and, to take the rotations into account, the knowledge of the rate of turn of the rigid body is also required.

As a vector field, the magnetic field is a suitable field for the presented velocity reconstruction technique for several reasons: its availability almost everywhere, the vast range of measurement systems that can be found on-the-shelf, and the fact that it is very often spatially non-uniform, especially in places where radio-frequency signals (e.g. GPS) are unavailable.

2.2 Asymptotic reconstruction of velocity in the general case

In the previous introductory discussion, we have shown that the velocity of a rigid body moving in a 3-dimensional space area where a 3-dimensional vector field is spatially disturbed is observable from embedded measurements of the field and its Jacobian, provided that the rate of turn of the rigid body is known. We now make a formal statement of this result summarizing the MINAV approach. An example of realization is schematically pictured in Figure 2.2.

The magneto inertial technique (MINAV) addresses the problem of estimating the motion of a rigid body with respect to an inertial frame of reference \mathcal{R}_i . In this technique, the rigid body is equipped with an embedded magnetic field gradiometer, and an inertial measurement unit (IMU).

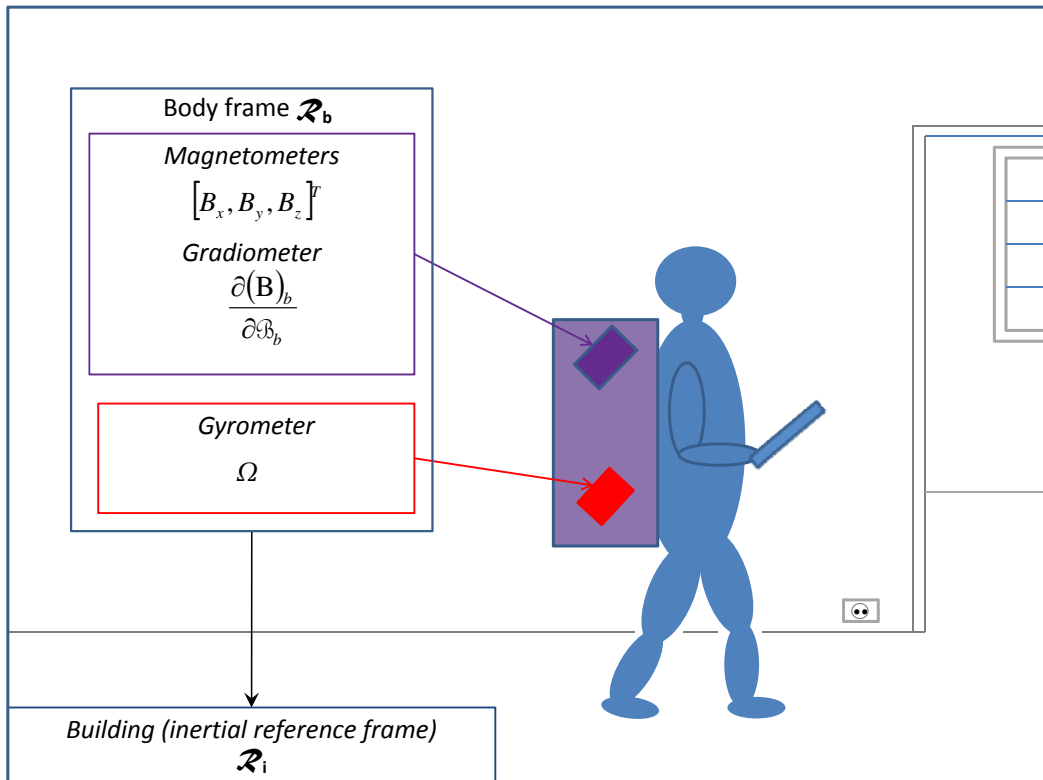


Figure 2.2: Reference frames and measurements in the case of pedestrian walking indoor.

Proposition 3: Consider a rigid body moving in a 3-dimensional space equipped with an inertial frame of reference \mathcal{R}_i . Consider a body frame of reference \mathcal{R}_b attached to the rigid body. The rigid body is equipped with a gyrometer producing a vector of readings $(p \ q \ r)^T$, a sensor measuring the three components of a field (e.g. the magnetic field) projected onto the body reference frame \mathcal{R}_b , $(B_x \ B_y \ B_z)^T$, and a gradiometer of this

2.2. ASYMPTOTIC RECONSTRUCTION OF VELOCITY IN THE GENERAL CASE

field whose reading is $\left(\frac{\partial(B)_b}{\partial\mathcal{B}_b}\right)$, the matrix containing the partial derivative of these three components. The vector $(V)_b = \begin{pmatrix} u & v & w \end{pmatrix}^T$, which is the projection of the velocity V with respect to the inertial reference frame \mathcal{R}_i onto the \mathcal{R}_b frame, can be reconstructed by the following observer

$$\dot{\hat{B}} = - \begin{pmatrix} p \\ q \\ r \end{pmatrix} \times \hat{B} + \left(\frac{\partial(B)_b}{\partial\mathcal{B}_b}\right) \left[\hat{V} - \ell_1 \left(\frac{\partial(B)_b}{\partial\mathcal{B}_b}\right)^T \left(\hat{B} - \begin{pmatrix} B_x \\ B_y \\ B_z \end{pmatrix}\right) \right] \quad (2.10a)$$

$$\dot{\hat{V}} = - \begin{pmatrix} p \\ q \\ r \end{pmatrix} \times \hat{V} - \ell_2 \left(\frac{\partial(B)_b}{\partial\mathcal{B}_b}\right)^T \left(\hat{B} - \begin{pmatrix} B_x \\ B_y \\ B_z \end{pmatrix}\right) \quad (2.10b)$$

where $\ell_1 > 0$ and $\ell_2 > 0$ are constant gains, as this observer constitutes with (2.8a) an error dynamics that is asymptotically converging to 0 when the matrix $\left(\frac{\partial(B)_b}{\partial\mathcal{B}_b}\right)$ is non-singular. \square

Proof: Again, the system is considered autonomous. Consider the candidate Lyapunov function W

$$W = \frac{1}{2} \left\| \hat{B} - \begin{pmatrix} B_x \\ B_y \\ B_z \end{pmatrix} \right\|^2 + \frac{1}{2\ell_2} \cdot \left\| \hat{V} - \begin{pmatrix} u \\ v \\ w \end{pmatrix} \right\|^2$$

Its time derivative can be written under the form

$$\dot{W} = -\ell_1 \left(\hat{B} - \begin{pmatrix} B_x \\ B_y \\ B_z \end{pmatrix}\right)^T \underbrace{\left[\left(\frac{\partial(B)_b}{\partial\mathcal{B}_b}\right) \left(\frac{\partial(B)_b}{\partial\mathcal{B}_b}\right)^T \right]}_Q \left(\hat{B} - \begin{pmatrix} B_x \\ B_y \\ B_z \end{pmatrix}\right)$$

$\ell_1 > 0$ is arbitrarily chosen, and Q is positive definite, thus $\dot{W} \leq 0$. If the set

$$\left\{ \dot{W} \left(\hat{B} - \begin{pmatrix} B_x \\ B_y \\ B_z \end{pmatrix}, \hat{V} - \begin{pmatrix} u \\ v \\ w \end{pmatrix} \right) = 0 \right\}$$

contains no other trajectory except the trivial one

$$\left(\hat{B} - \begin{pmatrix} B_x \\ B_y \\ B_z \end{pmatrix}, \hat{V} - \begin{pmatrix} u \\ v \\ w \end{pmatrix} \right) = (0, 0)$$

then, from LaSalle's invariance principle [69], the origin is globally asymptotically stable.

Indeed, the invariant set is reduced to the origin. Trajectories lying in the set $\dot{W} = 0$ are such that

$$\left(\frac{\partial(B)_b}{\partial\mathcal{B}_b}\right)^T \left(\hat{B} - \begin{pmatrix} B_x \\ B_y \\ B_z \end{pmatrix}\right) = 0$$

Assuming $\left(\frac{\partial(B)_b}{\partial\mathcal{B}_b}\right)$ has full rank, i.e. there are enough magnetic disturbances, one obtains

$$\frac{d}{dt}\hat{B} - \frac{d}{dt}\begin{pmatrix} B_x \\ B_y \\ B_z \end{pmatrix} = 0$$

However, this quantity can be expressed as follows

$$\frac{d}{dt}\hat{B} - \frac{d}{dt}\begin{pmatrix} B_x \\ B_y \\ B_z \end{pmatrix} = \left(\frac{\partial(B)_b}{\partial\mathcal{B}_b}\right) \left(\hat{V} - \begin{pmatrix} u \\ v \\ w \end{pmatrix}\right) - \ell_1 \left(\frac{\partial(B)_b}{\partial\mathcal{B}_b}\right) \left(\frac{\partial(B)_b}{\partial\mathcal{B}_b}\right)^T \left(\hat{B} - \begin{pmatrix} B_x \\ B_y \\ B_z \end{pmatrix}\right)$$

which yields, using $\hat{B} - \begin{pmatrix} B_x & B_y & B_z \end{pmatrix}^T = 0$,

$$0 = \hat{V} - \begin{pmatrix} u \\ v \\ w \end{pmatrix}$$

To conclude, if the Jacobian $\left(\frac{\partial(B)_b}{\partial\mathcal{B}_b}\right)$ is non singular, and in practice it usually is due to the magnetic field disturbances, the observer reconstructs the value of the field $\begin{pmatrix} B_x & B_y & B_z \end{pmatrix}^T$ and the velocity $\begin{pmatrix} u & v & w \end{pmatrix}^T$ expressed in the body frame of coordinates \mathcal{R}_b . ■

The proposed state observer (2.10) reconstructs the magnetic field and most importantly the velocity, both expressed in the body frame \mathcal{R}_b . The required measurements are: the magnetic field (output measurement), the Jacobian of the magnetic field in the body reference frame (input measurement) and the rate of turn of the rigid body with respect to the inertial reference frame (input measurement). All of them are also expressed in the body frame \mathcal{R}_b , which means that the sensors are strapdown sensors aboard the rigid body. One shall note that the observer proposed above can also be studied in non-autonomous cases, i.e. accounting for the time-dependence of the dynamics. Following [69], invariance principle can be invoked, but trajectories of the system are not invariant sets. Another argument of uniform observability must be used, which can be established from uniform complete observability arguments stemming from uniform bounds on the observability Grammian, or

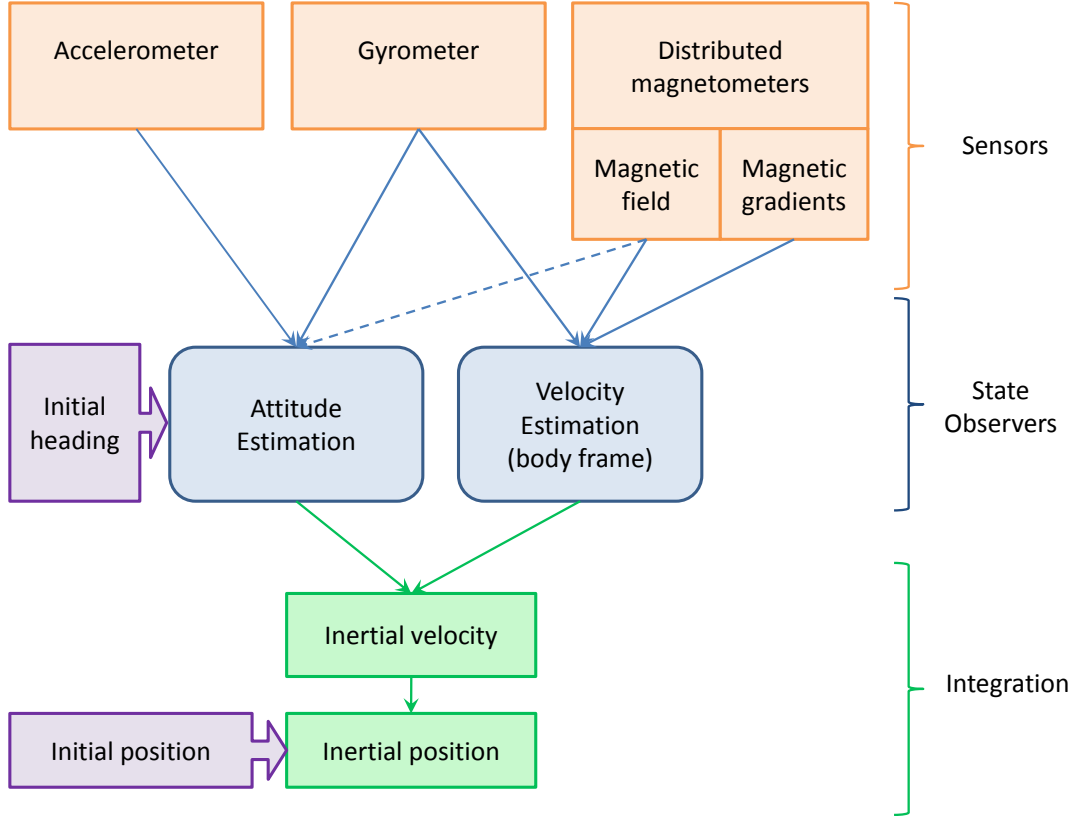


Figure 2.3: Trajectory reconstruction with a MINAV system.

arising from differential observability properties [19]. Such a proof of convergence accounting for the time-dependence of the dynamics is proposed in Appendix C.

The actual objective is to determine the trajectory of the rigid body in the reference frame \mathcal{R}_i . However, the body velocity cannot be processed by a numerical integration directly in the inertial reference frame. The proposed filter estimates $(V)_b = \left(\frac{dV}{dt}\bigg|_{\mathcal{R}_i}\right)_b$. It has to be first expressed in \mathcal{R}_i . Attitude information is necessary to appropriately project the velocity in the reference frame. Estimating the attitude from MEMS inertial sensors measurements (accelerometers and gyroscopes) is a classic problem that have already been thoroughly studied (see e.g. [12, 27, 54, 75]). The ground principles of such an attitude reconstruction can be found in Appendix F. However, as mentioned in Section 1.3, with low-precision inertial sensors, the heading is unobservable. It has to be integrated from a known initial heading provided by the user or given by a magnetometer when the Earth magnetic field is not disturbed (which is not so simple since the disturbances are required to get a velocity estimate). The attitude is then used to convert the body velocity to a velocity in the inertial reference frame where it can be integrated from an initial position provided by the user to get a position in that frame. Figure 2.3 details the successive steps of the trajectory reconstruction.

One can note that the velocity reconstruction described in this chapter does not require any a priori knowledge (such as a map) about the magnetic field nor its spatial variations. In

Place	Magnetic field	Magnetic gradient	Magnetometer technology
Geo Transfer Orbit (i.e. about 600 km of altitude)	0.1 G	100 nG/m	SQUIDs
Drilling wells	0.5 G	10 μ G/m	Fluxgate
Street, boulevard	0.5 G	50 mG/m	Magneto-resistive / GMR
Office building	0.5 G	50 mG/m	Magneto-resistive / GMR

Table 2.1: Magnetic field and gradient in various places.

this aspect, the presented technique differs greatly from the principle of magnetic anchors [15] or magnetic mapping [50, 102] that is often associated to navigation using magnetic fields (see also Chapter 5)

2.3 Properties of the magnetic field of importance for the MINAV technique

2.3.1 A disturbed field with easily measurable gradients

According to the principles of Magneto-Inertial Navigation (MINAV) presented in Section 2.2, one could have chosen any vector field to implement the velocity reconstruction technique presented, provided it is a non-uniform field in the area of interest (i.e. its Jacobian is nowhere singular in this region). However, not all field are as adapted as the magnetic field. It is a field that can be measured by many different techniques at various scales: at the surface of the Earth, in low-altitude orbit, or in deep off-shore wells (see e.g. [94] for more insight into the existing measurement techniques). Very importantly, the magnetic field presents spatial variations at these different scales, and the sensors to measure them are available. Table 2.1 reports some examples and details the observed magnitude of the magnetic field, its gradients and relevant sensors.

Interestingly, the price of the sensors is well-suited with the envisioned applications. Available magnetic sensor technologies are of various types. A list of them along with their ranges of measurement is reported in Figure 2.4 (found in [72]). In this figure, \overline{E} stands for the Earth magnetic field. We refer the reader to [72, 94] for a complete description of the various types of sensors, which are each exploiting a distinct type of connection between magnetic and electric phenomena. Among these technologies, the Anisotropic Magneto Resistance (AMR), considered in the application of this thesis, is a rugged, reliable and cheap choice, capable of providing an accurate estimate of the vector components of the ambient magnetic field and their gradients, which are required for pedestrian navigation (in buildings and streets). On the other hand, the SQUIDs magnetometers are more expensive and more difficult to use, but lie in the price range usually considered for orbital navigation. Section 2.3.4 provides more insight into the application of MINAV to that particular field.

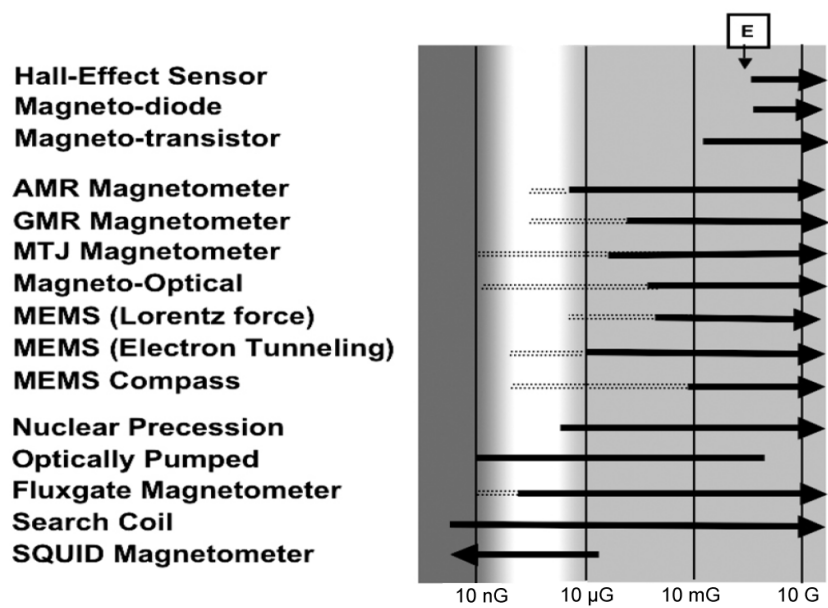


Figure 2.4: Various magnetometer technologies and their sensitivity. Source: [72]

\boxed{E} : Earth magnetic field

2.3.2 Differential calculus properties

As shown in Section 2.2, any non-uniform vector field can be used to estimate the body velocity. The magnetic field is not only a suitable choice since its gradients can be measured at different scales for different applications as mentioned in Section 2.3.1, but it also has some properties that can be used to simplify the measurement system. The magnetic is governed by Maxwell's equations [40, 41, 62, 78] (as well as the electric field). In the case of stationary vector fields considered so far, and in absence of electric charges (for the case the electric field is considered), the divergence of both electric and magnetic field are zero.

$$\nabla \cdot B = 0$$

$$\nabla \cdot E = 0$$

It means that the trace of their respective Jacobian matrix is zero. The number of independent terms in the Jacobian matrix of B is thus down from 9 to 8.

The other two Maxwell's equations express the curl of the magnetic and electric fields with respect to the time-derivative of the electric and magnetic fields, respectively.

$$\nabla \times E = - \frac{\partial B}{\partial t}$$

$$\nabla \times B = \mu_0 j + \frac{1}{c^2} \frac{\partial E}{\partial t}$$

where j stands here for the current density and c for the velocity of light. In the case of stationary fields, and in absence of currents within the measurement area, both curls are zero

$$\nabla \times E = 0$$

$$\nabla \times B = 0$$

This last property on the curl yields that the Jacobian matrix is symmetric in the case of stationary fields and in absence of current in the measurement area. In addition to the null trace given by the zero divergence, the number of independent terms in the Jacobian matrix is now down from 8 to 5. Notice that, if all the gradients with respect to any two space coordinate are known, the gradients with respect to the last space coordinate are computable from the other gradients.

2.3.3 Relations with the electric field

The assumption that the perturbed magnetic field is stationary can be considered, in some applications, as restrictive. There are two main cases that can be readily addressed though. We now detail them.

Time-periodic perturbed magnetic field

In the close vicinity of electric sources, the magnetic field can contain a relatively dominant periodic component at the 50 Hz frequency (60 Hz in the USA). This is also true for the electric field as has been experimentally studied in [66]. Therefore, one has to deal with a field of the form

$$B(X, t) = A(X) \cos(\omega t + \phi(X))$$

where w is the pulsation corresponding to 50 Hz, $A(X)$ is the space-dependent vector magnitude of the field, and ϕ is an unknown phase. Electric sources being quite synchronized (the speed of propagation between them being the speed of light), the phase ϕ is almost uniform and is therefore considered as constant. The w pulsation being known, it is relatively easy to extract the magnitude $A(X)$ from it. We take as simplifying assumption that $A(X)$ is always positive². Then, the chain-rule differentiation formula at constant \mathcal{R}_i gives

$$\left. \frac{dA}{dt} \right|_{\mathcal{R}_i} = \left(\frac{\partial A}{\partial X} \right) V$$

with

$$V = \left. \frac{dX}{dt} \right|_{\mathcal{R}_i}$$

However, the derivative of A is more useful in the reference frame of the sensors, \mathcal{R}_b . One has

$$\left. \frac{dA}{dt} \right|_{\mathcal{R}_b} = -\Omega_{b/i} \wedge A + \left. \frac{dA}{dt} \right|_{\mathcal{R}_i}$$

which yields

$$\left. \frac{dA}{dt} \right|_{\mathcal{R}_b} = -\Omega_{b/i} \wedge A + \left(\frac{\partial A}{\partial X} \right) V$$

with

$$A(X) = \sqrt{\frac{2}{T} \int_{t-T}^t B(X, u)^2 du}$$

component-wise, where $T = 1/50$.

The observer developed earlier for the steady magnetic field can be readily generalized to the magnitude A . Several sensors can be used to measure A at distributed locations, permitting to evaluate the Jacobian of this variable.

Another generalization is possible, directly working on the sensed field, and not on the magnitude, but accounting for the periodic nature of the sensed field. We now briefly expose it. Considering, as a simplifying assumption, a null phase, then one has

$$B(X, t) = A(X) \cos(wt)$$

which gives, by a time derivation

$$\begin{aligned} \left. \frac{dB}{dt} \right|_{\mathcal{R}_i} &= \left(\frac{\partial A}{\partial X} \right) V \cos(wt) - A(X)w \sin(wt) \\ \left. \frac{dB}{dt} \right|_{\mathcal{R}_b} &= -\Omega_{b/i} \times A(X) \cos(wt) + \left(\frac{\partial A}{\partial X} \right) V \cos(wt) - A(X)w \sin(wt) \end{aligned}$$

²In the general case where the components $A(X)$ are not always positive, their sign can be recovered thanks to the time origin chosen, by looking directly at the components of B at the beginning of each period.

It can be shown, using Barbalat's lemma to address the time-varying Lyapunov analysis, that the asymptotic observer permits to reconstruct the velocity

$$\begin{cases} A(X) = \sqrt{\frac{2}{T} \int_{t-T}^t B(X, u)^2} & (\text{component-wise}) \\ \dot{\hat{B}} = -\Omega_{b/i} \times \hat{B} + \left(\frac{\partial(A)_b}{\partial \mathcal{B}_b} \right) \hat{V} \cos(\omega t) - A(X) \omega \sin(\omega t) - \ell_1(\hat{B} - (B)_b) \\ \dot{\hat{V}} = -\Omega_{b/i} \times \hat{V} - \ell_2 \left(\frac{\partial(A)_b}{\partial \mathcal{B}_b} \right)^T \cos(\omega t) (\hat{B} - (B)_b) \end{cases}$$

The vector A is computed by the time-average of measurements performed at any particular point. Implicitly, it is assumed that the motion of the rigid body under consideration in the navigation problem is slow compared to the 50 Hz oscillations (this is quasi-static motion assumption). As in the usual case, the Jacobian $\left(\frac{\partial(A)_b}{\partial \mathcal{B}_b} \right)$ can be calculated using a set of spatially distributed sensors. The preceding analysis can be readily transposed to a set of electrometers [66].

Compensating magnetic field unsteadiness with electric field measurement

When no particular periodicity of the time-varying magnetic field signal can be assumed, it is possible to compensate its unsteadiness by an extra measurement. According to a chain rule differentiation, one has, for the sensed magnetic field B

$$\begin{aligned} \left. \frac{dB(X(t), t)}{dt} \right|_{\mathcal{R}_i} &= \left(\frac{\partial B(X(t), t)}{\partial X} \right) V + \left. \frac{\partial B(X(t), t)}{\partial t} \right|_{\mathcal{R}_i} \\ \left. \frac{dB(X(t), t)}{dt} \right|_{\mathcal{R}_b} &= -\Omega_{b/i} \times B(X(t), t) + \left(\frac{\partial B(X(t), t)}{\partial X} \right) V + \left. \frac{\partial B(X(t), t)}{\partial t} \right|_{\mathcal{R}_i} \end{aligned}$$

Similarly, for the sensed electric field, one has

$$\left. \frac{dE(X(t), t)}{dt} \right|_{\mathcal{R}_b} = -\Omega_{b/i} \times E(X(t), t) + \left(\frac{\partial E(X(t), t)}{\partial X} \right) V + \left. \frac{\partial E(X(t), t)}{\partial t} \right|_{\mathcal{R}_i}$$

These two equations can be related thanks to Maxwell's equations of electromagnetism (see e.g. [40, 41, 62])

$$\begin{aligned} (\nabla \times E) &= - \left. \frac{\partial B}{\partial t} \right|_{\mathcal{R}_i} \\ (\nabla \times B) &= \mu_0 \epsilon_0 \left. \frac{\partial E}{\partial t} \right|_{\mathcal{R}_i} \end{aligned}$$

Then, one gets

$$\left. \frac{dB}{dt} \right|_{\mathcal{R}_b} = -\Omega_{b/i} \times B + \left(\frac{\partial B}{\partial X} \right) V - \nabla \times E$$

This shows that the extra term in the equations governing the time variations of the measurements of magnetometers can be deduced from a reading of the electric field. A combination of distributed magnetometers and an electric field sensor could then be used to address the navigation problem in an unsteady disturbed magnetic field.

2.3.4 A field exploitable at various spatial scales

To illustrate the versatility of the MINAV methodology, we now consider a relatively extreme case, dealing with a spacecraft. As will appear, the magnetic field of the Earth can be exploited for the navigation problem of space vehicles orbiting or transiting in the neighborhood of this celestial body (typically, at a distance below 36 000 km). According to the literature on modeling the Earth magnetic field [85, 106], e.g. IGRF-2011 [42], the field is time invariant in the Earth frame of reference which is rotating with the Earth along a known axis. We refer the reader to [85, 89], for a description of the Earth magnetic field as an internal source model expressing the field as the gradient of a scalar potential given under the form of a spherical harmonic expansion with respect to spherical geocentric coordinates. To account for the rotation of the Earth, an additional frame of reference is introduced.

Consider an Earth attached frame of reference, referred to as $\mathcal{R}_t = (O_i, \mathcal{B}_t)$ where O_i is the center of an inertial frame of reference \mathcal{R}_i , and \mathcal{B}_t is a direct orthonormal triaxis rotating with the Earth. We consider $\mathcal{R}_i = \mathcal{R}_g$ the inertial frame of reference (geocentric) and \mathcal{R}_b , and the body frame of reference, respectively. The time variations of the sensed magnetic field are given by the projection of the following chain-rule vector equation onto the \mathcal{R}_b reference frame

$$\left. \frac{dB}{dt} \right|_{\mathcal{R}_b} + (\Omega_{b/i} - \Omega_{t/i}) \wedge B = \left(\frac{\partial B}{\partial X} \right) (V - \Omega_{t/i} \wedge X)$$

where $\Omega_{b/i}$ and $\Omega_{t/i}$ (a known constant vector) are the vector rotation of \mathcal{R}_b with respect to \mathcal{R}_i and the vector rotation of \mathcal{R}_t with respect to \mathcal{R}_i , respectively. In this equation, $\frac{\partial B}{\partial X}$ is the Jacobian of the magnetic field, while V is the velocity with respect to \mathcal{R}_i . The projection of this vector equation onto the \mathcal{R}_b reference gives

$$\begin{bmatrix} \dot{B}_x \\ \dot{B}_y \\ \dot{B}_z \end{bmatrix} + \left(\begin{pmatrix} p \\ q \\ r \end{pmatrix} - P_{i \rightarrow b} \begin{bmatrix} 0 \\ 0 \\ \omega_t \end{bmatrix} \right) \wedge \begin{bmatrix} B_x \\ B_y \\ B_z \end{bmatrix} = \left(\frac{\partial (B)_b}{\partial \mathcal{B}_b} \right) \left(\begin{bmatrix} u \\ v \\ w \end{bmatrix} - P_{i \rightarrow b} \left(\begin{bmatrix} 0 \\ 0 \\ \omega_t \end{bmatrix} \wedge \begin{bmatrix} x \\ y \\ z \end{bmatrix} \right) \right) \quad (2.11)$$

In this expression, the vector $\begin{pmatrix} p & q & r \end{pmatrix}^T$ contains the readings of the embedded gyroscope, ω_t is the scalar defining the rotation rate of the Earth, $\begin{pmatrix} B_x & B_y & B_z \end{pmatrix}^T$ is the vector containing the readings of the embedded magnetometer, $\left(\frac{\partial (B)_b}{\partial \mathcal{B}_b} \right)$ is the matrix containing the partial derivatives of the readings of the embedded magnetometer with respect to the body reference frame \mathcal{R}_b , $\begin{pmatrix} u & v & w \end{pmatrix}^T$ is the vector containing the coordinates of V projected in \mathcal{R}_b , and $\begin{pmatrix} x & y & z \end{pmatrix}^T$ is the vector containing the coordinates of X the position of the rigid body with respect to \mathcal{R}_i projected onto \mathcal{R}_i . The matrix $P_{i \rightarrow b}$ is the transition matrix from \mathcal{R}_i to \mathcal{R}_b .

To obtain the above equation, three frames of reference have been used. Compared to the other applications where only \mathcal{R}_i and \mathcal{R}_b are considered, it has been necessary to introduce the \mathcal{R}_t reference frame to invoke the stationarity of the Earth magnetic field, which holds only in this frame of reference and not in \mathcal{R}_i .

The equation relating the readings of magnetometers and gyroscopes is more complicated than usual. The rotation of the Earth is accounted for through the term ω_t . Another variable also come into play: the position. In the application envisioned in [89], this information is provided by the reference IMU of the space vehicle. In this case, the principle of MINAV applies, as Equation (2.11) is used once again to estimate the velocity V . This represents a new form of hybridation of sensors aboard a space vehicle.

A complete evaluation of the benefits of the application of MINAV for a heavy launcher (e.g. Ariane 5) along a typical Geosynchronous Transfer Orbit (GTO) is provided in [89], which shows that using highly sensitive magnetic sensors (in particular SQUID technology) the velocity could be estimated with an error below 1 m/s during the whole flight mission. In turn, this could improve the current launch vehicle navigation accuracy by a factor of 10 to 100. The potential gain is related to the magnitude of the magnetic field gradient observed along the trajectory, and the accuracy of the employed magnetic and inertial sensors.

Chapter 3

Design of MINAV systems

Conception de systèmes MINAV

Ce chapitre s'intéresse à la conception d'un système MINAV. L'un des points clés est la mesure de la Jacobienne du champ magnétique. En effet, c'est par elle que la vitesse est observable. En pratique, cette Jacobienne est calculée par différences finies à partir des mesures d'un jeu de magnétomètres spatialement répartis. La synchronisation de ces mesures et la connaissance précise de la distance entre les capteurs sont primordiales. Il faut pouvoir distinguer si l'écart entre les mesures de deux magnétomètres est dû à une variation spatiale du champ ou bien à des données prises à des instants différents lors du déplacement. La Section 3.1 traite ce problème de datation des données. L'évaluation précise de la distance entre les capteurs est explicitée en Section 3.2.

Nous nous intéressons ensuite au dimensionnement du système, c'est-à-dire au choix de la fréquence d'échantillonnage, à la précision des capteurs et à leur espacement en fonction des plages de valeurs attendues pour les gradients magnétiques et la vitesse. Une analyse de l'erreur est conduite en Section 3.3.

L'introduction du schéma de différences finies entraîne l'apparition de singularités près des points où le champ magnétique présente des extrema. L'impact de ces singularités est étudiée en Section 3.4.

Enfin, un système de mesure complet et adapté à un système MINAV est présenté en Section 3.5.

The principles of magneto-inertial navigation (MINAV) have been detailed in Chapter 2. Their practical implementation raises some important issues that are addressed in this chapter.

According to Proposition 3 of Chapter 2, the measurements that are necessary to implement the MINAV method are: one output measurement, the magnetic field vector, and two input measurements, the (vector) rate of turn, and the Jacobian of the magnetic field. We make the distinction of input versus output measurement, due to their respective roles in the proposed velocity reconstruction observer detailed in Proposition 3. In practice, a 3-axis gyrometer is used to measure the rate of turn and a set of spatially distributed magnetometers

is used to derive both the magnetic field and its Jacobian matrix. The measurement of this Jacobian is a key-point since the velocity owes its observability to it. In practice, the nine partial gradients of the Jacobian are estimated with an array of magnetometers and a finite difference scheme. The properties of the magnetic field mentioned in Section 2.3.2 allows to compute only 5 terms out the 9 and to determine the remaining ones knowing that the Jacobian matrix is symmetric and that its trace is zero. In particular, a complete column of this matrix can be reconstructed, allowing to distribute the sensors only in a plane, reducing greatly the space required for the measurement system. Here, however, we consider that all the terms are measured in a way similar to the following 2-dimensional example.

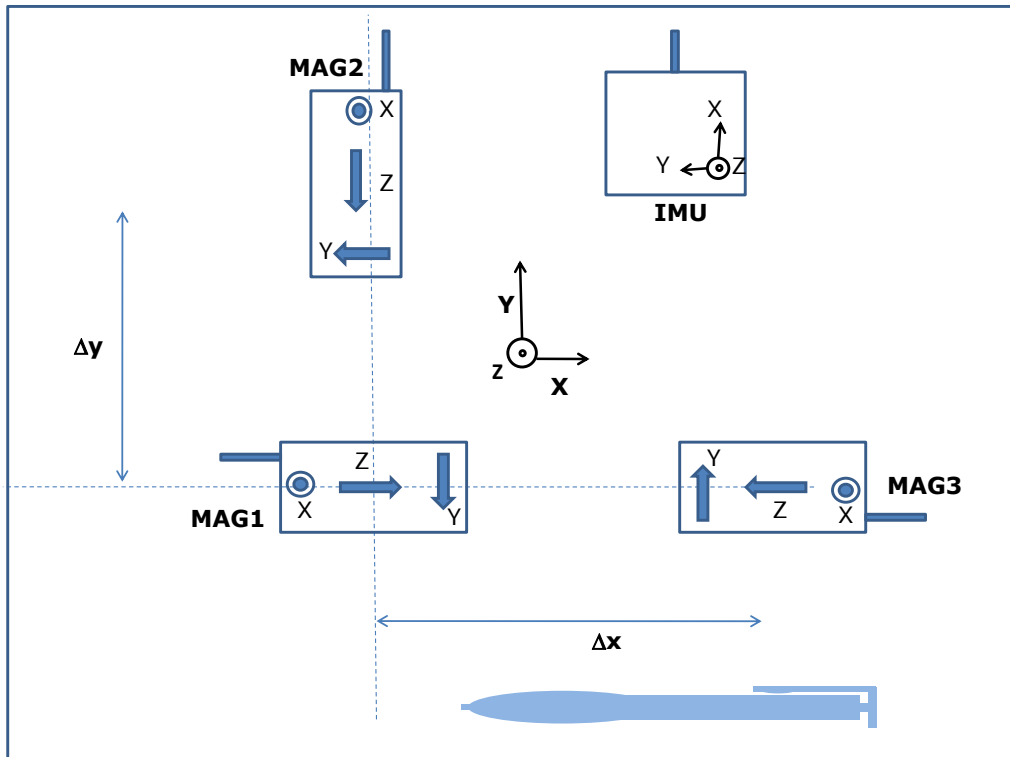


Figure 3.1: Schematic of a 2-dimensional sensing module, with three 3-axis magnetometers and an inertial measurement unit (IMU) gathering a 3-axis gyrometer and a 3-axis accelerometer.

In a simple 2-dimensional case, the 2×2 Jacobian is computed from the measurements of the three magnetometers. Denote $M_i = (M_{i,x}, M_{i,y})$ the values given by the i^{th} magnetometer (in the body frame). For example, the three magnetometers are located according to the schematic on Figure 3.1. A first approximation of the Jacobian is then

$$J = \begin{pmatrix} \frac{M_{3,x} - M_{1,x}}{\Delta x} & \frac{M_{2,x} - M_{1,x}}{\Delta y} \\ \frac{M_{3,y} - M_{1,y}}{\Delta x} & \frac{M_{2,y} - M_{1,y}}{\Delta y} \end{pmatrix} \quad (3.1)$$

where Δ_x is the distance between the sensors of magnetometers 3 and 1 which are both aligned on the x -axis, and Δ_y the distance between the sensors of magnetometers 2 and 1 which are aligned on the y -axis.

Having a precise estimation of the Jacobian through such a finite difference scheme requires to take care of the synchronization between the sensors and to have a precise knowledge of the distance between the sensors. Those two key points are detailed in Section 3.1 and Section 3.2.

Once one knows how to precisely estimate the Jacobian of the magnetic field, attention is given to the dimensioning of the system, which consists in choosing a proper sampling time, appropriate sensors sensitivity, and the right spacing to account for the fact that the magnetic gradients and velocity to estimate take values in a given and known range. An error analysis is performed in Section 3.3.

As will appear, the introduction of spatial finite differences schemes introduces singularities near extremal points of the fields. Their impact is investigated in Section 3.4.

Finally, a full measurement system suitable for a MINAV system is presented in Section 3.5.

3.1 Preliminary requirement: timestamping of the digital measurements

In most embedded positioning devices (see e.g. [20]), information is repeatedly collected from the sensors at successive time steps. Data is processed in a main loop and little care is given to the time delays between the various sensors. Implicitly, those delays are assumed to be negligible. In a MINAV system, however, the set of magnetometers is used to compute the Jacobian of the magnetic field by use of a finite difference scheme. More than the value of the field, the key information lies in its variations, and the difference of values sensed by the sensors of the set. Therefore, it is of paramount importance to distinguish between the variations due to the fact that the sensors are indeed positioned at slightly different places, and the variations due to measurements being taken at different dates during the movement.

To illustrate this point, assume that there are only 2 sensors moving one behind the other along a straight line. The distance between the two sensors is about 10 cm, the velocity of the system is about 1 m/s, and measurements are taken at 50 Hz. If the measurements are not performed on both sensors at the same time, the time interval between the 2 measurements can be up to $1/50 = 20$ ms which represents a displacement of 2 cm, i.e. twenty percents of the distance between the sensors, leading to an error close to 20 percent on the computed gradient. A better precision can be reached by taking care of the measurement date.

Depending on the sensors available, whether they are analog sensors or digital sensors, several techniques may be envisioned to determine the date of the measurements. One of the worst case scenario appears when the set of sensors consists of digital sensors, each one of them running its own clock without any external trigger. Note that many low-cost sensors present such a behavior, even if it is not obvious at first sight. Some of them indeed provide a misleading “upon request” operating mode. This terminology is misleading because one would assume that, in this mode, the measurement tasks are performed exactly when they are asked. However, careful investigation of a few sensors revealed a different mechanism. The sensor continuously performs periodic measurements, and delivers the latest one whenever a data request is made. The date may thus vary within a time-interval as large as the period

of the sensors internal clocks, which is what one wishes to avoid. HMR magnetometers from Honeywell [57] or Microstrain's IMU [80, pp 9-10], for instance, present such a behavior. With such sensors, data synchronization is almost impossible.

The approach proposed hereafter is a robust way to deal with such sensors by assigning a timestamp to each measurement, while being careful of not overwhelming the microcontroller which gathers all the measurements. Such overwhelming of the microcontroller would inevitably bring new dating issues or even data losses. The sensors are set to a continuous output mode in which they continuously deliver measurement information as soon as it is available (i.e. right after the physical measurement). Provided that the microcontroller reacts at the exact time when this information is received (at least a time small before the accuracy of the dating one wishes to achieve), and stores the date of reception as a timestamp along with the data, then there is no uncertainty in the actual timestamping of the measurements. A reaction from the microcontroller at the exact time the information arrives is not achievable because of timing jitter at the microcontroller level. The jitter depends on the interrupt model but is still present. However, a lower precision can be achieved which is already better than 1/10 of the sensor period (a few tenth of milliseconds instead of several milliseconds in the system presented in Section 3.5). The method is now detailed a bit further on an example with a set of HMR magnetometers from Honeywell and an IMU from Microstrain.

Unlike the magnetometers, the IMU, which can be considered as a regular clock, provides accurate timing information, included in its output message. The IMU is taken as a reference clock (if it is not the case, any internal or external clock can be used). Next, we proceed in two steps. *i*) whenever a sensor (excluding the IMU) measurement has been received, the microcontroller measures the time elapsed from the latest IMU measurement. This timestamp is then included in the output message of the microcontroller along with the value of the measurement, *ii*) the timestamp is then corrected depending on the sensor. There is indeed a certain amount of time elapsed between the actual measurement at the sensor level and the arrival of a message with that measurement at the microcontroller level. These two steps are now detailed.

Timestamping at the microcontroller level

The reference clock is the IMU clock. The IMU tick count is included in its messages. The microcontroller clock is used to measure the time elapsed between an IMU message and the reception of measurements from all the magnetometers. The information from all sensors is obtained under the form of messages received through various UART ports using dedicated interrupt handler routines.

To maximize performance, the task performed inside the interrupt handler routines is limited to the following: to get the data and store the timestamp (for the first byte of data of each message only). The interrupt subroutine, which is pictured in Figure 3.2, is exited as soon as possible, allowing other interrupts to come into play. Further tasks are done afterwards in the main loop. These include checking the validity of the message when a checksum is available, and converting the stored acquisition timestamps into timestamps relative to the IMU clock. Finally a single output message containing both sensors data and their timing information is formulated. The main software architecture is detailed in Figure 3.3. The gathered message contains: *i*) data collected from the various sensors. *ii*) an absolute timestamp given by the IMU reference clock. *iii*) a relative timestamp for every sensor data. This represents the time difference between the reception of the sensor

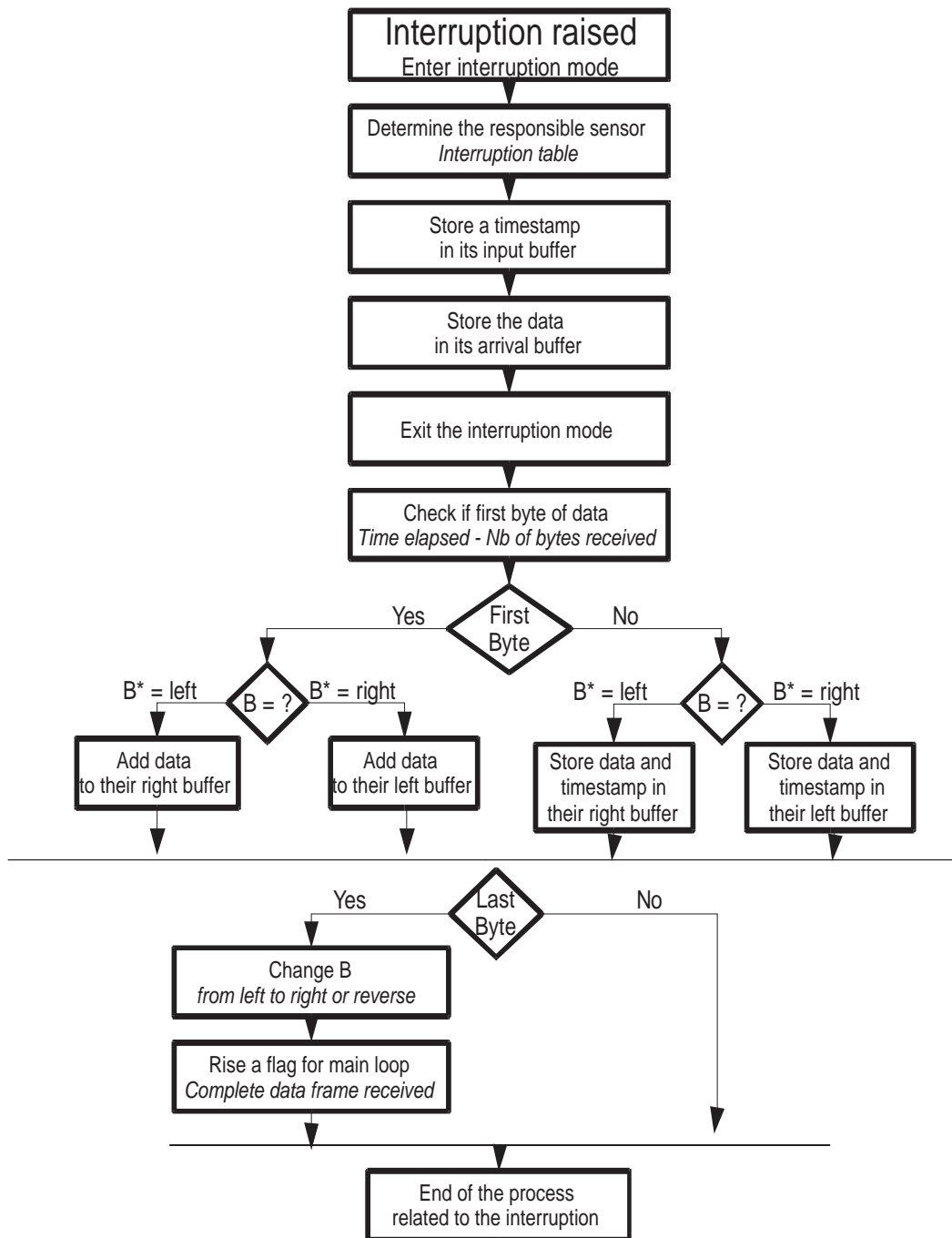


Figure 3.2: Interrupt management: the interrupt mode is left as soon as possible in order to avoid delaying another interrupt. Two buffers (left and right) are used. At any given time, one is full of available data (the last complete data frame received) and ready to be read, whereas the other is being written with new data.

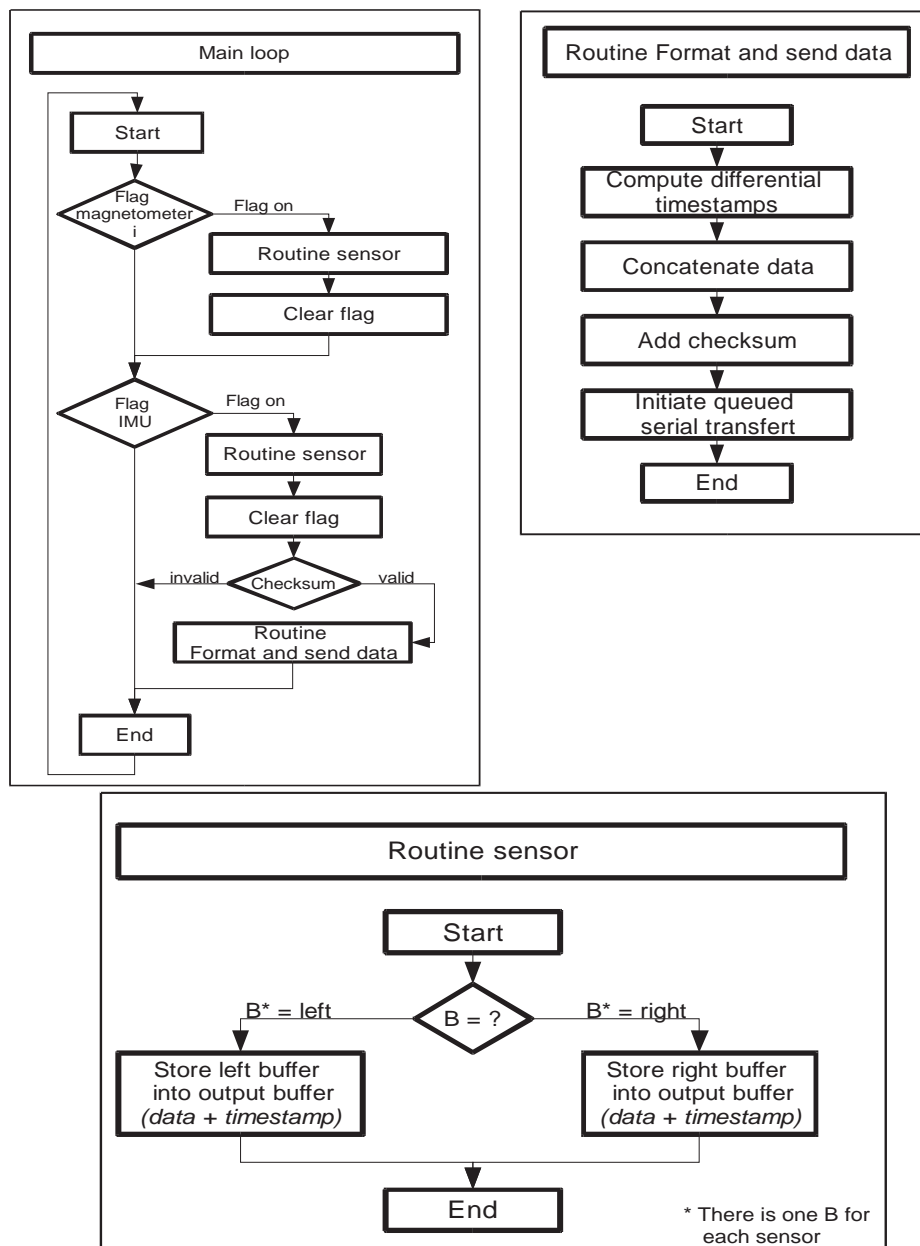


Figure 3.3: Software main loop. Three buffers are used for each sensor: `buffer_right`, `buffer_left`, and `buffer_output`. The first two are used so that the last complete frame is stored in one of them while the other one is being written or ready to be written. When an IMU frame is complete, the last available data from each sensor is stored in the corresponding output buffer. This is a way to freeze all of the values that will be sent while the differential timestamps are computed and the output message is concatenated.

measurements by the microcontroller and the acquisition of the data from the IMU contained in the same output message.

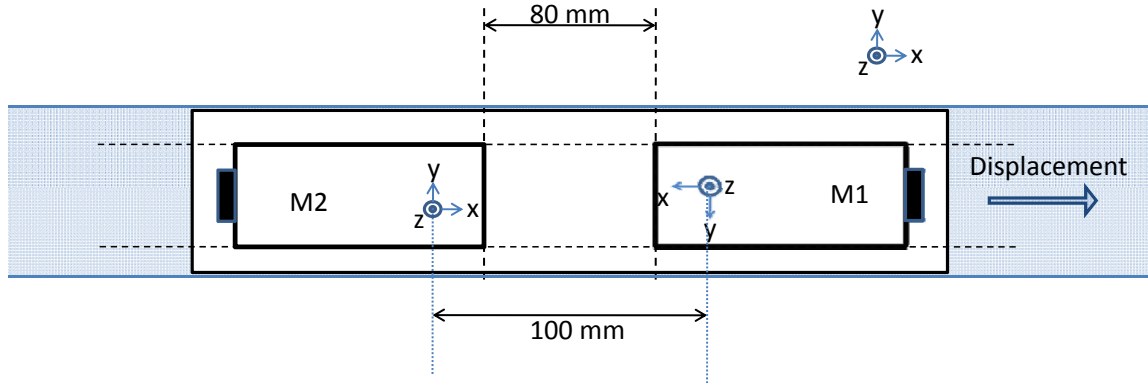


Figure 3.4: Two sensors aligned in the direction of the rail. The sensing parts of each axis are at distinct locations of the outer box.

Delay between measurement and acquisition

Physically, an additional pure delay due to the sensor itself has also to be taken into account. This delay is caused by internal computations performed at the sensor level to compensate for drift due to temperature changes, conversion of voltages into variables of interest, and transmission delays. This point is supported by an experiment where the sensors have been moved quickly from one steady position to another. Data sheets can provide a first estimate of this delay, but large deviations are expected (at least for low-cost sensors). For the magnetometers, an offline identification easily yields an estimate of this delay. The magnetometer responds in a few tenths of a millisecond, and the IMU reacts slightly later. The delay between the IMU and the magnetometers can be easily determined.

Finally, note that no real, absolute time information can be obtained. The internal clock of the IMU, which was taken as a reference, is accessible after a delay which can be estimated but not completely determined. There remains a small uncertainty in the origin of the time scale. However, an accurate relative timing of all the measurements can be achieved with this method. Those relative dating is the one that really matters when it comes to computing the Jacobian of the magnetic field by a finite difference scheme.

3.2 Identification of the distance between sensors

In Equation (3.1), now that the measurements have been synchronized, it is necessary to know Δx and Δy to estimate the Jacobian. These parameters need to be well identified, otherwise the true terms of the Jacobian will be always overestimated or underestimated. A rough estimate of the spacing between the sensors is naturally given by the distance between the outer box of the two sensors. However, performing an accurate measurement of the distance that way can reveal rather inaccurate, and knowing precisely where the sensing part of the sensor lies, for a given axis, is not truly possible. We propose hereafter a simple method to estimate these parameters.

Consider a straight rail and set the system on the rail such that the two sensors are aligned in the direction of movement along the rail as depicted in Figure 3.4. In that configuration, one of the sensors follows the other one as the system is translating along the rail. The measurements made by the two sensors are thus the same with a shift in time. This time shift has to be converted in a distance. One can proceed as follows. Every 4 seconds, the platform is moved 1 cm (or less)¹ forward until the end of the rails is reached. By identification of the sensors output records, it is thus easy to eliminate the time and get the profile of the field as measured by each sensor along the rail direction. To get better results, some pre-treatments are performed to eliminate as much noise as possible. We now detail them.

- A zero-phase digital filter [86] is applied to the set of data to lower the level of noise by smoothing them but without introducing detrimental delays.
- A value is associated to each step (one step every centimeter or less) for each sensor. This step simultaneously converts the time shift between the measurements into a distance and lowers the level of noise a bit further by averaging the measurements over a couple of seconds.

Finally, the distance between the sensors can simply be read as the shift between two curves, as illustrated on Figure 3.5.

3.3 Error analysis of velocity equation

A few simple guidelines are provided in this Section for a proper dimensioning of the system. They are based on an error analysis of Equation (2.6) where the velocity naturally appears. The first point to notice is that, the Jacobian of the magnetic field being computed by a finite difference scheme from a set of magnetometers, the sensors have to be accurate enough to measure not only the value of the field, but, more importantly, the small variations between the magnetometers around this value. Denote J_0 the smallest value of the gradient that has to be measured. Note that the value of the field is not monotonous, which means that the gradient vanishes sometimes. The impact of those points will be further analyzed in Section 3.4. If two single-axis sensors giving measurements M_1 and M_2 are distant of Δx and have a resolution of M_{min} , the smallest measurable gradient is

$$\frac{M_{min}}{\Delta x}$$

It yields the following constraint on the precision of the magnetometers

$$\frac{M_{min}}{\Delta x} \leq J_0$$

Consider the case of a pedestrian walking in an office building, where the typical order of magnitude of the gradient is 50 mG/m . One should be able to measure significantly smaller variation and thus choose a J_0 not greater than 10 mG/m . Then, depending on the

¹The value of the step has to be known, but can possibly vary from one step to another. The smaller and the more accurate the step is, the more precision on the spacing one obtains.

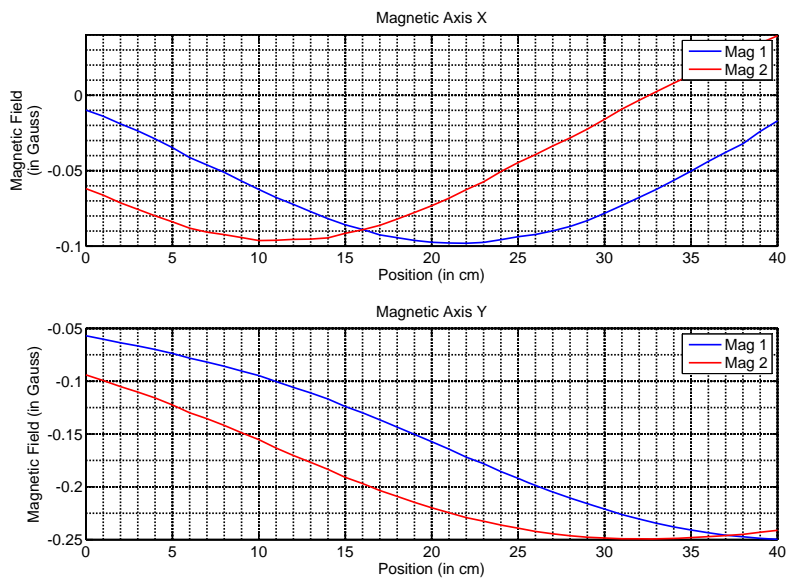


Figure 3.5: A board of two magnetometers is moved along the direction of alignment by small increments (here of 1 cm). This permits to construct two “magnetic maps” from the data of the two sensors. The distance between the sensors is the space-shift in their measurements. Results are reported for 2 sensing axes of the sensors.

resolution of the sensors available (e.g. 1 mG), a lower bound to the distance between the magnetometers is obtained.

$$\begin{aligned}\Delta x &\geq \frac{M_{min}}{J_0} \\ \Delta x &\geq 0.1 \text{ m}\end{aligned}\tag{3.2}$$

Inversely, in case of constraints on the size of the system (i.e. δ has to remain small), the requirement (3.2) bears on the resolution of the sensors.

To evaluate the accuracy of the velocity reconstruction, we now consider an error analysis. In the considered 1-axis case, Equation (2.6) writes

$$\dot{B} = J_B V\tag{3.3}$$

Taking the logarithm of Equation (3.3) and differentiating it yields the uncertainty equation

$$\frac{\Delta \dot{B}}{\dot{B}} = \frac{\Delta J_B}{J_B} + \frac{\Delta V}{V}$$

One obtains, for absolute errors,

$$\Delta V = V \left(\frac{\Delta J_B}{J_B} + \frac{\Delta \dot{B}}{\dot{B}} \right)\tag{3.4}$$

The first term is an error due to the gradient reconstitution while the second term depends on the estimation of the time derivative of magnetic field. The error ΔJ_B on J_B is essentially due to the resolution of the magnetometers used for the finite difference scheme, and the distance Δx between them

$$\Delta J_B \approx \frac{2M_{min}}{\Delta x}$$

Let us now focus on the second term of Equation (3.4). Given noisy measurements of B performed at discrete times, a question is to quantify the uncertainty $\Delta \dot{B}$ of reconstruction of \dot{B} . This is a problem of differentiation of a noisy signal. A possible solution to this question is brought by [22] under the assumption that B is a variable driven by an underlying continuous time dynamics fed with noise. Measurements of this continuous variable are performed at discrete times with additive noise. This is a mathematical problem statement representative of our case, since the encountered magnetic field is varying, and that the time variations can be modeled under the discussed form with a noise power that can be tuned to account for typical envisioned applications.

Applying the result of [22] to a double integrator fed with white noise with spectral density $\frac{\lambda_c}{2}$, measured at a sample rate f , with a corrupting white noise of variance $\lambda_v \ll \lambda_c$, the minimal estimator error variance (obtained by an optimal differentiation filter) is, neglecting aliasing phenomenon, given by the formula

$$E^2 \approx \frac{\lambda_c}{4\sqrt{3}f} + 6 \left(\sqrt{3} - 1 \right) \lambda_v f^2\tag{3.5}$$

Proof: According to the [22, corollary 1], one has

$$E^2 = \frac{\lambda_c}{2i\pi} \oint_{|z|=1} \left(\underbrace{\frac{L^c L^c}{\tau \beta \beta_*}}_I + \eta \underbrace{\frac{MM_* P_{22}}{\tau \beta \beta_*}}_{II} \right) \frac{dz}{z} \quad (3.6)$$

where L^c is solution of a linear polynomial equation involving $P_{i,j}$, N , β_* and D . (M, N) is the discrete transfer function modeling the dynamic measurement noise. Here, one has $(M, N) = (1, 1)$. (C, D) is the transfer function of the double integrator driven by the white noise modeling B . β and the scalar τ are defined by a spectral factorization involving N , D , M , and $P_{i,j}$. These $P_{i,j}$ are themselves defined with respect to H , the measurement transfer function, C , and R , the discrete covariance matrix of the dynamics of the continuous variable the derivative is being estimated. Finally, if q^{-1} is the backward shift operator, one notes $u_*(q^{-1}) = u(q)$. In the integral, z is substitute for q .

The first term (I) of Equation (3.6) accounts for the lag in the tracking of \dot{B} by the optimal differentiator, the second term (II) is related to the measurement noise. Both terms can be evaluated when $\eta = \frac{\lambda_v}{\lambda_c} \ll 1$, i.e. when the measurement noise is much smaller than the noise driving the dynamics of B . One has, with δt the sampling rate,

$$\begin{aligned} M &= N = 1 \\ D &= (1 - q^{-1}) \\ P_{11} &= \frac{\delta t^3}{6} (q^{-1} + 4 + q) \\ P_{22} &= \delta t (-q^{-1} + 2 - q) \\ \tau \beta \beta_* &= \frac{\delta t^3}{6} (q^{-1} + 4 + q) + \eta (2 - q - q^{-1})^2 \end{aligned} \quad (3.7)$$

When $\eta \ll 1$, the term (II) is thus

$$(II) \approx \frac{\lambda_v}{2i\pi} \oint_{|z|=1} \left(\frac{\delta t (-z^{-1} + 2 - z)}{\frac{\delta t^3}{6} (z^{-1} + 4 + z)} \right) \frac{dz}{z} \approx 6 (\sqrt{3} - 1) \frac{\lambda_v}{\delta t^2}$$

β , and then L have to be evaluated prior to estimate the term (I) in Equation (3.6). β is the result of a spectral factorization. Yet, closed-form expressions exist for second-order spectral factors [88]. In particular, [23, (3.7)] provides the expression in our particular case of interest. When $\eta \ll 1$, one obtains

$$\beta(q) = 1 + \frac{1}{2\sqrt{3}} \cdot q$$

Evaluating (3.7) at $q = 1$ yields

$$\tau = \frac{2 + \sqrt{3}}{6} \delta t^3$$

One can thus form the polynomial equation satisfied by L

$$\frac{\delta t^2}{2} q(1 + q^{-1}) - \tau \left(1 + \frac{1}{2 + \sqrt{3}} q \right) Q_0 = q(1 - q^{-1}) (L_0 + L_1 q)$$

Evaluating this polynomial at $q = 1$ yields

$$Q_0 = \frac{3 + \sqrt{3}}{(2 + \sqrt{3}) \delta t}$$

By identifying the coefficients of the two polynomials, one gets

$$L = L_0 = \frac{\delta t^2}{2\sqrt{3}}$$

The term (I) of Equation (3.6) can now be computed, still under the assumption that $\eta \ll 1$

$$(I) \approx \frac{3\lambda_c L_0^2}{i\pi\delta t^3} \oint_{|z|=1} \frac{dz}{z^2 + 4z + 1} \approx \frac{\lambda_c \delta t}{4\sqrt{3}}$$

Finally,

$$E^2 \approx \frac{\lambda_c \delta t}{4\sqrt{3}} + 6 \left(\sqrt{3} - 1 \right) \frac{\lambda_v}{\delta t^2} \quad , \quad \eta \ll 1 \quad (3.8)$$

■

Error estimate Gathering Equation (3.3), Equation (3.5) and Equation (3.8), one finally obtains the error estimate.

$$\Delta V \approx V \left(\frac{2M_{min}}{J_B \Delta x} + \frac{1}{B} \sqrt{\frac{\lambda_c}{4\sqrt{3}f}} + 6 \left(\sqrt{3} - 1 \right) \lambda_v f^2 \right) \quad (3.9)$$

This formula will be exploited in Section 3.5 on a particular case of application.

3.4 Impact of the time-discretization

In this section, we wish to stress the impact of evaluating the gradient of the magnetic field through a finite difference scheme. As will appear, this approximation plays a relatively involved role as singularities appear. Fortunately, this possibly malicious effect is circumvented by another source of approximation which is the time sampling. As a result of the cancellation of these effects, we formulate a *rule of thumb* for selecting the distance between sensors: *the distance between two sensors should be chosen such that, at all times, at most one extremum of the sensed field can be located in between the sensors.*

To illustrate this *rule of thumb*, we consider again a simple 1-dimensional case and establish an error estimate for the time sampled evaluation of an integral that equals the theoretical value of the displacement. Depending on the choice of the relative distance between the sensors, time sampling provides either a converging estimate or a diverging one. This problem is as follows.

The gradients of the magnetic field are measured thanks to a set of magnetometers by a finite difference scheme as the one proposed in Equation (3.1). To ease the analysis, it is assumed that the rigid body is moving (along a single axis) with a constant velocity of, e.g.

1 m/s. The position at $T=1$ s can be computed by Equation (2.6). which yields, after an integration

$$x(1) - x(0) = \int_0^1 \frac{d}{dt} \left(\frac{B(x(t))}{\nabla B(x(t))} \right) dt \quad (3.10)$$

where $x(0) = 0$ is the initial condition. In practical applications, the gradient $\nabla B(x)$ is (approximately) evaluated using two magnetometers. Those sensors are assumed to be ideal and flawless. We note $\Delta x > 0$ the distance between the two sensors.

Since we chose a unit velocity, at any given time t , the first sensor measures $B(x(t) + \frac{\Delta x}{2}) = f(t + \frac{\Delta x}{2})$ and the second one $B(x(t) - \frac{\Delta x}{2}) = f(t - \frac{\Delta x}{2})$ as pictured in Figure 3.6.

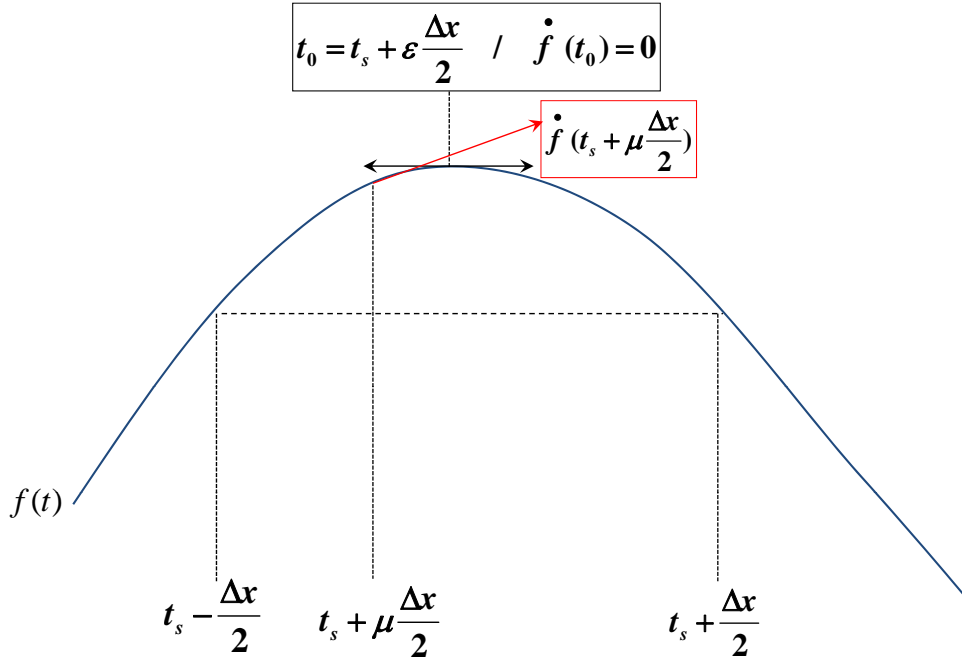


Figure 3.6: The different points of interest around the extremum.

With such a set-up, Equation (3.10) can be approximated in several ways (discretization schemes) parametrized by $\mu \in [0; 1]$

$$\int_0^1 f_\mu(t) dt = \Delta x \int_0^1 \frac{f'(t + \mu \Delta x / 2)}{f(t + \Delta x / 2) - f(t - \Delta x / 2)} dt \quad (3.11)$$

The parameter $\mu \in [0; 1]$ is used to express how the numerical scheme is centered. Negative values of μ could be considered as well by symmetry, but do not bring anything to the discussion. We are now interested in the integral (3.11) and we wish to determine conditions under which it is a good approximation of (3.10). In Equation (3.11), the denominator can vanish due to the presence of an extremum of f , which is assumed to be a smooth function $\mathbb{R} \rightarrow \mathbb{R}$. This singularity is first studied in terms of singularity in the function f_μ .

3.4.1 Order of the singularity created by the spatial discretization

When the magnetic field has a local extremum, the denominator of f_μ can vanish near the extremum. If Δx is small enough to have at most one extremum in any interval of length δ , it is always the case. Denote t_0 this extremum (of f) and t_s the point (singularity) where the denominator D of f_μ vanishes, i.e. where f_μ is singular. One has $t_0 \in [t_s - \frac{\Delta x}{2}; t_s + \frac{\Delta x}{2}]$. We parametrize under the form

$$t_0 = t_s + \epsilon \frac{\Delta x}{2}, \quad \text{with } \epsilon \in [-1; 1].$$

Now expand the denominator D of f_μ near the singularity

$$\begin{aligned} D(t) &= f\left(t + \frac{\Delta x}{2}\right) - f\left(t - \frac{\Delta x}{2}\right) \\ &= \underbrace{D(t_s)}_{=0} + (t - t_s) \left(\frac{\partial D}{\partial t} \right)_{t=t_s} + O((t - t_s)^2) \\ &= (t - t_s) \left(\dot{f}\left(t_s + \frac{\Delta x}{2}\right) - \dot{f}\left(t_s - \frac{\Delta x}{2}\right) \right) + O((t - t_s)^2) \end{aligned}$$

This gives

$$f_\mu(t) = \frac{\Delta x \dot{f}(t + \mu \Delta x / 2)}{(t - t_s) \left(\dot{f}(t_s + \Delta x / 2) - \dot{f}(t_s - \Delta x / 2) \right) + O((t - t_s)^2)} \quad (3.12)$$

From Equation (3.12), one has to distinguish several cases to determine the order of the singularity

- **Case A:** If $\mu = \epsilon$, i.e. $\dot{f}(t_s + \mu \Delta x / 2) = 0$, then a further expansion of the numerator yields

$$f_\mu(t) = \frac{\Delta x \ddot{f}(t_s + \mu \Delta x / 2) + O(t - t_s)}{\dot{f}(t_s + \Delta x / 2) - \dot{f}(t_s - \Delta x / 2) + O(t - t_s)}$$

A.1 If there is no other extremum over the interval $[t_s - \Delta x / 2; t_s + \Delta x / 2]$, then the first term of the denominator $\dot{f}(t_s + \Delta x / 2) - \dot{f}(t_s - \Delta x / 2) \neq 0$, and f_μ has a (finite) limit in t_s . The function f_μ is thus integrable over $[0; 1]$.

A.2 However, if there is one or more other extrema over $[t_s - \Delta x / 2; t_s + \Delta x / 2]$, then the first term of the denominator $\dot{f}(t_s + \Delta x / 2) - \dot{f}(t_s - \Delta x / 2)$ can vanish. Under this assumption, f_μ presents a singularity at least of order 1 in t_s .

- **Case B:** If $\mu \neq \epsilon$, i.e. $\dot{f}(t_s + \mu \Delta x / 2) \neq 0$, then, according to Equation (3.12), the function f_μ presents a singularity at least of order 1 in t_s .

B.1 If there is no other extremum over the interval $[t_s - \Delta x / 2; t_s + \Delta x / 2]$, then the first term of the denominator $\dot{f}(t_s + \Delta x / 2) - \dot{f}(t_s - \Delta x / 2) \neq 0$ and the singularity of f_μ is exactly of order 1.

B.2 If there are one or more other extrema over the interval, then the denominator can vanish. The singularity is then of order higher than one.

In practice, if the spacing between the sensors is small enough with respect to the variations of the magnetic field, there is at most one extremum over every interval of length Δx . Thus, case B.1 is the most common, and case A.1 may exceptionally arise when the gradient estimated by the finite different scheme and the temporal derivative of the magnetic field vanish at the same point (just as if a punctual magnetic gradiometer was available). This is hardly the case.

To move on to the evaluation of the integral of f_μ , we assume that case B.1 holds and note

$$f_\mu^*(t) = (t - t_s) f_\mu(t)$$

where f_μ^* is smooth at t_s (and smooth over $[0; 1]$).

3.4.2 Evaluation of the integral through Euler-MacLaurin formula

In absence of singularity

In practice, the integral (3.11) is evaluated from sampled data. For smooth integrands, sampling provides accurate solutions, provided that the sampling is thin enough. The error is evaluated using the Euler-MacLaurin formula (3.13). According to [36, 37], if $f_\mu^{n-1} \in C^0[0; 1]$ and f_μ^n is integrable over $[0; 1]$, and in absence of singularity, the integral giving the position writes

$$I_1 = \int_0^1 f_\mu(t) dt = Q_1 - M_1 + E_1 \quad (3.13)$$

where

$$\begin{aligned} Q_1 &= \frac{1}{m} \sum_{j=0}^{m-1} f_\mu \left(\frac{j + t_\nu}{m} \right) \\ M_1 &= \sum_{j=1}^n \frac{\bar{B}_j(t_\nu)}{j!} \frac{f_\mu^{(j-1)}(1) - f_\mu^{(j-1)}(0)}{m^j} \\ E_1 &= \frac{1}{m^n} \int_0^1 \frac{f_\mu^{(n)}(t) \bar{B}_n(t_\nu - mt)}{n!} dt \end{aligned}$$

where \bar{B}_i , $i \in \mathbb{N}$ are the periodic Bernoulli functions². The sum (3.13) gives an exact evaluation of I_1 in terms of the sum of samples of the integrand over the grid

²We take the same notations as in [1, 36]. For all $i \in \mathbb{N}$, the Bernoulli polynomials of degree j are defined via a generating function as

$$\frac{te^{xt}}{e^t - 1} = \sum_{i=0}^{\infty} B_j(x) \frac{t^i}{i!}$$

for $|t| \leq 2\pi$. For any $i \in \mathbb{N}$, the corresponding periodic Bernoulli function is defined by

$$\bar{B}_i(x) = B_i(x), \text{ for } 0 \leq x < 1, \quad \bar{B}_i(x+1) = \bar{B}_i(x), \quad \forall x \in \mathbb{R}$$

It is a function of period 1 taking the same values as the corresponding Bernoulli polynomial over $[0, 1)$.

$\left[\frac{t_\nu}{m} \quad \frac{1+t_\nu}{m} \quad \dots \quad 1 + \frac{-1+t_\nu}{m} \right]$ ($m > 0$) and residuals. The parameter t_ν which defines the sampling grid is, without loss of generality, written as

$$t_\nu = \frac{\nu + 1}{2} \quad \text{with} \quad -1 \leq \nu \leq 1$$

The term Q_1 corresponds to the classical evaluation of the integral from the sampled signal. M_1 is a correcting term taking into account the values at the boundaries. E_1 is the residual error. We now investigate further the two errors terms M_1 and E_1 . When the function f_μ is smooth, one can choose an arbitrary integer $n_0 \leq n$ to evaluate the error terms. One obtains

$$M_1 = \sum_{j=1}^{n_0} \frac{\bar{B}(t_\nu)}{j!} \frac{f_\mu^{(j-1)}(1) - f_\mu^{(j-1)}(0)}{m^j} = \sum_{j=1}^{n_0} O\left(\frac{1}{m^j}\right) = O\left(\frac{1}{m}\right)$$

On the other hand, the residual error term writes,

$$|E_1| = \frac{1}{m^{n_0}} \left| \int_0^1 \frac{f_\mu^{(n_0)}(t) \bar{B}_{n_0}(t_\nu - mt)}{n!} dt \right| \leq \frac{1}{m^{n_0}} \int_0^1 \left| \frac{f_\mu^{(n_0)}(t)}{n_0!} \right| dt \max_{t \in [0;1]} (|\bar{B}_{n_0}(t_\nu - mt)|)$$

since \bar{B} is continuous and $f^{(n_0)}$ integrable. This gives

$$E_1 = O\left(\frac{1}{m^{n_0}}\right)$$

Gathering these estimates of M_1 and E_1 , we deduce that

$$I_1 = Q_1 + O\left(\frac{1}{m}\right)$$

The error made when evaluating the integral I_1 from the samples is of the same order as the sampling interval.

With a first order singularity

As we have shown in Section 3.4.1, the integrand f_μ has, in many cases of practical interest, a singularity of order 1. In the presence of a first order singularity in t_s , according to [36, 37] that both refer to [73], the Cauchy principal value integral can also be approximated³ in a similar way, while the standard integral $\int_0^1 f_\mu(t) dt$ is ill-defined. In this case, the following relation holds, [36, 37] giving an estimate of I_2 , the principal value of I_1

$$I_2 = \int_0^1 f_\mu(t) dt = Q_2 - S_2 - M_2 + E_2$$

³Consider h a continuous function over $[0; 1]$ and $s \in [0; 1]$. The following limit exists

$$I_c = \lim_{\epsilon \rightarrow 0} \int_0^{s-\epsilon} \frac{h(x)}{x-s} ds + \int_{s+\epsilon}^1 \frac{h(x)}{x-s} ds$$

It is the principal value. We note it

$$I_c = \int_0^1 \frac{h(x)}{x-s} ds$$

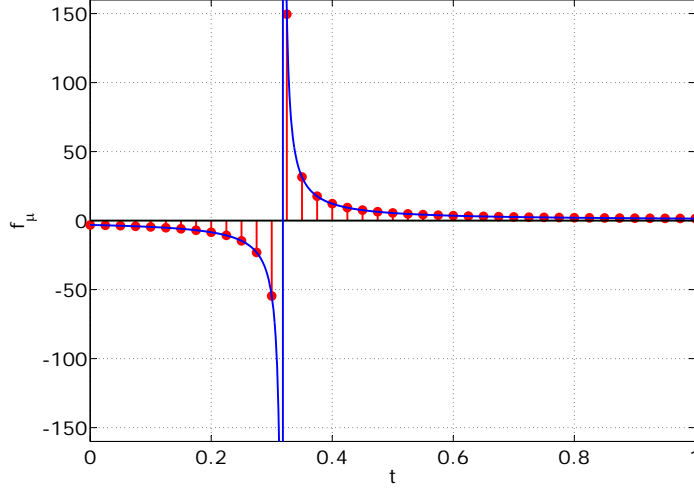


Figure 3.7: Sampling

where

$$\begin{aligned}
 Q_2 &= \frac{1}{m} \sum_{j=0}^{m-1} f_\mu \left(\frac{j + t_\nu}{m} \right) \\
 S_2 &= \frac{\pi}{\tan(\pi(t_\nu - mt))} f_\mu^*(t_s) \\
 M_2 &= \sum_{j=1}^n \frac{\bar{B}_j(t_\nu)}{j!} \frac{1}{m^j} (f_\mu^{j-1}(1) - f_\mu^{j-1}(0)) \\
 E_2 &= \frac{1}{m^n} \int_0^1 \frac{d^n}{dy^n} (f_\mu(y) - \pi f_\mu(t_s)(y - t_s) \cot(\pi(y - t_s))) \frac{\bar{B}_n(t_\nu - my)}{n!} dy
 \end{aligned}$$

where \bar{B}_i is again the periodic Bernoulli function of degree i . t_ν is a parameter accounting for the centering of the sampling grid $\left[\frac{t_\nu}{m}, \frac{1+t_\nu}{m}, \dots, 1 + \frac{-1+t_\nu}{m} \right]$ ($m > 0$). As in the case of a smooth integrand previously addressed, Q_2 corresponds to the classical computation of the integral from sampled measurements. S_2 is a term added to account for the singularity. M_2 accounts for the boundary values, and E_2 is the residual error. To evaluate the error terms M_2 and Q_2 , we proceed as earlier. Since f_μ^* is smooth, M_2 is evaluated using an arbitrary integer $n_0 \leq n$.

$$M_2 = \sum_{j=1}^{n_0} \frac{\bar{B}_j(t_\nu)}{j!} \frac{f_\mu^{(j-1)}(1) - f_\mu^{(j-1)}(0)}{m^j} = \sum_{j=1}^{n_0} O\left(\frac{1}{m^j}\right) = O\left(\frac{1}{m}\right) \quad (3.14)$$

Evaluating E_2 is a bit more involved. In details

$$E_2 = \frac{1}{m^n} \int_0^1 \frac{d^n}{dy^n} \left(\frac{f_\mu^*(y)}{y - t_s} - \pi f_\mu^*(t_s) \cot(\pi(y - t_s)) \right) \frac{\bar{B}_n(t_\nu - my)}{n!} dy = O\left(\frac{1}{m^n}\right) \quad (3.15)$$

Proof: According to [1, §4.3.70,p.75]

$$\cot(\pi(y - t_s)) = \frac{1}{\pi(y - t_s)} - \frac{1}{\pi} \sum_{j=1}^{\infty} \frac{(2\pi)^{2j} |B_{2j}|}{(2j)!} (y - t_s)^{2j-1}$$

which yields

$$E_2 = \frac{1}{m^n} \int_0^1 \frac{d^n}{dy^n} \left(\frac{f_\mu^*(y)}{y - t_s} - \frac{f_\mu^*(t_s)}{y - t_s} + \sum_{j=1}^{\infty} \frac{(2\pi)^{2j} |B_{2j}|}{(2j)!} (y - t_s)^{2j-1} \right) \frac{\bar{B}_n(t_\nu - my)}{n!} dy$$

Again according to [1, §23.1.15,p.805], the following inequality holds

$$\begin{aligned} |B_{2j}| &\leq \frac{2(2j)!}{(2\pi)^{2j}} \frac{1}{1 - 2^{1-2j}} \\ \frac{(2\pi)^{2j} |B_{2j}|}{(2j)!} &\leq \frac{2}{1 - 2^{1-2j}} \end{aligned}$$

The radius of convergence of the series $\sum_{j=1}^{\infty} \frac{(2\pi)^{2j} |B_{2j}|}{(2j)!} (y - t_s)^{2j-1}$ is equal or greater than 1. As $y - t_s$ takes value in $[0, 1]$, the function smooth. The only term left under the integral sign is a continuous function over $[0, 1]$. For any n , it can be bounded above by its maximum on the interval independently of m , which leads to Equation (3.15). ■

Equation (3.14) and Equation (3.15) show that the two error terms M_2 et E_2 vanish when the sampling interval gets null.

Finally, we wish to take a look at the term S_2 stemming from the singularity. In t_s ,

$$S_2(t_s) = \frac{\pi}{\tan(\pi(t_\nu - mt_s))} \frac{\Delta x \dot{f}\left(t_s + \frac{\mu\Delta x}{2}\right)}{\left(\frac{\partial D}{\partial t}\right)_{t=t_s} + o(1)}$$

However $t_s + \mu\Delta x/2$ is close to the extremum (which is in $t_0 = t_s + \epsilon\Delta x/2$). The numerator can thus be expanded near the singularity

$$\begin{aligned} \dot{f}\left(t_s + \frac{\mu\Delta x}{2}\right) &= 0 + \left[\left(t_s + \frac{\mu\Delta x}{2}\right) - \left(t_s + \frac{\epsilon\Delta x}{2}\right) \right] \ddot{f}\left(t_s + \frac{\epsilon\Delta x}{2}\right) + o(\Delta x) \\ &= (\mu - \epsilon) \frac{\Delta x}{2} \ddot{f}\left(t_s + \frac{\epsilon\Delta x}{2}\right) + o(\Delta x) \end{aligned}$$

And the expansion of the denominator around the singularity yields

$$\begin{aligned} \left(\frac{\partial D}{\partial t}\right)_{t=t_s} &= \dot{f}\left(t_s + \frac{\Delta x}{2}\right) - \dot{f}\left(t_s - \frac{\Delta x}{2}\right) \\ \dot{f}\left(t_s + \frac{\Delta x}{2}\right) &= 0 + (1 - \epsilon) \frac{\Delta x}{2} \ddot{f}\left(t_s + \frac{\epsilon\Delta x}{2}\right) + \frac{1}{2} \left((1 - \epsilon) \frac{\Delta x}{2}\right)^2 \dddot{f}\left(t_s + \frac{\epsilon\Delta x}{2}\right) + o(\Delta x^2) \\ \dot{f}\left(t_s - \frac{\Delta x}{2}\right) &= 0 - (1 + \epsilon) \frac{\Delta x}{2} \ddot{f}\left(t_s + \frac{\epsilon\Delta x}{2}\right) + \frac{1}{2} \left((-1 - \epsilon) \frac{\Delta x}{2}\right)^2 \dddot{f}\left(t_s + \frac{\epsilon\Delta x}{2}\right) + o(\Delta x^2) \\ \left(\frac{\partial D}{\partial t}\right)_{t=t_s} &= \Delta x \ddot{f}\left(t_s + \frac{\epsilon\Delta x}{2}\right) + o(\Delta x^2) \end{aligned}$$

Finally,

$$\begin{aligned} S_2(t_s) &= \frac{\pi \cdot \cot(\pi(t_\nu - mt_s))}{2} \frac{(\mu - \epsilon)\Delta x^2 \ddot{f}(t_s + \frac{\epsilon\Delta x}{2}) + o((\mu - \epsilon)\Delta x^2)}{\Delta x \ddot{f}(t_s + \frac{\epsilon\Delta x}{2}) + O(\Delta x^2)} \\ &= \frac{\pi \cdot \cot(\pi(t_\nu - mt_s))}{2} \cdot ((\mu - \epsilon)\Delta x + O(\Delta x^2)) \end{aligned}$$

The error term S_2 due to the singularity is thus the product of a term proportional to the spacing Δx between two sensors⁴ by a term which depends on the sampling grid. The term $\cot(\pi(t_\nu - mt_s))$ is indeed a comparison between the centering of the grid parametrized by t_ν and the singularity. It evaluates the distance between the singularity and the closest point of the sampling grid. The function is π -periodical. So evaluating $\cot(\pi(t_\nu - mt_s))$ is equivalent to evaluate all $\cot(\pi(j + t_\nu - mt_s))$ at once. Moreover $\cot(\pi(j + t_\nu - mt_s))$ gets infinitely large when t_s gets close to any point $\frac{j+t_\nu}{m}$ of the sampling grid. Interestingly, taking a thinner sampling grid has no reason to improve the result. However, if the sampling grid is perfectly centered around the singularity, i.e. $t_\nu - mt_s \in \mathbb{N}$, the error is in $O(\frac{1}{m})$ and thus tends toward 0 with the sampling interval.

Gathering the estimates of M_2 , E_2 and S_2 above, we obtain

$$I_2 = Q_2 + O\left(\frac{1}{m}\right) + O(\Delta x)$$

3.4.3 Importance of the Cauchy principal value integral

We consider further the case B.1 with a first-order singularity. It is assumed that the distance between the two sensors is such that there is at most one extremum of the magnetic field in any interval of length Δx . For sake of easiness, we consider that here there is only one extremum of f over $[-1; 1]$. We now verify on an example, that the Cauchy principal value corresponds indeed to the motion of the rigid body.

Consider the function

$$f(t) = t^4$$

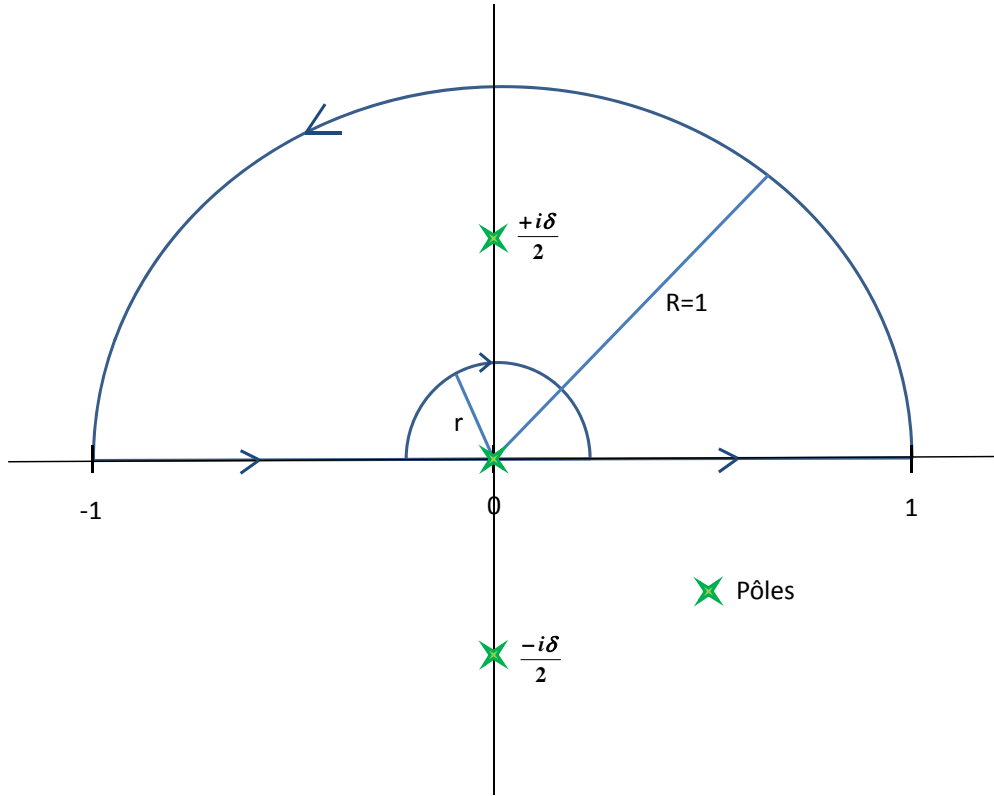
The reconstructed velocity is given by

$$f_\mu(t) = \Delta x \frac{4 \cdot \left(t + \frac{\mu\Delta x}{2}\right)^3}{\left(t + \frac{\Delta x}{2}\right)^4 - \left(t - \frac{\Delta x}{2}\right)^4} = \frac{\left(t + \frac{\mu\Delta x}{2}\right)^3}{t \left(t^2 + \frac{\Delta x^2}{4}\right)}$$

which has a single singularity on $[-1; 1]$. It is a first order singularity, we are thus, as desired, in the case B.1.

One can evaluate by two means the integral of f_μ over the path C represented in Figure 3.8, which consists of half the circle of radius $R = 1$ centered in $(0,0)$, C_1 , the two segments $[-1; -r]$

⁴To be more accurate, S_2 is proportional to the distance between the point where the temporal derivative is evaluated at the singularity and the point where the temporal derivative vanishes (see Figure 3.6). In particular, if the gradient could be evaluated at a single point by an ideal gradiometer, and not by a finite difference scheme, it would yield $(\mu - \epsilon)\Delta x = 0$. According to the list of the possible singularities provided above, one would thus switch from case B.1 (first order singularity) to a case A.1 without singularity, which concurs with the fact that the term S_2 due to the singularity vanishes.


 Figure 3.8: Poles of f_μ and integration path.

and $[r;1]$, and half a circle of radius r centered in $(0,0)$, C_r . The value of interest is when r gets to 0. One has

$$\oint_C f_\mu(z) dz = 2i\pi \text{Res} \left(f_\mu, i\frac{\Delta x}{2} \right) = \underbrace{\int_{C_1} f_\mu(z) dz}_{I_1} + \underbrace{\int_{-1}^1 f_\mu(z) dz}_{I_2} + \lim_{r \rightarrow 0} \left(\underbrace{\int_{C_r} f_\mu(z) dz}_{I_3} \right)$$

where one wishes to evaluate I_2 by computing every other terms.

Starting with I_3 , the integral can be re-parametrized in the angle θ .

$$I_3 = \lim_{r \rightarrow 0} \int_{+\pi}^0 f_\mu \left(r e^{i\theta} \right) r i e^{i\theta} d\theta$$

The limit and integral signs can be inverted, which yields

$$I_3 = \int_{+\pi}^0 \lim_{r \rightarrow 0} \left(\int_{+\pi}^0 \frac{\left(r e^{i\theta} + \frac{\mu \Delta x}{2} \right)^3 r i e^{i\theta} d\theta}{r e^{i\theta} \left(r^2 e^{2i\theta} + \frac{\Delta x^2}{4} \right)} \right) = -\frac{\mu^3 \Delta x i \pi}{2} \quad (3.16)$$

The same kind of re-parametrization can also be done for I_1 with $R = 1$. It gives

$$I_1 = \int_0^\pi f_\mu \left(e^{i\theta} \right) i e^{i\theta} d\theta = \int_0^\pi \left(e^{i\theta} + \frac{\mu \Delta x}{2} \right)^3 \cdot \frac{1}{1 + \frac{\Delta x^2 e^{-1i\theta}}{4}} \cdot e^{-2i\theta} i d\theta$$

By taking a Taylor expansion formula for small Δx , one finally obtains

$$I_1 = -2 + \frac{3\mu\Delta x i\pi}{2} + O(\Delta x^2) \quad (3.17)$$

The last term to evaluate is $Res(f_\mu, i\frac{\Delta x}{2})$. One has

$$\begin{aligned} \oint_C f_\mu(z) dz &= 2i\pi Res\left(f_\mu, i\frac{\Delta x}{2}\right) \\ &= 2i\pi \lim_{t \rightarrow i\frac{\Delta x}{2}} \left(\frac{\left(t + \frac{\mu\Delta x}{2}\right)^3}{t\left(t + i\frac{\Delta x}{2}\right)} \right) = \frac{\pi\Delta x}{2} (3\mu^2 - 1) - i\frac{\mu\Delta x}{2} \mu (\mu^2 - 3) \end{aligned} \quad (3.18)$$

Finally, putting all terms (3.16), (3.17) and (3.18) together yields

$$\begin{aligned} \int_{-1}^1 f_\mu(z) dz &= \oint_C f_\mu(z) dz - I_1 - I_3 = 2 + \frac{(3\mu^2 - 1)\pi}{2} \cdot \Delta x + O(\Delta x^2) \\ &= \int_{-1}^1 (v(t) = 1) dt + O(\Delta x) \end{aligned}$$

The real trajectory is thus reconstructed with an error of order Δx . The Euler-MacLaurin discretization scheme bypasses the singularity and provides an estimate of the traveled distance up to order 1 in Δx .

Conclusion

The position of a rigid body moving along a single axis can be evaluated thanks to the variations of the magnetic field by computing the integral (3.10) reproduced below

$$x(1) - x(0) = \int_0^1 \frac{\dot{B}(x(t))}{\nabla B(x(t))} dt \quad (3.10)$$

Estimating the gradient of the magnetic field can be achieved by a simple finite difference scheme with two magnetometers such that

$$\int_0^T f_\mu(t) dt = \Delta x \int_0^T \frac{\dot{f}(t + \mu\Delta x/2)}{f(t + \Delta x/2) - f(t - \Delta x/2)} dt \quad (3.11)$$

When the magnetic field presents an extremum, this can lead to integrate a function presenting a singularity.

As explained in Section 3.4.1, if the sampling grid is thin enough with respect to the variations of the field, there is at most one extremum between the two sensors used to estimate the gradient. Either the estimation of the gradient and the time-derivative vanish at the same point (case *A.1*), in which case there is no singularity, or, and it is the mostly encountered case, the gradient and the time-derivative vanish in separate points. In that case, the function f_μ to be integrated presents a first order singularity near the point where the gradient vanishes. Then, as has been illustrated by the treated example in Section 3.4.3, the position integrated from the samples is of the form

$$\text{Computed position} = \text{true position} + O\left(\frac{1}{m}\right) + O(\Delta x)$$

When the sampling time goes to zero (or when the speed goes to zero, i.e. one performs a quasi-static move), there is still an error of order Δx . In practice, the distance between the sensors is constrained by the size of the sensors, their mutual influence upon each other, and their resolution with respect to the magnitude of the gradient to measure. A trade-off with Equation (3.9), and Equation (3.2) has to be considered.

3.5 One Practical Implementation: the magneto-inertial pedometer

The principles of magneto-inertial navigation have been presented in Chapter 2. Several important points in the design of a measurement system suitable for implementation of a MINAV navigation system have been analyzed earlier in this chapter. The system requires a 3-axis accelerometer and a 3-axis gyrometer to perform the attitude estimation. A set of spatially distributed magnetometers and a 3-axis gyrometer are necessary to estimate the velocity in the body frame. The Jacobian matrix of the magnetic field is estimated from the set of magnetometers. Section 3.2 and Section 3.4 gives insights into choosing the distance between the sensors of the set. The measurement system now presented complies with all these recommendations formulated in this chapter:

1. the sensors data have to be time-stamped,
2. the distance between the sensors has to satisfy the “rule of the thumb”: *at all times, at most one extremum of the magnetic field can be located in between the sensors*,
3. the inter-sensor distance has to be known accurately,
4. the sample rate, the sensor resolution and the noise level have to be chosen according to the (conservative) error estimate (3.9).

The MINAV system under consideration (it is detailed further and tested in Chapter 5) is pictured in Figure 3.9. It incorporates spatially distributed magnetometers and an IMU.

Six HMR2300 three-axis magneto-resistive magnetometers from HoneywellTM are used. Their range is ± 2 G and they have a $70 \mu\text{G}$ resolution. The distances between the sensors are approx. 10 cm one from each other. As discussed in Section 3.2, these positions have been carefully identified to 9.5 cm and 10.5 cm respectively. This distance is compliant with the “rule of thumb” formulated in Section 3.4 for typical indoor environments.

Alternately, these magnetometers could be replaced by Philipps KMZ10B magneto-resistive sensors, or fluxgate sensors like the FLC3-70 from Stefen Mayer Instrument.

The IMU under consideration is a 3DM-GX1 from MicrostrainTM. It includes three angular-rate gyroscopes, three orthogonal single-axis magnetometers, and three single-axis accelerometers, along with 16 bit A/D converters and a microcontroller. In the setup, the IMU is asked to deliver temperature-compensated sensor data at a rate of 76 Hz, its fastest output rate.

Alternately, this IMU could be replaced by other models such as the Adis16405 from Analog Devices which is less costly (approx. half prize ≈ 600 USD). This last device provides only raw data (and not reconciliated measurements), and it belongs to the same class of sensors in terms of short term bias stability of the gyroscopes (which is a critical factor for attitude estimation). Performance of the built-in accelerometers are also alike.

As is detailed in Chapter 5, the sensors communicate through a datation module implementing the time-stamping technique of Section 3.1. It relies on a micro-controller MPC555 from Motorola, which serves as an interface for the sensors.

Conservative estimate of error of the considered MINAV system

The precision achievable with this system can be evaluated according to Equation (3.9). During the motion, it is assumed that $J_B \approx 5.10^{-2}G.m^{-1}$, $V \approx 1 m.s^{-1}$. This gives $\dot{B} \approx 5.10^{-2}G.s^{-1}$. A signal of this form can be generated by integrating twice $\ddot{B} = c$, where c is a white noise with spectral density $\frac{\lambda_c}{2\pi}$ (or noise power $\frac{\lambda_c}{2}$) with $\lambda_c \approx 5.10^{-6}G.s^{-3}$. The magnetic sensor under consideration has a variance $\lambda_v \approx 2.10^{-9}G^2$ and operates at a frame rate $f = 76 Hz$.

$$E^2 = \frac{5.10^{-6}}{4 \cdot \sqrt{3} \cdot 76} + 6 \cdot (\sqrt{3} - 1) 2.10^{-9} \cdot 76^2 \approx 10^{-8} + 5.10^{-5}$$

The minimal estimation error variance is thus driven by the noise of the sensor (and not by the lag due to tracking the underlying dynamics governing the sensed variable).

As a result, the error introduced under the form $\frac{\Delta \dot{B}}{J_B}$ is approximately $0.14 m.s^{-1}$. The second error term, $\frac{\Delta J_B V}{J_B}$, accounting for the spatial differentiation and the sensors resolution, is approximately $0.04 m.s^{-1}$. Using Equation (3.9), the total error is $0.18 m.s^{-1}$. This is a conservative estimate which allows to assess that the set-up is relevant for the pedestrian positioning application.

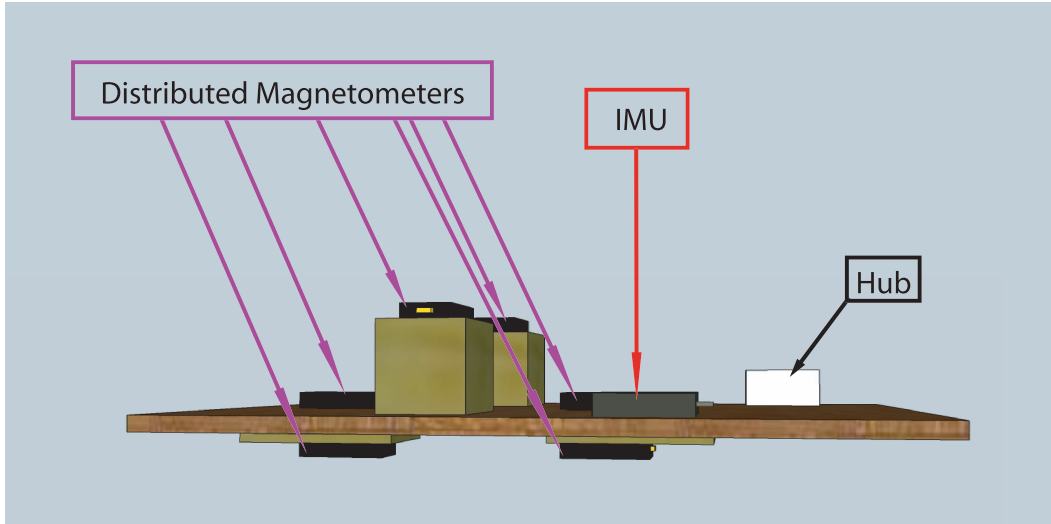


Figure 3.9: Schematic representation of the sensor module.

Chapter 4

Alignment and calibration of MINAV sensors: problems and methods

Alignement et calibration des capteurs MINAV: problèmes et méthodes

Jusqu'à présent, les capteurs ont été considérés comme des tri-axes idéaux, alignés avec le repère de référence \mathcal{R}_b . En pratique, et particulièrement avec des capteurs bas-coûts, les capteurs ne sont pas aussi parfaits. Ce chapitre propose une modélisation de ces erreurs, en Section 4.1, et des méthodes pratiques pour calibrer les capteurs, i.e. estimer les paramètres dans le modèle d'erreur. Les erreurs prises en compte sont essentiellement celles qui sont dues aux non-orthogonalités, aux erreurs d'alignement, aux facteurs d'échelle et aux biais constants. Les problèmes dus aux dérives à long terme, à la compensation en température, à la sensibilité aux radiations ou aux défauts de la conversion analogique numérique ne rentrent pas dans le cadre de ce travail. La calibration d'un capteur seul, magnétomètre ou accéléromètre, est détaillée en Section 4.2, puis une méthode pour calibrer un gyroscope au moyen d'un accéléromètre préalablement calibré est exposée en Section 4.3. La Section 4.4 traite de la calibration et de l'alignement d'un jeu de magnétomètres répartis dans l'espace. Enfin, l'harmonisation (i.e. l'alignement) des blocs inertiel et magnétique est étudiée en Section 4.5, avant de proposer une procédure opérationnelle de calibration du système complet en Section 4.6, qui reprend les différents éléments présentés dans ce chapitre.

The principles of MINAV and rules for design of its applications have been exposed in Chapter 2 and Chapter 3, respectively. We now get in more details into hardware related issues. So far, the sensors have been seen as perfect orthonormal triaxis, aligned with the body reference frame \mathcal{R}_b . In practice, sensors (especially low-cost sensors) do not appear under this idealized form. The sources of errors and their role in the constituted navigation system are discussed in this chapter. We propose a set of solutions to, sequentially, calibrate them. The problem treated are essentially related to non-orthogonalities, misalignments, scale factors, and constant biases. The problem of long term drift, temperature compensation [35],

sensitivity to radiations, defects of analog to digital conversion are out of the scope of this work.

4.1 Errors model for the 3-axis sensors under consideration

Consider a 3-axis sensor. Its sampled measurements are denoted y_i (3×1 vector), where i stands for the sampling index, whereas the actual value of the sensed field is denoted Y_i (3×1 vector). These measurements are collected in $y = (y_i)_{i=1,\dots,N}$, where N is the total number of samples.

To improve the accuracy of raw sensor data y , especially when dealing with low-cost sensors, mathematical models must be built to take into account the various sources of errors [95]. Some, such as scale-factors, misalignment and the resulting cross-coupling of axes, apply to all kinds of sensors (and in particular to gyroscopes, accelerometers and magnetometers which are used in the presented MINAV system) while some others only apply to a particular class of sensors.

In the case of magnetometers which is of particular interest here, there exist additional specific sources of errors, mainly hard and soft iron errors (see [48, 94]). Hard iron errors are induced by permanent undesired fields. They are generated by ferromagnetic materials attached to the magnetometer frame (typically the structure or the equipment installed near the magnetometer, or even non-varying current in close-by wires). They result in a bias. Soft iron errors are induced by materials that generate magnetic fields in response to externally applied magnetic fields. The model presented in this chapter takes only into account the proportionality of this error to the applied external field. The constant of proportionality is referred to as the magnetic susceptibility of the material considered. Soft iron errors generally present a hysteresis which is often small enough to be neglected.

To cover most cases of interest, we consider a bias vector $\beta = [\beta_1 \ \beta_2 \ \beta_3]^T$, scale-factors represented by a diagonal matrix α , and misalignments terms represented by a skew-symmetric matrix R , e.g. under the micro-rotation form as used in the CORDIC navigation algorithm.

$$Y_i = \alpha R y_i + \beta$$

$$\text{with } R = \begin{bmatrix} 1 & \psi & -\theta \\ -\psi & 1 & \phi \\ \theta & -\phi & 1 \end{bmatrix}, \quad \alpha = \begin{bmatrix} \alpha_1 & & \\ & \alpha_2 & \\ & & \alpha_3 \end{bmatrix}$$

However, due to the use of low cost sensors, substantial misalignments and errors must be considered, and, additionally, significant non-orthogonality between axes may arise. Therefore, no possibly simplifying assumption on the magnitude of the errors is made. All these factors are gathered into a general matrix A , and a bias vector B . With these notations, the error model is

$$Y_i = A y_i + B \tag{4.1}$$

The calibration problem consists in determining A and B . This is generally addressed using an external reference, e.g. a calibration table. We wish to avoid this cumbersome equipment, and propose a different approach. By keeping the sensors at the same place, but along various orientations, at steady state, the magnetic and gravitational fields are constant

and should produce a measurement vector of constant norm. This constant may be chosen equal to 1 (for magnetometers) without any loss of generality¹. The calibration technique that we propose all exploit this property.

4.2 Individual 3-axis sensor calibration

4.2.1 Background on table-free calibration methods

In classic inertial navigation, there exist various methods for three-axis sensors calibration. Most of them have an important drawback in common. They require expansive tools to acquire the data and compare them against a fixed reference, and, quite often, a high degree of expertise to process the data. Usually (see e.g. [25]), IMUs calibration is achieved using a well-instrumented mechanical platform (called *calibration table*) whose varying orientation is precisely measured. The platform is rotated to various precisely controlled orientations which serve as comparisons against the orientations determined from the IMU sensors. The rotational velocities are accurately controlled as well. Magnetometers calibration is usually performed using a similar approach in magnetically shielded facilities to provide a known uniform field (see e.g. [94]). Similarly, measurements are then performed with precise knowledge of sensors orientation.

The recent development of micro-electro mechanical systems (MEMS) and other low-cost sensors has led to a paradox. Due to their relatively low quality, these low-cost sensors are in great need of a calibration procedure (much more than higher-end sensors), but the cost of the traditional calibration procedures may exceed by several orders of magnitude the cost of developing and constructing the sensors themselves. Moreover, as the cost of the sensors are decreasing, their use is spreading. This yields a great interest in developing new “simple but effective” calibration procedures that do not require any high degree of expertise nor any expensive hardware to be put into practice. Lately, a new paradigm for such sensors calibration has emerged. Some procedures and algorithm have been proposed (see [13, 44, 100]) and a few for magnetometers calibration (see [45, 48, 92, 108]). They all rely on the fact that the force field under consideration (the gravitational field for accelerometers and the Earth magnetic field for magnetometers) corresponds to a sensed vector having, in theory, a constant and known norm. The strategy is to identify and remove the measurement errors. No specific calibration hardware is required.

The measurement errors are represented by the constant coefficients of the vector affine transformation (4.1). The calibration problem is recast into the determination of an inverse affine transformations maximizing a performance index. This index involves the norm of the reconstructed data and a comparison against its theoretical (scalar) constant value.

This method requiring a constant force field cannot be applied to the gyrometer calibration. Without using any expensive calibration table, the only constant rotation rate is the rotation of the Earth, which is below the precision of the class of sensors under consideration. Another method is thus proposed. It simultaneously calibrates the gyrometer

¹The norm of the gravity field can be obtained from dependable look-up tables [9]. Outdoor, the norm of the Earth magnetic field can also be found in tables [42]. But as for the norm of the magnetic field in buildings, there is no such table. However, the norm of the magnetic field does not play any roll in a magneto-inertial system: the entire dynamics of the magnetic field as in Equation (2.5) is proportional to that norm. One can thus get rid off it and take the norm equal to one without impacting the system.

and performs the alignment with an already calibrated magnetometer or accelerometer by using the dynamics of the field seen from the sensors (rotations).

4.2.2 Classical two-step algorithm for magnetometers and accelerometers calibration

Here, we briefly recall the two-step calibration algorithm originally proposed in [45, 48]. As the norm of the sensed field is assumed to be constant, $\|Y_i\|^2 = 1$, for all $i = 1, \dots, N$, the sensed field vectors y_i should all be located on the unit sphere. Due to errors, this is not the case, as already discussed. It is desired to find A and B in Equation (4.1) such that the values $Ay_i + B$ are as close as possible to this sphere. Equivalently, one can seek for a matrix M and a bias vector N such that the values $M(y_i - N)$ are as close as possible to the same sphere. In details, P and Q have to yield a fair approximation of $\|P(y_i - Q)\|^2 = 1$ for every sample $i = 1, \dots, N$. To this end, P and Q are defined as the minimizers of the following cost function (4.2)

$$g(P, Q, y) = \sum_{i=1}^N \left(\|P(y_i - Q)\|^2 - 1 \right)^2 \quad (4.2)$$

Once expanded, it becomes

$$g(P, Q, y) = \sum_{i=1}^N \left(y_i^T P^T P y_i - 2Q^T P^T P y_i + (Q^T P^T P Q - 1) \right)^2$$

Here, P is sought after under the form of an upper triangular matrix, implicitly leaving out any rotation matrix which leaves the cost g invariant. The parameters to be determined through the minimization procedure are the components of P and Q , i.e. 9 parameters. The cost function (4.2) is quartic in these parameters. Yet, as proposed in [45, 48], a two-step estimation using a least squares method can be performed. Note

$$P = \begin{pmatrix} p_{11} & p_{12} & p_{13} \\ 0 & p_{22} & p_{23} \\ 0 & 0 & p_{33} \end{pmatrix}, \quad Q = \begin{pmatrix} q_1 \\ q_2 \\ q_3 \end{pmatrix}$$

First, the following change of variables is performed

$$\begin{cases} a = p_{11}^2 & d = 2p_{11}p_{12} & g = -2(aq_1 + dq_2 + fq_3) \\ b = p_{12}^2 + p_{22}^2 & e = 2p_{12}p_{13} + 2p_{22}p_{23} & h = -2(dq_1 + bq_2 + eq_3) \\ c = p_{13}^2 + p_{23}^2 + p_{33}^2 & f = 2p_{11}p_{13} & i = -2(fq_1 + eq_2 + cq_3) \\ & j = aq_1^2 + bq_2^2 + cq_3^2 + 2dq_1q_2 + 2eq_2q_3 + 2fq_1q_3 - 1 \end{cases}$$

These last 10 variables are normalized to 9 variables by considering the 9-dimensional vector of ratios $r = (a/b, c/b, d/b, e/b, f/b, g/b, h/b, i/b, j/b)$. Then, a new optimization

problem (4.3) is formulated.

$$\min_r \sum_{i=1}^N \left\| \frac{y_{i1}^2}{y_{i2}^2} \cdot \frac{a}{b} + \frac{y_{i3}^2}{y_{i2}^2} \cdot \frac{c}{b} + \frac{y_{i1} \cdot y_{i2}}{y_{i2}^2} \cdot \frac{d}{b} + \frac{y_{i2} \cdot y_{i3}}{y_{i2}^2} \cdot \frac{e}{b} + \frac{y_{i3} \cdot y_{i1}}{y_{i2}^2} \cdot \frac{f}{b} + \frac{y_{i1}}{y_{i2}^2} \cdot \frac{g}{b} + \frac{y_{i2}}{y_{i2}^2} \cdot \frac{h}{b} + \frac{y_{i3}}{y_{i2}^2} \cdot \frac{i}{b} + \frac{1}{y_{i2}^2} \cdot \frac{j}{b} - 1 \right\|^2 \quad (4.3)$$

This new (quadratic) problem is solved by a least-squares method. Finally, inverse algebraic transformations permit to recover the 9 coefficients of A and B from the 9 ratios. The optimization problem (4.3) is not equivalent to the minimization of the original cost function g in (4.2). The reason why is that, as appeared when introducing the vector or ratios r , the (not unique) normalization of the variables yielding the reduction to a classic least-squares problem, has introduced a non uniform weighting of the various measurements (see (4.3)). In theory, it would have been possible to consider any of the 9 variables a, b, \dots, j to normalize the problem. Similarly, this would have led to nonequivalent optimization problems though. The original optimization problem with cost function (4.2) has thus been “distorted”. In some extreme cases this can be a problem.

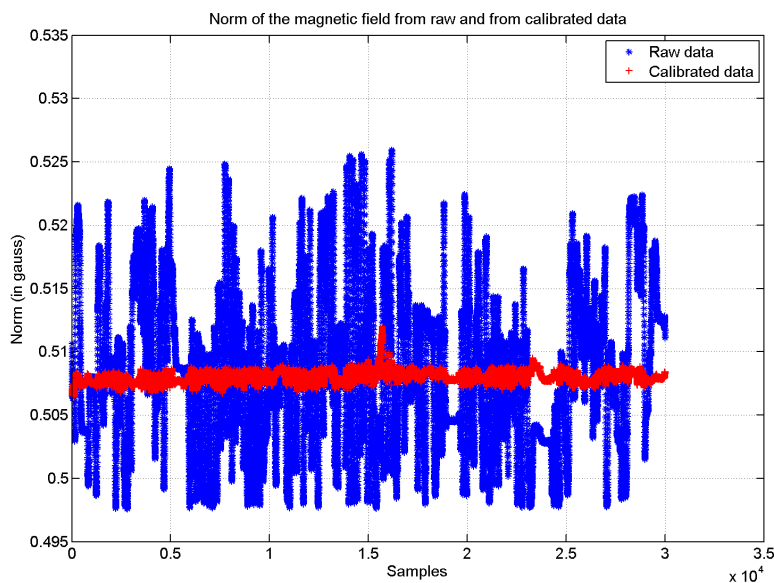


Figure 4.1: Comparison of the norm of raw and calibrated data.

Figure 4.1 presents results obtained with this algorithm. The statistics of both raw and calibrated data sets of a magnetometer HMR2300 and of the magnetometer of the IMU are presented reported in Table 4.1 along with the time elapsed during the computation of the algorithm on a Intel Core 2 Duo 2.6GHz.

IMU Magnetometer	Raw data	Calibrated data
Mean	$5.099327e - 1$	$5.139927e - 1$
Deviation	$1.077045e - 2$	$1.223969e - 3$
Samples	120000	120000
Time	-	<i>approx.1.2 s</i>
HMR2300	Raw data	Calibrated data
Mean	$5.090592e - 1$	$5.139977e - 1$
Deviation	$9.846039e - 3$	$6.878812e - 4$
Samples	120000	120000
Time	-	<i>approx.1.2 s</i>

Table 4.1: Raw data and calibrated data (through the 2-step algorithm) for two magnetometers.

4.2.3 An iterative algorithm for magnetometers and accelerometers calibration

We now develop an alternative technique. Consider a step in the iterations, say the k^{th} . Following the idea of [45, 48] presented earlier, we wish to account for the fact that the sensed field is constant. Consider the N data $y_{i,k}$, $i = 1, \dots, N$, which are initialized at step $k = 0$ with the measurements y_i . First, we formulate the following cost to be minimized

$$h(A, B, k) = \sum_{i=1}^N \left\| (Ay_{i,k} + B) - \frac{y_{i,k}}{\|y_{i,k}\|} \right\|^2 \quad (4.4)$$

This function is quadratic with respect to the coefficients of A and B . In view of algorithmic minimization, this is an advantage over the cost presented in [45] which is quartic with respect to these same variables. We note the uniquely defined solution

$$(A_{k+1}, B_{k+1}) = \arg \min_{A, B} h(A, B, k)$$

which can be obtained by a classic least-squares approach. Then, we use these matrices to update the data as follows

$$y_{i,k+1} = A_{k+1}y_{i,k} + B_{k+1}$$

After k such iterations, a matrix \tilde{A}_k and a vector \tilde{B}_k are obtained recursively by

$$\begin{cases} \tilde{A}_k = A_k \tilde{A}_{k-1} \\ \tilde{B}_k = A_k \tilde{B}_{k-1} + B_k \end{cases}$$

They relate $y_{i,k}$ to the raw measurements y_i . In details,

$$y_{i,k} = \tilde{A}_k y_i + \tilde{B}_k$$

We can now summarize the method

Algorithm 1 (Proposed algorithm):

1. Initialize $k = 0$, $y_{i,0} = y_i$ for all $i = 1, \dots, N$
2. Compute $(A_{k+1}, B_{k+1}) = \arg \min_{A,B} h(A, B, k)$ by a least-squares method (where h is given in Equation (4.4))
3. Update the data $y_{i,k+1} = A_{k+1}y_{i,k} + B_{k+1}$
4. Increase k by 1 and return to step 2

A limited number K of iterations is usually considered. Then the data $y_{i,K}$, $i = 1, \dots, N$ are the "calibrated data". □

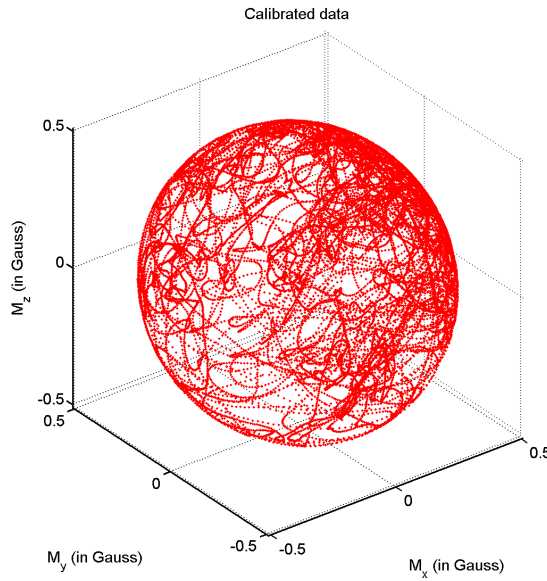


Figure 4.2: Calibrated data matching the sphere.

In words, this algorithm solves a sequence of least square problems in which the input data are iteratively calibrated using the successively determined calibration matrices and vectors. Figure 4.2 shows calibrated results in 3-dimension, obtained with the presented algorithm. We now prove two properties of the proposed algorithm 1. For sake of conciseness, we note $y_k = (y_{i,k})_{i=1,\dots,N}$.

Proposition 4 (calibration improvement): The data generated by the Algorithm 1 satisfy the following decrease property:

$$f(y_{k+1}) \leq f(y_k)$$

where

$$f(y_k) = \sum_{i=1}^N (1 - \|y_{i,k}\|)^2$$

Further, $(f(y_k))_{k \in \mathbb{N}}$ decreases and is positive, so it converges to a limit $\ell \geq 0$. □

This property shows that, in the sense detailed by the function f , the data are better and better calibrated as the iterations are pursued.

Proof: By construction, A_k and B_k are such that $h(A_k, B_k, k)$ is minimal. In particular, one can compare them against the identity matrix and the zero vector

$$h(A_{k+1}, B_{k+1}, k) \leq h(I_3, 0, k)$$

Replacing $A_{k+1}y_{i,k} + B_{k+1}$ by $y_{i,k+1}$ yields

$$\sum_{i=1}^N \left\| y_{i,k} - \frac{y_{i,k}}{\|y_{i,k}\|} \right\|^2 \geq \sum_{i=1}^N \left\| y_{i,k+1} - \frac{y_{i,k}}{\|y_{i,k}\|} \right\|^2 \quad (4.5)$$

or

$$\sum_{i=1}^N \left(y_{i,k} \cdot \left(1 - \frac{1}{\|y_{i,k}\|} \right) \right)^2 \geq \sum_{i=1}^N \left\| y_{i,k+1} - \frac{y_{i,k}}{\|y_{i,k}\|} \right\|^2$$

which gives, by triangle inequality on the right term,

$$\sum_{i=1}^N (1 - \|y_{i,k}\|)^2 \geq \sum_{i=1}^N \left(\|y_{i,k+1}\| - \left\| \frac{y_{i,k}}{\|y_{i,k}\|} \right\| \right)^2 \quad (4.6)$$

Finally,

$$f(y_k) \geq f(y_{k+1})$$

which concludes the proof. ■

Proposition 5 (alignment): The data generated by Algorithm 1 satisfy the following alignment property

$$\lim_{k \rightarrow +\infty} \left(\frac{y_{i,k+1}}{\|y_{i,k+1}\|} - \frac{y_{i,k}}{\|y_{i,k}\|} \right) = 0$$

□

This property shows that, as the iterations are pursued, the calibrated data make little progress in orientation.

Proof: First, we perform a preliminary decomposition of the objective function h

$$\begin{aligned} h(k) &\triangleq h(A_{k+1}, B_{k+1}, k) \\ &= \sum_{i=1}^N \left(\|y_{i,k+1}\|^2 + 1 - 2 \frac{\langle y_{i,k+1} | y_{i,k} \rangle}{\|y_{i,k}\|} \right) \end{aligned}$$

which can also be written under the form

$$\begin{aligned} h(k) &= f(y_{k+1}) + \sum_{i=1}^N \left(2 \|y_{i,k+1}\| - 2 \frac{\langle y_{i,k+1} | y_{i,k} \rangle}{\|y_{i,k}\|} \right) \\ &= f(y_{k+1}) + 2 \sum_{i=1}^N \|y_{i,k+1}\| \left(1 - \left\langle \frac{y_{i,k+1}}{\|y_{i,k+1}\|} \middle| \frac{y_{i,k}}{\|y_{i,k}\|} \right\rangle \right) \end{aligned} \quad (4.7)$$

Consider again Equation (4.5) and Equation (4.6), one obtains

$$f(y_k) \geq h(k) \geq f(y_{k+1})$$

From Proposition 4, we know that $f(y_k)$ converges to a limit ℓ as $k \rightarrow +\infty$. Therefore, from the preceding inequalities, we conclude that $h(k)$ converges to the same limit. Then, from Equation (4.7), we deduce

$$\lim_{k \rightarrow +\infty} \left(\sum_{i=1}^N \|y_{i,k+1}\| \left(1 - \left\langle \frac{y_{i,k+1}}{\|y_{i,k+1}\|} \middle| \frac{y_{i,k}}{\|y_{i,k}\|} \right\rangle \right) \right) = 0$$

All the terms under the \sum sign are positive or zero, therefore we conclude that, $\forall i = 1, \dots, N$,

$$\begin{aligned} \lim_{k \rightarrow +\infty} \left(\|y_{i,k+1}\| \left(1 - \left\langle \frac{y_{i,k+1}}{\|y_{i,k+1}\|} \middle| \frac{y_{i,k}}{\|y_{i,k}\|} \right\rangle \right) \right) &= 0 \\ \lim_{k \rightarrow +\infty} \left(\|y_{i,k+1}\| \left\langle \frac{y_{i,k+1}}{\|y_{i,k+1}\|} \middle| \left(\frac{y_{i,k+1}}{\|y_{i,k+1}\|} - \frac{y_{i,k}}{\|y_{i,k}\|} \right) \right\rangle \right) &= 0 \end{aligned} \quad (4.8)$$

Now, to conclude, note

$$u_{i,k} = \frac{y_{i,k+1}}{\|y_{i,k+1}\|} - \frac{y_{i,k}}{\|y_{i,k}\|}$$

and decompose it under the form

$$u_{i,k} = (1 - \alpha_{i,k}) \frac{y_{i,k+1}}{\|y_{i,k+1}\|} - \beta_{i,k} \frac{y_{i,k+1}^\perp}{\|y_{i,k+1}^\perp\|}$$

where $y_{i,k+1}^\perp$ is directly orthogonal to $y_{i,k+1}$, and with

$$\alpha_{i,k}^2 + \beta_{i,k}^2 = 1$$

We deduce from Equation (4.8) that

$$\lim_{k \rightarrow +\infty} \alpha_{i,k} = 1, \quad \lim_{k \rightarrow +\infty} \beta_{i,k} = 0$$

Finally, this gives

$$\lim_{k \rightarrow +\infty} \left(u_{i,k} = \frac{y_{i,k+1}}{\|y_{i,k+1}\|} - \frac{y_{i,k}}{\|y_{i,k}\|} \right) = 0$$

which concludes the proof. ■

The interested reader can refer to Appendix A for further conclusions on the asymptotic behavior of the iterative calibration procedure in a particular plane case.

4.3 Calibration of a 3-axis gyrometer with respect to an accelerometer

Classically (see [26, 54], and the references therein), the attitude of a rigid body (described by a rotation matrix for instance) can be estimated using a (3-axis) accelerometer and a (3-axis) gyrometer. This point is of particular importance in aerial robotics (see [55]). The reader can

report to Appendix F for a discussion on these methods. As detailed in Section 2.2, in MINAV systems, the attitude is used to project the velocity from the body frame onto the inertial frame of reference. Integration of the inertial frame velocity provides the trajectory. Since small angular errors in the attitude estimation give linearly growing errors in the trajectory, the attitude estimation is also a key task of our system. Calibration and harmonization of the accelerometers and gyrometers is then of paramount importance.

The accelerometer, which measures (at rest) the Earth gravity field (which is by assumption of constant norm in a neighborhood of the rigid body), can be calibrated using the exact same technique as the one presented for magnetometers. Because gravity is a constant field at the spatial scale of a laboratory, the calibration method consisting in orienting the sensing device in all possible directions is very easy to apply. Bias and scale factors are then identified and removed. However, this method is not suitable for gyrometer calibration. The culprit is that having some precisely controlled rotation rate is very difficult during in-the-field experiments. This results in a sensed field that does not have a constant norm, which totally discards the previously presented methods.

The method proposed below uses the relation between the accelerometer measurements and the rate of turn, as given by the chain rule differentiation. Compared to other methods (as e.g. [44]), the dynamic is not integrated, and the equation are kept under their differential expressions. The result of this calibration procedure is that the gyrometer is calibrated and harmonized with the accelerometer.

Let us define the calibration problem we wish to address.

Problem Statement

Consider a rigid body equipped with a (3-axis) gyrometer and a (3-axis) accelerometer. The accelerometer is calibrated (in the sense of Section 4.2), i.e. the matrices A and b in Equation (4.1) have already been identified, but the gyrometer is not. It is desired to calibrate the gyrometer in the frame of the accelerometer. Let Ω be the vector rotation rates, Ω_{acc} the components of Ω in the accelerometer frame, Ω_{gyr} the readings of the gyroscope, R_{acc} the rotation matrix from the inertial frame of reference \mathcal{R}_i to the accelerometer frame of reference \mathcal{R}_{acc} . After this calibration, one should be able to read the variable

$$\Omega_{acc} = R_{acc}\Omega$$

In other words, considering that, by default, one has

$$\Omega_{acc} = A_0\Omega_{gyr} + B_0$$

it is desired to identify A_0 and B_0 .

Proposition 6: Assuming that a properly calibrated accelerometer is available which delivers the measurements γ_{acc} and $\frac{d\gamma_{acc}}{dt}$ in its own frame \mathcal{R}_{acc} . The readings satisfy $\gamma_{acc} = R_{acc}g$ where R_{acc} is the rotation from \mathcal{R}_i to \mathcal{R}_{acc} , g is the gravity (this is only true if the accelerometer is rotated with zero velocity, i.e. it is always on the rotation axis).

Then, the following properties hold:

- the readings from the accelerometer and from the gyrometer are related through the relation

$$\frac{d\gamma_{acc}}{dt} = -\Omega_{acc} \times \gamma_{acc} \quad (4.9)$$

where $\Omega_{acc} = R_{acc}\Omega$

- the calibration matrix A_0 and bias B_0 such that

$$\Omega_{acc} = A_0 \Omega_{gyr} + B_0 \quad (4.10)$$

can be estimated from the knowledge of Ω_{gyr} , γ_{acc} and $\frac{d\gamma_{acc}}{dt}$.

□

This proposition states that the gyroscopes can be calibrated in the accelerometer frame with a procedure which, in fact, does not require any expensive equipment and can be performed in-the-field by any operator. As will appear, the platform has simply to be rotated in every direction around the accelerometer.

Proof: By making a cross product by γ_{acc} on the right side of Equation (4.9), and expanding the right-hand triple product according to the triple product expansion formula (a.k.a. Lagrange formula), one obtains

$$\frac{d\gamma_{acc}}{dt} \times \gamma_{acc} = \|\gamma_{acc}\|^2 \Omega_{acc} - (\Omega_{acc}^T \gamma_{acc}) \gamma_{acc} \quad (4.11)$$

Ω_{acc} can be split into the sum of Ω_{acc}^{\parallel} parallel to γ_{acc} , and Ω_{acc}^{\perp} orthogonal to γ_{acc} . Then, Equation (4.11) yields

$$\frac{d\gamma_{acc}}{dt} \times \gamma_{acc} = \|\gamma_{acc}\|^2 \Omega_{acc}^{\perp} = g^2 \Omega_{acc}^{\perp} \quad (4.12)$$

where g is the norm of the gravity.

This means that, for a given sample, Ω_{acc}^{\perp} can be determined from the knowledge of γ_{acc} and $\frac{d\gamma_{acc}}{dt}$. In other words, Ω_{acc}^{\perp} is observable from the measurement γ_{acc} . According to the error model of the sensor given in Equation (4.10), this projection can be expressed in terms of the sought after calibration parameters A_0 and B_0 as

$$\Omega_{acc}^{\perp} = P_{\gamma} (A_0 \Omega_{gyr} + B_0) \quad (4.13)$$

where P_{γ} is the projector on the plane orthogonal to γ_{acc} .

Gathering Equation (4.12) and Equation (4.13) yields Equation (4.14) for a given set of measurements, say the k^{th} .

$$\underbrace{\frac{\left(\frac{d\gamma_{acc}}{dt}\right)_k \times \gamma_{acc}}{\|(\gamma_{acc})_k\|^2}}_{\text{known with the accelerometer}} = \underbrace{(P_{\gamma})_k}_{\text{known with the accelerometer}} \left(\underbrace{A_0}_{\text{measured by the gyrometer}} \underbrace{(\Omega_{gyr})_k}_{\text{measured by the gyrometer}} + B_0 \right) \quad (4.14)$$

By introducing the vectors X_k depending only on the gyrometer measurement $(\Omega_{gyr})_k$ and Y_k depending only on the accelerometer measurements $(\gamma_{acc})_k$

$$X_k = \begin{pmatrix} (\Omega_{gyr})_k \\ 1 \end{pmatrix}$$

$$Y_k = \frac{\left(\frac{d\gamma_{acc}}{dt}\right)_k \times (\gamma_{acc})_k}{\|(\gamma_{acc})_k\|}$$

the equation can be simply rewritten under the linear form (in ${}_0A$ and B_0)

$$Y_k = (P_\gamma)_k [A_0 \ B_0] X_k$$

Gathering a set of data (indexed by index k), the parameters A_0 and B_0 can then be computed in a least square sense of the former equality. A_0 and B_0 are thus defined as the parameters minimizing the following cost function J

$$J(\tilde{A}, \tilde{B}) = \sum_{k=1}^K \left\| Y_k - (P_\gamma)_k [\tilde{A} \ \tilde{B}] X_k \right\|^2 \quad (4.15)$$

Algorithm 2: Denote $(E_i)_{i=1..12}$ a canonical base of $\mathbb{M}_{3,4}(\mathbb{R})$ with

$$E_1 = \begin{pmatrix} 1 & 0 & 0 & 0 \\ 0 & 0 & 0 & 0 \\ 0 & 0 & 0 & 0 \end{pmatrix}, \quad E_2 = \begin{pmatrix} 0 & 0 & 0 & 0 \\ 1 & 0 & 0 & 0 \\ 0 & 0 & 0 & 0 \end{pmatrix}, \quad \dots$$

and use them to linearly decompose the two terms appearing in the sum (4.14) Denote

$$\mathbb{X} = [x_{i,j}]_{i=1..12, j=1..12} \quad \text{and} \quad \mathbb{Y} = [y_i]_{i=1..12}$$

the following projections on the canonical base $(E_i)_{i=1..12}$

$$\begin{aligned} \forall j, \sum_{k=1}^K (P_\gamma)_k E_j X_k X_k^T &= \sum_{i=1}^{12} x_{i,j} E_i \\ \sum_{k=1}^K (P_\gamma)_k Y_k (X_k)^T &= \sum_{i=1}^{12} y_i E_i \end{aligned}$$

Assuming \mathbb{X} is invertible ², the cost function $J(\tilde{A}, \tilde{B})$ has a unique minimum in (A_0, B_0) defined by

$$[A_0 \ B_0] = \begin{pmatrix} m_1 & m_4 & m_7 & m_{10} \\ m_2 & m_5 & m_8 & m_{11} \\ m_3 & m_6 & m_9 & m_{12} \end{pmatrix} \quad (4.16)$$

where

$$\begin{pmatrix} m_1 & m_2 & \dots & m_{12} \end{pmatrix}^T = \mathbb{X}^{-1} \mathbb{Y} \quad (4.17)$$

□

This algorithm is further studied in Appendix B. It concludes the proof of Proposition 6 and gives an analytical expression (see Equation (4.16) and Equation (4.17)) of the sought after calibration matrix A_0 and bias B_0 . ■

²This point is still being investigated, as this assumption seems to always hold in practice.

4.4 Calibration of a set of 3-axis magnetometers

We now address the problem of calibrating the array of magnetometers necessary to the implementation of the MINAV technology. The calibration of the sensor array consists in determining A_p and B_p for each sensor, such that

- each sensor considered separately is well calibrated, i.e. its norm is constant if it is rotated in a constant field,
- and all the sensors have the same output when they are put at the same location, i.e. their measurements should have the same norm and the same orientation.

An important issue is to get a data set where, for each sample, all the sensors measure the same field. This assumption may seem trivial, but in fact it implies two strong constraints on data acquisition: both sensors have to actually be exposed to the same field at the same date so that data from both sensors can be compared.

As all the sensors cannot be placed at the exact same location with perfect coincidence, data have to be acquired at a location where the sensed field is uniform. The impact of the presence of a gradient is discussed later on in Section E.3.

Secondly, both sensors have to make their measurements at the same dates. However, it is often not possible when using off-the-shelf digital sensors as discussed in Section 3.1. There are two ways to get round this difficulty. The first one is to wait for a short period of time after each measurement point, i.e. to have quasi-static displacements that can be easily identified in each data set. This allows to pick up at least one sample for each sensor at each measurement point. Such a procedure has a harmful impact on the duration of the data acquisition phase. The second way consists in interpolating the measurements. This requires that sampling dates are precisely known. This is possible using the technique detailed in §3.1.

To perform the calibration, several methods can be envisioned. The presented one extends the one proposed in [32] for a single 3-axis sensor and presents two advantages: it avoids having any sensor playing a particular role, and it uses only one single optimization problem to solve. The iterative calibration is performed *simultaneously* for the two three-axis sensors. Consider a step in the iterations, say the k^{th} . We wish to account for the fact that the sensed field is constant and that it is the same for both sensors. Consider the N data $y_{p,k}(i)$, $i = 1, \dots, N$ for the p^{th} magnetometer. They are initialized with the measurements at step $k = 0$. First, we formulate the cost function to be minimized for sensor p , $p = 1, 2$.

$$f_{p,3}(A, B, y_k) = \sum_{i=1}^N \left\| \left(Ay_{p,k}(i) + B_{p,k}(i) - \frac{y_{1,k}(i) + y_{2,k}(i)}{\|y_{1,k}(i) + y_{2,k}(i)\|} \right) \right\|^2$$

As in the method proposed for calibrating a single sensor, in Section 4.2, the cost function used is quadratic with respect to the coefficients of A and B , yielding easy computation of the solution of the minimization of $f_{p,3}$ with respect to these two arguments. For each sample, the value of the field taken as reference (the same for all magnetometers of the set) is the normalized average $\left(\frac{y_{1,k}(i) + y_{2,k}(i)}{\|y_{1,k}(i) + y_{2,k}(i)\|} \right)$. We note the uniquely defined solution

$$(A_{p,k+1}, B_{p,k+1}) = \operatorname{argmin}_{A,B} f_{p,3}(A, B, y_k)$$

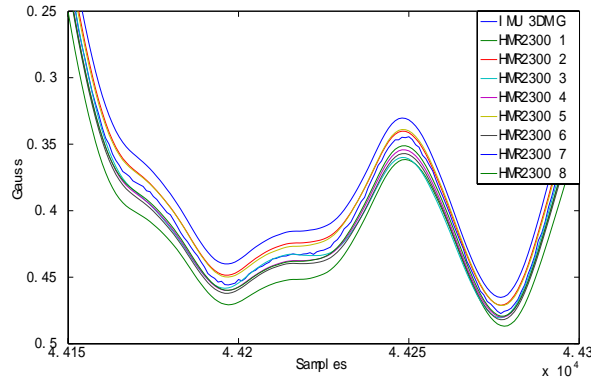


Figure 4.3: The X-Components of 9 magnetometers calibrated separately in a place where the magnetic field is almost uniform. Inconsistencies can be observed.

which is obtained by a classic least-squares solver. Then, we use these matrices to update the data corresponding to each sensor p as follows

$$y_{p,k+1}(i) = A_{p,k+1}y_{p,k}(i) + B_{p,k+1}, \quad \forall i = 1, \dots, N$$

Again, after k such iterations, a matrix $\tilde{A}_{p,k}$ and a bias vector $\tilde{B}_{p,k}$ are obtained recursively for each sensor through

$$\begin{aligned} \tilde{A}_{p,k} &= A_{p,k}\tilde{A}_{p,k-1} \\ \tilde{B}_{p,k} &= A_{p,k}\tilde{B}_{p,k-1} + B_{p,k} \end{aligned}$$

They relate the calibrated data $y_{p,k}(i)$ to the raw measurements $y_p(i)$. Precisely,

$$y_{p,k}(i) = \tilde{A}_{p,k}y_p(i) + \tilde{B}_{p,k}$$

This method have been applied on a set of eight HoneywellTM HMR2300 magnetometers and one 3DMG-X1 from MicrostrainTM together and had the full system travel along an horizontal a-magnetic rail. Prior to this, the magnetometers had all been calibrated separately. The data collected during this experiment are reported in Figure 4.3. They are inconsistent although the sensors were separately calibrated. This stresses the need of a joint calibration. Then, the same experiment was conducted with sensors that were calibrated using the iterative method above. The results obtained during this second experiment are reported in Figure 4.4. In this case, the results are consistent.

4.5 Harmonization of inertial and magnetic sensors

Here, the problem we wish to address is to estimate the harmonization matrix (totally or at least its most impacting terms) between the frame where the velocity is measured or estimated (the frame of the set of spatially distributed magnetometers) and the one in which the attitude is known (the IMU frame).

Consider the following systems, each being attached to a coordinate frame:

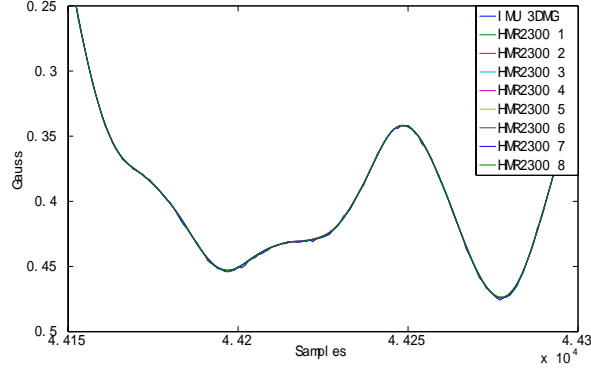


Figure 4.4: The X-Component of 9 magnetometers calibrated all together in a place where the magnetic field is almost uniform. The data are consistent.

- a building considered as the inertial frame of reference \mathcal{R}_i (with its horizontal plane denoted x-y and z pointing upward);
- a pedestrian moving in the building with an attached frame \mathcal{R}_{ped} whose x and y-axis are horizontal and x is pointing forward;
- a subsystem providing an inertial speed expressed in its own coordinate frame \mathcal{R}_{vel} ;
- an IMU providing the attitude of its own coordinate frame \mathcal{R}_{IMU} with respect to the inertial frame of reference \mathcal{R}_i . The attitude is initialized such that the gravity is on the vertical axis ³.

Indices *ped*, *vel*, *IMU* and *I* refer to which frame the corresponding quantity is expressed in. For instance, V_{vel} is the speed expressed in \mathcal{R}_{vel} , whereas V_{IMU} is the same speed expressed in \mathcal{R}_{IMU} . Figure 4.5 pictures the introduced coordinate frames and indicates the rotation matrices between them. The ones of interest are:

- $R_{plane} = R_{ped \rightarrow I}$, rotation matrix from the pedestrian frame to the inertial frame (unknown)
- $R_{body}^T = R_{ped \rightarrow vel}$, rotation matrix from the pedestrian frame to the velocity sensor frame (unknown)
- $R_{harmo} = R_{vel \rightarrow IMU}$, rotation matrix from the velocity sensor frame to the IMU frame (unknown, to be identified)
- $R_{att} = R_{IMU \rightarrow I}$, rotation matrix from the IMU frame to the inertial frame (measured by the IMU).

³ The yaw angle is left free to allow a later absolute alignment (e.g. using a map if one is available).

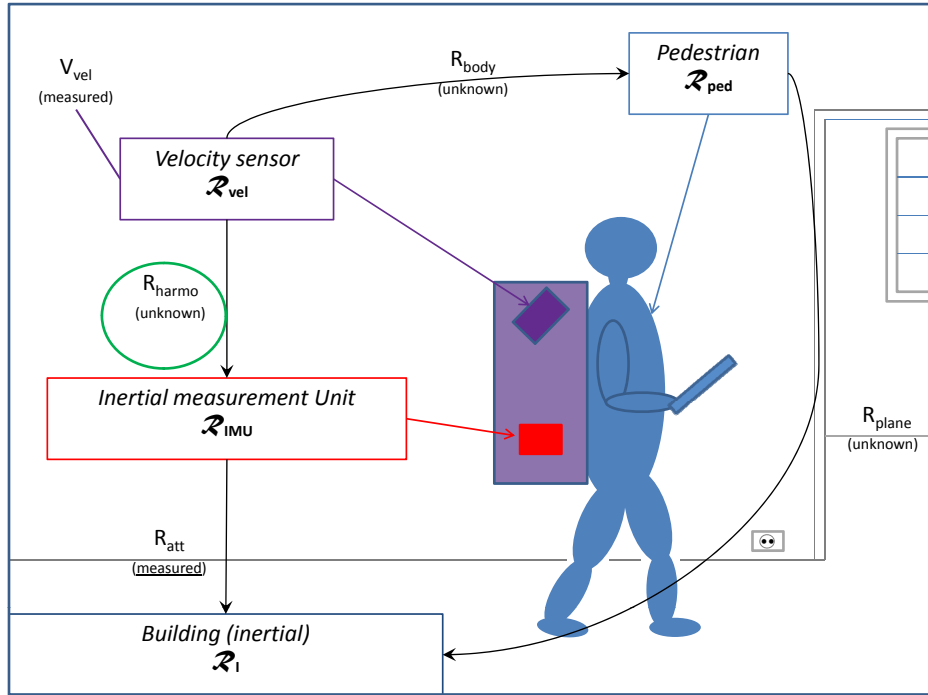


Figure 4.5: Diagram representing the various coordinate frames and rotation matrices of interest in the harmonization problem. The speed V_{vel} is measured in the velocity frame \mathcal{R}_{vel} . The rotation matrix $R_{IMU \rightarrow I} = R_{att}$ is measured. The rotation matrix R_{harmo} is to be identified.

The following useful relations hold

$$V_I = R_{att} R_{harmo} \underbrace{V_{vel}}_{\text{speed which is measured}} \quad (4.18)$$

$$V_{vel} = R_{body}^T V_{ped}$$

and

$$I_3 = R_{att} R_{harmo} R_{body}^T R_{plane}^T$$

which yields

$$V_I = R_{plane} R_{body} V_{vel} \quad (4.19)$$

The most interesting frame to express the speed in is the inertial frame \mathcal{R}_i . Indeed, in this frame, it is possible to integrate it to obtain the trajectory of the pedestrian in the building. However, the speed is measured in the velocity frame \mathcal{R}_{vel} . The matrix R_{body} is unknown and is relatively uncertain because, each time the pedestrian uses the navigation system, it could be put into a slightly different orientation. Finally, R_{plane} is unknown as well. Therefore, the easiest way to express the speed in the inertial frame is to determine

the harmonization matrix $R_{harmono}$ between the velocity frame and the IMU-frame, and thus exploit Equation (4.18) and not Equation (4.19). This matrix depends only on the relative orientations of the two sensor subsystems. The positions and orientations of the subsystems being constant, $R_{harmono}$ needs to be identified only once and for all.

The relative position at any current time T , $P(T) - P(0)$, with respect to an inertial position $P(0)$ is given through

$$P(T) = P(0) + \int_0^T R_{att} R_{harmono} V_{vel} dt \quad (4.20)$$

Ideally, the harmonization matrix $R_{harmono}$ should be close to identity, but errors of a few degrees cannot be avoided in the actual set-up of the subsystems when off-the-shelf packaged sensors are used. In the following, we model the impact on trajectory reconstruction when this matrix is omitted. Then, we show how to compensate for this error.

4.5.1 Identification and correction of trajectory errors due to an harmonization error

Trajectory errors: the shape of the trajectory is altered

For sake of illustration, we consider a particular case where the pedestrian is walking with a speed of constant norm, and, for simplicity, in the forward direction (i.e. along the x -axis of \mathcal{R}_{ped}). First, we assume that the pedestrian frame, the velocity frame and the IMU frame are identical, i.e. that $R_{harmono} = R_{body} = I_3$. So, we have

$$V_{ped} = V_{vel} = V_{IMU} = \begin{pmatrix} V_0 \\ 0 \\ 0 \end{pmatrix}$$

Further, we assume that the pedestrian is walking in an horizontal plane over the time interval $[0, T]$. The IMU attitude is thus expressed using a single angle $\alpha(t)$

$$R_{att}(t) = \begin{pmatrix} \cos(\alpha) & -\sin(\alpha) & 0 \\ \sin(\alpha) & \cos(\alpha) & 0 \\ 0 & 0 & 1 \end{pmatrix} = R(\alpha(t)) \quad (4.21)$$

Through Equation (4.20), one gets

$$P(T) = P(0) + \int_0^T R(\alpha(t)) \cdot V_{IMU} \cdot dt = P(0) + V_0 \int_0^T \begin{pmatrix} \cos(\alpha) \\ \sin(\alpha) \\ 0 \end{pmatrix} \cdot dt$$

Now, assume that the pedestrian has walked along a closed-curve. Then, $P(T) = P(0)$. From the previous equality, we deduce that ⁴

$$\int_0^T \cos(\alpha(t)) dt = \int_0^T \sin(\alpha(t)) dt = 0$$

⁴One shall note that this last property is true even if the velocity V_{IMU} is not aligned with the x -axis but belongs to the $x - y$ plane (see Section 4.5.2).

Now, we introduce an harmonization error, i.e. there is now a rotation $R_{harmono} \neq I_3$ between the coordinate frame where the speed is measured in (\mathcal{R}_{vel}) and the one where the attitude is measured in (\mathcal{R}_{IMU}). We split up $R_{harmono}$ into three successive canonical constant rotations (roll ϕ , pitch θ , and yaw ψ in this order from \mathcal{R}_{IMU} to \mathcal{R}_{vel}) and note $R_{harmono}^T$

$$\begin{pmatrix} c(\psi) & -s(\psi) & 0 \\ s(\psi) & c(\psi) & 0 \\ 0 & 0 & 1 \end{pmatrix} \begin{pmatrix} c(\theta) & 0 & s(\theta) \\ 0 & 1 & 0 \\ -s(\theta) & 0 & c(\theta) \end{pmatrix} \begin{pmatrix} 1 & 0 & 0 \\ 0 & c(\phi) & -s(\phi) \\ 0 & s(\phi) & c(\phi) \end{pmatrix}$$

where $c(\cdot)$ and $s(\cdot)$ stands for $\cos(\cdot)$ and $\sin(\cdot)$ respectively.

Assume that the velocity frame \mathcal{R}_{vel} has been slightly rotated. The speed $V_{IMU} = \begin{pmatrix} V_0 & 0 & 0 \end{pmatrix}^T$ in the IMU-frame is unchanged, but the speed measured in the velocity frame \mathcal{R}_{vel} now writes

$$V_{vel} = R_{harmono}^T \begin{pmatrix} V_0 \\ 0 \\ 0 \end{pmatrix} = V_0 \begin{pmatrix} c(\theta) \cdot c(\psi) \\ c(\theta) \cdot s(\psi) \\ -s(\theta) \end{pmatrix} \neq V_{IMU}$$

If the harmonization error is not taken into account in the trajectory reconstruction, one obtains

$$\begin{aligned} P_r(T) - P(0) &= \int_0^T R_{att}(t) V_{vel} \cdot dt & (4.22) \\ &= V_0 \cdot \int_0^T \begin{pmatrix} c(\alpha(t)) & -s(\alpha(t)) & 0 \\ s(\alpha(t)) & c(\alpha(t)) & 0 \\ 0 & 0 & 1 \end{pmatrix} \begin{pmatrix} c(\theta) \cdot c(\psi) \\ c(\theta) \cdot s(\psi) \\ -s(\theta) \end{pmatrix} \cdot dt \\ &= \begin{pmatrix} 0 \\ 0 \\ -T \cdot V_0 \cdot \sin(\theta) \end{pmatrix}^T \neq 0 = P(T) - P(0) & (4.23) \end{aligned}$$

where the vector $\begin{bmatrix} c(\theta) \cdot c(\psi) & c(\theta) \cdot s(\psi) & -s(\theta) \end{bmatrix}^T$ has been put outside the integral since it is constant.

According to Equation (4.23), the reconstructed position will then slightly, but constantly, drift downward (or upward depending on the signs of θ and V_0) as illustrated in the simulation presented in Figure 4.6. In Figure 4.7, the same drift can be observed on experimental data obtained with one implementation of the MINAV system (presented in details in Chapter 5). As a consequence, even if closed paths are followed, the estimated trajectory will not go back to the starting point as it should. Interestingly, one can note that the two other angles have no impact on Equation (4.23). Only the pitch angle θ alters the shape of the reconstructed trajectory. The trajectory will simply be rotated if the yaw angle is not zero (as illustrated in Figure 4.6 where only the pitch angle is corrected). The roll angle does not have any effect

since the movement is performed along its rotation axis. Note that the error in Equation (4.23) is proportional to the traveled distance $V_0 \cdot T$. An angle as small as 3 *degrees* leads to an error of more than 5% of the traveled distance.

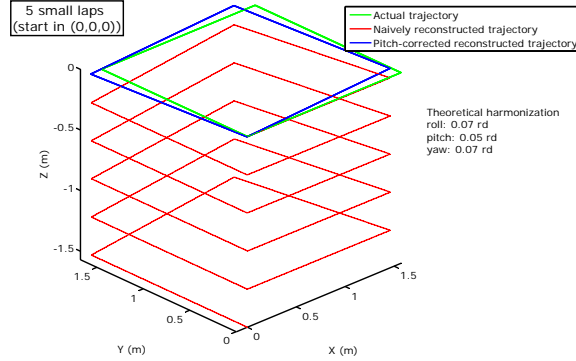


Figure 4.6: Simulation results - The harmonization angles are given on the right of the figure. Neglecting the harmonization, even for low pitch angles, can generate important drifts. Performing the harmonization with only a pitch-angle eliminates the closure error.

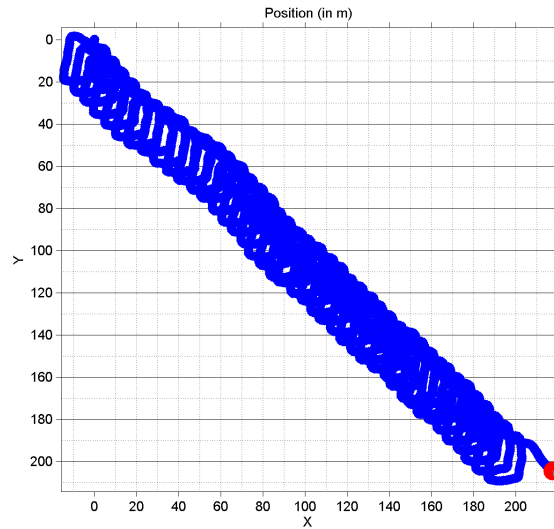


Figure 4.7: Experimental results - Many laps (each being about 90 m long) are performed in the same loop-shaped corridor during about 45 minutes, for a total length of 3 km. The drift, due to the altitude deviation being projected, is clearly visible.

Proposed harmonization procedure (preliminary version)

We have just explained how even a small pitch angle error could alter the shape of the trajectory at a macroscopic scale. A first calibration procedure is proposed in this section. It takes advantage of this property. From the measurements, both the traveled distance $V_0 \cdot T$

and the reconstructed trajectory neglecting the harmonization matrix (Equation (4.22)) are easily computable. They lead to the following simple calibration procedure:

1. Walk along any closed-loop trajectory in the horizontal plane with the following constraints: the speed direction must be kept along the x-axis of the IMU, the velocity should be constant, and the IMU must be kept horizontal (i.e. its z-axis should be kept vertical).
2. Compute the naively reconstructed trajectory according to Equation (4.22) recalled below. Note $P_r(T)$ the final point.

$$P_r(T) - P(0) = \int_0^T R_{att}(t)V_{vel} \cdot dt \quad (4.22)$$

3. Identify the pitch angle θ thanks to Equation (4.23).

$$\sin(\theta) = \|P_r(T) - P(0)\| \cdot \frac{-1}{V_0 \cdot T}$$

This calibration procedure identifies the incriminated angle rather straightforward. Some of the constraints may seem hard to fulfill. However, most of them will be relaxed in Section 4.5.2.

4.5.2 Practical calibration results and limitations

The example of Section 4.5.1 shows a particular case where a single angle is responsible for the non-closing of the reconstructed trajectory. We now present another viewpoint which will allow us to take some further errors in the trajectory reconstruction into account, and remove some constraints from the proposed calibration procedure. We assume that the pedestrian is performing a closed-loop trajectory with the time-varying speed in a constant direction in its own frame \mathcal{R}_{ped} (forward for instance, as in Section 4.5.1). The speed direction is then constant in the three frames \mathcal{R}_{ped} , \mathcal{R}_{vel} , and \mathcal{R}_{IMU} (but the speed directions do not have the same expressions in the three frames).

Again, from Equation (4.20), we have

$$P(T) - P(0) = \int_0^T R_{att}(t)R_{harmo}V_{vel}(t)dt$$

The speed direction being constant in the velocity frame, it can be put outside the integral sign, allowing to put the constant matrix R_{harmo} outside the integral sign too. Denote $\frac{V_{vel}}{\|V_{vel}\|}$ the constant speed direction in the velocity frame, and $v_{vel}(t) = \|V_{vel}(t)\|$ its magnitude. Then, one gets

$$P(T) - P(0) = \underbrace{\int_{t_0}^T v_{vel}(t)R_{att}(t)dt}_M R_{harmo} \frac{V_{vel}}{\|V_{vel}\|} \quad (4.24)$$

If the path followed by the pedestrian is a closed-loop trajectory, $P(T) = P(0)$, which means that M has not full rank and R_{harmo} must send $\frac{V_{vel}}{\|V_{vel}\|}$ in the kernel of M . Further, M has the following property.

Proposition 7: Consider a plane closed trajectory followed with a constant speed direction in the \mathcal{R}_{ped} frame of reference (without spinning around that direction), starting at time $t=0$ and ending at time $t=T$. Denote the speed magnitude

$$v_{vel}(t) = v_{IMU}(t) = \|V_{vel}(t)\|$$

Then, the 3x3 matrix

$$M = \int_0^T v_{IMU}(t) R_{att}(t) dt$$

has rank 1, and its only non-zero singular value is the traveled distance. \square

Proof: First assume that the IMU has its x and y axis in the horizontal plane. The attitude is then a simple rotation around the vertical z axis defined by a single angle $\alpha(t)$ as already defined in Equation (4.21).

$$R_{att}(t) = \begin{pmatrix} \cos(\alpha(t)) & -\sin(\alpha(t)) & 0 \\ \sin(\alpha(t)) & \cos(\alpha(t)) & 0 \\ 0 & 0 & 1 \end{pmatrix} \quad (4.21)$$

For any constant speed direction

$$\frac{V_{IMU}}{\|V_{IMU}\|} = \begin{pmatrix} v_x \\ v_y \\ 0 \end{pmatrix}$$

chosen in the horizontal plane of the IMU-frame, as long as the starting point and the end point are identical, we get

$$0 = \left(\int_0^T v_{IMU}(t) \begin{pmatrix} c(\alpha) & -s(\alpha) & 0 \\ s(\alpha) & c(\alpha) & 0 \\ 0 & 0 & 1 \end{pmatrix} dt \right) \begin{pmatrix} v_x \\ v_y \\ 0 \end{pmatrix} \quad (4.25)$$

where $v_{IMU}(t) = \|V_{IMU}(t)\|$. Equation (4.25) gives a linear equation in $(v_x \ v_y)^T$

$$\underbrace{\begin{pmatrix} \int_0^T v_{IMU}(t)c(\alpha) & -\int_0^T v_{IMU}(t)s(\alpha) \\ \int_0^T v_{IMU}(t)s(\alpha) & \int_0^T v_{IMU}(t)c(\alpha) \end{pmatrix}}_A \begin{pmatrix} v_x \\ v_y \end{pmatrix} = \begin{pmatrix} 0 \\ 0 \end{pmatrix}$$

As $(v_x, v_y) \neq (0, 0)$, we deduce that A has not full rank. Yet,

$$\underbrace{\det(A)}_{=0} = \left(\int_0^T v_{IMU}(t)c(\alpha) dt \right)^2 + \left(\int_0^T v_{IMU}(t)s(\alpha) dt \right)^2$$

which is null if and only if both squared terms are null, i.e.

$$\int_0^T v_{IMU}(t)c(\alpha)dt = 0 \quad \text{and} \quad \int_0^T v_{IMU}(t)s(\alpha)dt = 0$$

Replacing those quantities in Equation (4.25) yields

$$M = \begin{pmatrix} 0 & 0 & 0 \\ 0 & 0 & 0 \\ 0 & 0 & \int_0^T v_{IMU}(t)dt \end{pmatrix}$$

which shows that M is of rank 1.

The starting frame on the right side of R_α and the arrival frame on the left side of R_α can be rotated by some orthogonal matrices P and Q , taking into account the fact that the IMU is not horizontal anymore (P) and that the coordinate frame of the inertial frame is arbitrary (Q).

We can get rid off P and Q under the integral sign since they are constant. This yields

$$M = \int_0^T v_{IMU}(t)Q^T \begin{pmatrix} \cos(\alpha) & -\sin(\alpha) & 0 \\ \sin(\alpha) & \cos(\alpha) & 0 \\ 0 & 0 & 1 \end{pmatrix} P dt = Q^T \begin{pmatrix} 0 & 0 & 0 \\ 0 & 0 & 0 \\ 0 & 0 & \underbrace{\int_0^T v_{IMU}(t)dt}_{\text{traveled distance}} \end{pmatrix} P$$

which is the sought after singular value decomposition of M with the traveled distance as only non-zero singular value. ■

According to Equation (4.24), to close the reconstructed trajectory, and thus correct the pitch angle discussed in Section 4.5.1, one simply has to find an harmonization matrix that sends $\frac{V_{vel}}{\|V_{vel}\|}$ in the vector space of the null singular value of M . For instance, a rotation matrix that sends $\frac{V_{vel}}{\|V_{vel}\|}$ on the direction of its projection on the plane of null singular value is a solution ⁵.

Accounting for experimental data errors

In practice, the actual attitude and the actual velocity are almost never known, but estimated. Information about those quantities is provided through sensors, either directly or, more often, through data filtering. Denote by index f the corresponding filtered quantities that are available. By integration, one gets the reconstructed position $P_r(t)$

$$P_r(T) - P(0) = \underbrace{\int_0^T v_{vel}^f(t)R_{att}^f(t)dt}_{M^f} R_{harmono} \frac{V_{vel}^f}{\|V_{vel}^f\|}$$

As stated in Proposition 7, M has a plane of null singular values and its only non-zero singular value is the traveled distance. Due to the limited bandwidth of the sensors and

⁵Note that this plane corresponds to the degree of freedom left by the yaw angle ψ in Section 4.5.1.

the filters, M^f does not have a plane of perfectly null singular value. As a consequence, the reconstructed trajectory cannot be made perfectly closed thanks to an harmonization matrix. However, M^f is not very different from M . Experiments show that the singular values of M^f are close to those of M : two are close to zero (almost identical), and a third one is close to the traveled distance. The closure error can be minimized by choosing an $R_{harmono}$ sending $\frac{V_{vel}^f}{\|V_{vel}^f\|}$ in the vector space of the two smallest singular values. If the speed direction has been kept perfectly constant in the pedestrian frame \mathcal{R}_{ped} , the smallest singular value is indeed the lowest closure error that can be achieved by choosing $R_{harmono}$.

Proposed harmonization procedure

A first calibration procedure has been proposed in Section 4.5.1. Some constraints, potentially hard to fulfill without dedicated equipment were required to perform that procedure. The approach presented above allows to remove or weaken most of them in a new calibration procedure. We now present this procedure.

1. Walk along any closed-loop trajectory in the horizontal plane with the following constraint: the speed direction must be kept along the x-axis of the IMU.
2. Compute the matrix

$$M_f = \int_0^T v_{vel}^f(t) R_{att}^f(t) dt$$

3. Identify the plane of smaller singular values of M_f (supposed to be identical).
4. Find a rotation matrix $R_{harmono}$ which sends the speed direction $V_d = \frac{V_{vel}^f}{\|V_{vel}^f\|}$ to its

projection $P(V_d) = P\left(\frac{V_{vel}^f}{\|V_{vel}^f\|}\right) / \left\| \frac{V_{vel}^f}{\|V_{vel}^f\|} \right\|$ in that plane of singular values, for instance thanks to Olinde Rodrigues' formula.

$$N = \frac{P(V_d) \times V_d}{\|P(V_d) \times V_d\|} = \begin{pmatrix} N_1 \\ N_2 \\ N_3 \end{pmatrix}$$

$$\alpha = \arccos(V_d^T P(V_d))$$

$$R_{harmono} = \cos(\alpha) I_3 + (1 - \cos(\alpha)) N N^T + \sin(\alpha) \begin{pmatrix} 0 & -N_3 & N_2 \\ N_3 & 0 & -N_1 \\ -N_2 & N_1 & 0 \end{pmatrix}$$

Compared to the preliminary version of the procedure in Section 4.5.1, two requirements have been removed: keeping the speed constant and the z-axis vertical. The required trajectory is now simply the one naturally performed by any pedestrian walking, for instance, in a loop-shaped corridor. This allows the system to be calibrated very easily in the field by any operator.

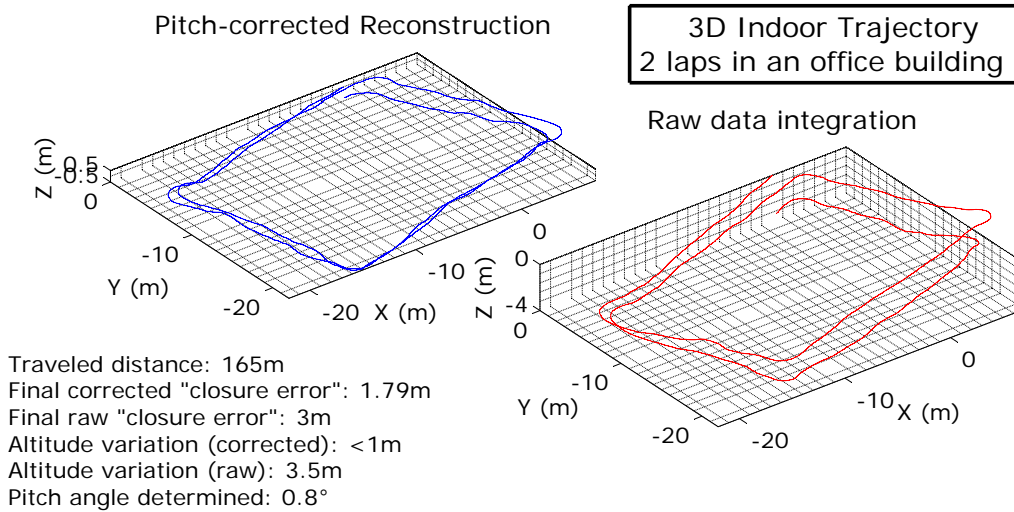


Figure 4.8: Experimental data - The pitch-angle has been corrected. The trajectory does not drift downward anymore.

4.6 Proposed operational procedure to calibrate a MINAV system

In summary of this chapter, we propose here an operational procedure to calibrate a MINAV system. We consider the application described in Chapter 3, the MINAV pedometer. As pictured in Figure 5.1, this system is constituted of two sensing modules (velocity sensor and IMU) that are rigidly attached to a rigid body, and then carried by a pedestrian one wishes to estimate the motion of.

To calibrate the MINAV systems, three steps have to be performed. They constitute the following procedure.

1. Calibrate the IMU
 - Calibrate the 3-axis accelerometer, use Algorithm 1 in Section 4.2.3.
 - Calibrate the 3-axis gyroscope with respect to the 3-axis accelerometer, use Algorithm 2 in Section 4.3.
2. Calibrate the velocity sensor, i.e. calibrate each magnetometer and simultaneously harmonize the set of magnetometers, use the algorithm described in Section 4.4.
3. Harmonize the velocity sensor and the IMU, use the "Harmonization procedure" of Section 4.5.

Chapter 5

Real case study: the MINAV pedometer

Cas d'étude réel: le podomètre MINAV

Ce chapitre est consacré à une application particulière de localisation de piétons dans les bâtiments, même si, comme les résultats présentés dans ce chapitre le montrent, la technique MINAV permet aussi la navigation dans les rues, et à l'extérieur des bâtiments. Ces zones, où l'on ne peut utiliser le GPS, présentent un terrain particulièrement favorable à la technique MINAV. Les bâtiments présentent de nombreuses sources de perturbation du champ magnétique. Le béton armé des murs, les cadres de portes, les forts courants électriques environnants en font partie. Il en résulte un champ magnétique avec de fortes variations, qui peuvent être mesurées par des magnétomètres relativement bas-coûts. De nombreuses techniques de positionnement dans les bâtiments ont vu le jour ces dernières années. Les principales d'entre elles sont passées en revue en Section 5.1. Nous proposons ensuite, en Section 5.2, un système MINAV pour le piéton, tant du point de vue matériel que du point de vue des algorithmes. Enfin, le système est évalué dans des environnements urbains variés en Section 5.3.

The principles of MINAV have been explained in Chapter 2. A suitable measurement system and its calibration have been detailed in Chapter 3 and Chapter 4, respectively. Finally, in this chapter, we present an application to indoor pedestrian navigation, i.e. navigation of a pedestrian inside buildings, even if, as will appear in the results, reliable position estimates can also be obtained outside buildings, in the streets. These GPS-denied areas are ideally suited for MINAV. Buildings provide countless sources of stationary magnetic field distortions. The reinforced concrete used in walls, the door frames, the strong electric currents, for instance, range among them. Their contributions result in a magnetic field with spatial variations that can be easily measured by rather low-cost magnetometers.

After briefly reviewing the main navigation techniques that are currently envisioned for indoor navigation in Section 5.1, our proposed MINAV system for pedestrians is detailed

in Section 5.2 both from the hardware and software points of view. Finally, in Section 5.3, the system is evaluated in various environments.

5.1 State of the art of indoor positioning and navigation techniques

As already discussed in the introduction of this thesis, localization technologies have become available to the general public thanks to the widespread use of GPS receivers. However, some limitations were quickly pointed out: the accuracy significantly drops in many places where satellites coverage is not necessarily reliable. In cities, the accuracy drops even more with the many reflections (multipaths) and the GPS signals can even be completely lost in urban canyons, and, obviously, in buildings or underground. Many works has been conducted in the past decade to overcome this limitation, both by improving the GPS receivers (enhanced handling of low signal to noise ratio, compensation for signal multipaths, among others) and by developing alternate techniques.

The positioning solutions envisioned by research teams are numerous and several criteria can be used to classify them. For pedestrian navigation, one can first distinguish between solutions where the positioning estimate is computed at the level of the receiver and solutions where this computation is done externally, for instance at the level of a network of sensors tracking the pedestrian who can be requested to wear a tracking beacon. Further, the type of sensors used vary from one technique to another. The technologies involved can be passive or active. They can consist in cameras, lasers, inertial sensors, magnetometers, ultrasound devices, or most often radio-frequency receivers designed for signals of various range: Ultra-Wide Band (UWB) [49], Wifi (IEEE 802.11b), Bluetooth (IEEE 802.15), GSM [21, 53], RFID (Radio-Frequency IDentification, or even pseudolites (GPS-like signals emitted by ground stations). The signal metrics used for the radio signals can be the most common Receiver Signal Strength (RSS), the Time of Arrival (ToA), the Time Difference Of Arrival (TDoA), or (less often) the Angle of Arrival (AoA). Finally, one criterion of importance for many applications is the need for pre-installed infrastructure (visual markers, radio emitters, magnetic beacons to name a few) We now present briefly some of the most common techniques.

Most of the network based positioning techniques rely on radio-frequency signal, and almost all the radio-frequency approaches are using a network, whether dedicated to the positioning solutions, or shared with other usages, pre-installed in the building or deployable at the time of the positioning needs. The transmission of the radio signal indoor is altered by the many obstacles and reflections, which has a detrimental effect on the resulting accuracy of the system. Ultra-wide band signals are spreading since they can lower the cuts that occurs at some frequencies depending on the building.

Some of those techniques can achieve very accurate positioning provided the network is sufficiently dense. However, deploying and maintaining this network can reveal extremely costly. In many applications, such as those for first responders, one cannot afford to deploy such networks in advance. Self-deployable networks are possible, but the process can be time consuming, suffer from the relative inaccuracy of the deployed nodes, and the risk of not covering the entire targeted area remains.

Cell-ID Almost all the radio-frequency approaches rely on a network of devices to estimate the position of moving pedestrians. A first and easy approach consists in identifying the pre-installed network node in range and, knowing its position, associate the position of the pedestrian to the cell associated to the node. This can, for instance, be achieved by means of magnetic beacons, RFID tags [52], Bluetooth or GSM cells, ultrasound emitters or visual markers [83]. The accuracy and the number of nodes to deploy directly depend on the range of the emitters (or the line of sight of the marker). A single GSM emitter can cover a rather wide area outdoor, while RFID tags only range from several centimeters for passive tags to a few meters for active tags. Overlapping of cells, often happens in GSM networks. This permits to refine the position by intersecting areas of possible position. RFID tags are rather inexpensive but have to be deployed in large numbers to cover an area. Bluetooth cells can provide a limited communication channel but are rather expansive. GSM cells have the advantage of being already deployed for mobile phone applications and also provide limited communication capabilities. However, their wide range intrinsically limits their accuracy.

Traveled distance estimation Thanks to propagation models, the Receiver Signal Strength (RSS), the Time of Flight (ToF) or the Time of Arrival (ToA) for synchronized devices, can be associated to a distance between the emitter and the receiver. When only one emitter is detected, it can only be known that the receiver lies somewhere on a sphere around the emitter. When at least three emitters are in range, the position can be computed. This technique yields more precise results than simple Cell-ID positioning, and can be applied to various signals, for instance ultrasound, GSM, Wifi, UWB, or even to magnetic nodes [15]. These techniques perform well in open-space, but indoor, they are subject to many reflections and attenuations that are very difficult to model, and, which, in turn, dramatically limit their accuracy.

Lateration A pulse emitted by a node arrives at slightly different times at two (or more) spatially distributed receivers. This Time Difference of Arrival (TDoA) is related to the distance between the emitter and the two receivers being slightly different. Given one emitter and two receivers, it can be established that the locus of the emitter relatively to the receivers lies on an hyperboloid. Having either more emitters or receivers permits to fully determine the relative location of the emitter, or inversely, to determine the position of the receivers with respect to the known position of the node. This can be (easily) used with ultrasound since the velocity of the sound is rather slow (compared to the velocity of light). Inversely, two or more signals emitted from spatially separated but well-synchronized nodes arrive at a single receiver location with TDOA allowing similar computation. Such techniques can be used with UWB, pseudolites or Wifi signals for instance. Wifi stations have the advantage of providing interesting communication capabilities but are rather expansive and their range is much shorter than UWB, whose large spectrum of emission permits to limit the signal strength attenuation compared to the other radio signals.

Fingerprinting The fingerprinting technique consists in building a map of the area where the position has to be estimated later, and associate to each location (each room for instance) all signals received and their strength, with gives a supposedly unique fingerprint of the location, for instance the available Wifi, GSM or WLAN networks or even FM-radios and their strength. Those data are stored in a database. When the pedestrian equipped with

the positioning system moves in the area, the signals and their strengths are measured again and compared against the database. Providing that the available signals and their strengths do not vary too much, there is a match in the database that gives the current location. Used with Wifi signals and smartphones, it yields rather inexpensive positioning solutions and is particularly adapted to leader-follower scenarios. Yet, its accuracy, and its availability cannot be guaranteed, since the fingerprint can change over time, which completely discards the method for many applications. This fingerprinting technique however, does not necessarily rely on a base station network. The fingerprint can take part of the environment. It has, for instance, also been applied with camera by extracting main features of pictures.

Magnetic map matching The usually considered application of magnetometers is called magnetic field navigation [102]. It completely differs from the MINAV approach presented in this thesis. This method uses the variations of the magnetic field to identify users position using a map-matching technique. It assumes that a map of the magnetic field has been previously obtained and uses current measurements to establish the position on this map according to a maximum likelihood criterion. Magnetic map matching techniques exploit the fact that, as has been noted by practitioners, for indoor environments in particular, the magnetic maps feature distinctive spatial variations that can be matched with a priori information using the previously mentioned maximum likelihood technique [50]. In practice, anchors or magnetic material can be installed in the building to help distinguish between several possible signatures.

More generally, map matching consists in identifying some precise location both on an a priori given map and in the embedded positioning system to be able to pin-point the exact location on the map and thus correct the drift that has occurred until that point. The features used to identify a location can be stairs or corners for instance [24]. A complementary approach is to simply prevent pedestrian from crossing walls as proposed in [114].

Optical system Optical positioning covers various techniques. Markers (bar codes for instance) permits to act like in the case of cell-ID, and if the size of the tag is normalized, one can compute an estimate of the distance (and even, in some cases, an orientation) from the embedded sensor to the tag. Without markers, the fingerprinting technique can be used. Pictures taken beforehand (or the main features extracted from them) can be used as signatures. Other methods rely on geometric analysis of collections of successive images to estimate the motion [82]. Used alone, these methods, often complemented by a laser to estimate the depth of the picture, drift just like any other dead reckoning system. Finally, some systems build metric or topological [70] representations or maps of the user's exploration path as it is explored, performing a Simultaneous Localization And Mapping (SLAM) [28, 29, 47]. The map is built with the drift inherent to the method used in dead reckoning, but as long as one remains in the explored map, the drift of the positioning solution theoretically stops growing.

ZUPT Probably, the philosophy most similar to the one we consider in the MINAV technique is the ZUPT method. This similarity stems from the fact that this method does not use any exterior source of information and aims at resetting the velocity estimate. Yet, the way this reset is performed is very different from the continuous update produced by the observability of the body velocity variable granted by the magnetic field spatial variations

information in the MINAV technique. The ZUPT consists in using a zero-velocity update (ZUPT). In [24, 46], an IMU is placed on the shoe of the pedestrian for which the navigation problem is to be solved. The IMU is used in a conventional DR approach. Periodically, the velocity estimate is reset when the foot touches the ground. Detection is performed by investigating noise levels of the IMU sensors (see [101] for a comparison of different criteria). Very good performance have been reported by several teams [24, 46, 65, 84]. The method has been extended to attitude update (AUPT) [24].

Many systems are proposed that complement the short term accuracy of inertial navigation with other previously mentioned techniques to lower or even bound the position error. One can for instance mention the coupling of inertial and optical measurements [7], the use of inertial navigation to deploy a network of RFID tags [93], or inertial navigation coupled with ultrasound nodes [43].

5.2 Implementing the MINAV methodology

5.2.1 Hardware

We consider the sensors setup presented in Section 3.5. Their design complies with the guidelines of Chapter 3.

Keeping the considerations of real-time implementation discussed in Section 3.1 in mind, a robust two-processor embedded system has been developed (see [20, 58] for further detail on embedded software design). Each processor runs a distinct software and the two communicate via a simple RS232 serial link. The first processor is used to gather data from the sensors, while the second one performs the data fusion calculation. It is fast enough to run a low-dimensional EKF algorithm at 76 Hz. The advantages of this architecture are as follows: *i*) task-scheduling is easily programmed since only one of the processors is in charge of handling the various sensors; *ii*) new data fusion algorithms can be easily uploaded, because the scheduling of tasks is not impacted; *iii*) depending on the computational requirements, the computation board can be replaced and upgraded without interfering with the data acquisition process and its task-scheduling; *iv*) finally, the measurement system is quite low-cost, since it relies on off-the-shelf components and can be easily maintained.

As exposed in Figure 5.1, this (modular) embedded measurement system consists of four modules.

The first module is the sensor module consisting in a rigid body with strapdown magnetometers and inertial sensors. The sensors have been described in Section 3.5. An electric hub connects all the in and out wires to a single connector. This connector is linked to the data acquisition module..

The core of this acquisition module is an MPC555 microcontroller from MotorolaTM. This microcontroller has substantial computational capabilities and a large number of versatile and programmable input/output ports. In particular, an extensive use of UARTs is made (QSCI1, queued serial communication interface, and SCI2), TPUs (time processing units used as customized additional UARTs, see [81]), i.e. in total 8 UARTs. Finally, it is small (credit card format) and has a low weight.

The data acquisition software running on the microcontroller is event-driven, driven by the IMU messages, which are 31 bytes long. Magnetometers measurements are received at 154 Hz and are buffered until a message from the IMU is received and validated by the



Figure 5.1: Schematic view of the multi-module system.

microcontroller. Information from the magnetometers is then picked up in the data buffers. Those pieces of information are then gathered together into a 116 byte message containing all of the on board measurements and sent through a serial port.

The output message of the measurement module is detailed in Table 5.1.

This message is received by the computation board where the velocity and position estimation is actually performed. Then, estimates are sent to a display module for real-time reporting of position data. We now describe these two modules further.

The computation board consists in a PC running a customized Linux distribution based on a Debian kernel. The PC board was selected among numerous models based on computational power, energy consumption, toughness, size and price. The chosen calculation board has a standard pico-ITX PC architecture. Its processor is a 1.2 GHz C7-M from VIA designed for embedded applications. It can perform 1500 MIPS and presents classic PC I/O ports such as two UARTs (used as main data links with the acquisition module and the display module), an Ethernet board (not used here), a VGA output (which turns out to be convenient for monitoring purposes during debugging phases of the software and hardware development), a keyboard, and several USB ports (which may be considered for plugging future devices such as cameras). The operating system is installed on a 1 Gbyte disk-on-chip system which prevents all possible mechanical failure associated to traditional hard-drives. This flash memory device is directly connected to the mother board through its IDE port. A pico-PSU device is used

5.2. IMPLEMENTING THE MINAV METHODOLOGY

Bytes	Data	Description
1-3	0xFC FB FA	Headers
4-11	QUAT	Attitude quaternion
12-17	ACC	Accelerometers measurements
18-23	GYR	Gyrometers measurements
24-25	TT	Timer Tick of the IMU
26-31	LMAG1	Last measurements of the 1 st magnetometer
32	LTSM1	Timestamp of the last measurement of the 1 st magnetometer
33-38	LMAG2	Last measurements of the 2 nd magnetometer
39	LTSM2	Timestamp of the last measurement of the 2 nd magnetometer
40-45	LMAG3	Last measurements of the 3 rd magnetometer
46	LTSM3	Timestamp of the last measurement of the 3 rd magnetometer
47-52	LMAG4	Last measurements of the 4 th magnetometer
53	LTSM4	Timestamp of the last measurement of the 4 th magnetometer
54-59	LMAG5	Last measurements of the 5 th magnetometer
60	LTSM5	Timestamp of the last measurement of the 5 th magnetometer
61-66	LMAG6	Last measurements of the 6 th magnetometer
67	LTSM6	Timestamp of the last measurement of the 6 th magnetometer
68-73	PMAG1	Penultimate measurements of the 1 st magnetometer
74	PTSM1	Timestamp of the penultimate measurement of the 1 st magnetometer
75-80	PMAG2	Penultimate measurements of the 2 nd magnetometer
81	PTSM2	Timestamp of the penultimate measurement of the 2 nd magnetometer
82-87	PMAG3	Penultimate measurements of the 3 rd magnetometer
88	PTSM3	Timestamp of the penultimate measurement of the 3 rd magnetometer
89-94	PMAG4	Penultimate measurements of the 4 th magnetometer
95	PTSM4	Timestamp of the penultimate measurement of the 4 th magnetometer
96-101	PMAG5	Penultimate measurements of the 5 th magnetometer
102	PTSM5	Timestamp of the penultimate measurement of the 5 th magnetometer
103-108	PMAG6	Penultimate measurements of the 6 th magnetometer
109	PTSM6	Timestamp of the penultimate measurement of the 6 th magnetometer
110-111	CHKSUM	Checksum

Table 5.1: Output of the measurement system. This message of 111 bytes is delivered at 76 Hz.

Bytes	Data	Description
1	0xFC	Header
2-7	P_x, P_y, P_z	Position with respect to the starting point (Inertial reference frame)
8-13	u, v, w	Body velocities (Body reference frame)
14-21	Q0,Q1,Q2,Q3	Attitude quaternion (Body reference frame)
22-23	TT	Timer Tick
24-25	CHKSUM	Checksum

Table 5.2: Output of the computation board. This message of 25 bytes is delivered at 76 Hz.

as power supply. The computation softwares are written in C and can be updated directly on the board, where a compiler is available, or uploaded in as already executable file. Customs scripts (e.g. makefiles) for compiling and deploying the executable code and configuration files are an efficient way to upgrade the software during development and testing. Two SD cards slots have been added to record all data coming in (measurements described in Table 5.1) and out (position estimates described in Table 5.2) of the module, which is very convenient not only during development and debugging phases, but also to record all the scenarii performed with the system.

Finally, the display module implements all the user interface software. The user can provide a starting point and an initial attitude which are required to compute a position. The current position is then displayed on screen in real time. Saved past scenarii can also be replayed for further analysis. From the hardware point of view, this display module simply consists in a tablet PC¹.

5.2.2 Software

Model We now detail the implementation of the principles of MINAV thoroughly explained in Chapter 2 for a pedestrian positioning system. The state considered gathers the magnetic field B and the velocity V , both expressed in the body reference frame. According to Section 2.1, the dynamics of the magnetic field, projected in the body frame of reference, writes

$$\begin{pmatrix} \dot{B}_x \\ \dot{B}_y \\ \dot{B}_z \end{pmatrix} = - \begin{pmatrix} p \\ q \\ r \end{pmatrix} \wedge \begin{pmatrix} B_x \\ B_y \\ B_z \end{pmatrix} + \left(\frac{\partial (B)_b}{\partial \mathcal{B}_b} \right) \begin{pmatrix} u \\ v \\ w \end{pmatrix} \quad (2.6)$$

¹As a trade-off between cost, ease of use and ... design, we chose an eeePC from Asus, which looks like a tablet, but whose screen hides a true keyboard very helpful when it comes to debugging or showing some more figures at the end of an exhibition.

In Chapter 2, we considered the rigid body to be subject to a zero-mean total force. In the case of the pedestrian, we use a different model and consider the velocity to be an unknown constant in the body frame. This is a modeling consistent with [6], where it is shown that the velocity expressed in the body frame of reference usually keeps a constant direction in turns. The dynamics of the the velocity could be modeled a bit further. Some works have been conducted in biomechanics about the move of the different body segments with respect to the others, but few results have emerged at the macroscopic scale, the human body being largely over actuated. This is a point for future investigations.

Accounting for the equation

$$\begin{pmatrix} \dot{u} \\ \dot{v} \\ \dot{w} \end{pmatrix} = \begin{pmatrix} 0 \\ 0 \\ 0 \end{pmatrix}$$

finally, the system to be observed writes

$$\frac{d}{dt} \begin{pmatrix} (B)_b \\ (V)_b \end{pmatrix} = \begin{pmatrix} -[(\Omega)_b] & \left(\frac{\partial(B)_b}{\partial B_b}\right) \\ 0_{3 \times 3} & 0_{3 \times 3} \end{pmatrix} \begin{pmatrix} (B)_b \\ (V)_b \end{pmatrix} \triangleq A \begin{pmatrix} (B)_b \\ (V)_b \end{pmatrix} \quad (5.1a)$$

$$y = \begin{pmatrix} I_3 & 0_3 \end{pmatrix} \begin{pmatrix} (B)_b \\ (V)_b \end{pmatrix} \triangleq C \begin{pmatrix} (B)_b \\ (V)_b \end{pmatrix} \quad (5.1b)$$

Filter Observability of (5.1) has been studied in Section 2.1, where a non-linear observer has been proposed. For sake of performance and ease of tuning, we chose to implement a Kalman filter (KF). The matrix A is determined from the measurements of the measurement system (see Table 5.1). Classically, this filter proceeds in two steps. In the prediction step, the state is propagated at the next time step by integrating the dynamics. Quantities with index p are relative to this prediction step. In the estimation step, mentioned by index e , the measurements are taken into account to correct the prediction. For convenience, we recall here the main equations of these two steps. (The reader can refer to [63] for background on this algorithm.)

At the discrete time k , using the time step δt , consider $\hat{X}_p[k]$ the vector containing estimates at index k of $(B)_b$ and $(V)_b$, and $\hat{X}_e[k]$ a vector of the same size 6×1 . Denote Σ_p the 6×6 covariance matrix of the state used for prediction and Σ_e the 6×6 covariance matrix of the state used for estimation. The 6×6 covariance matrix of the noise dynamics is denoted M_η , and the 3×3 covariance matrix of the measurement noise is M_ρ . The updates are as follows

$$\begin{aligned} \hat{X}_p[k+1] &= (I + A\delta t) \hat{X}_e[k] \\ \Sigma_p[k+1] &= (A + A \cdot \delta t) \Sigma_e[k] (I + A \cdot \delta t)^T + M_\eta \\ K &= \Sigma_p[k+1] C^T (C \Sigma_p[k+1] C^T + M_\rho)^{-1} \\ \hat{X}_e[k+1] &= \hat{X}_p[k+1] + K (Y - C \hat{X}_p[k+1]) \\ \Sigma_e[k+1] &= \left(\Sigma_p[k+1]^{-1} + C^T M_\rho^{-1} C \right)^{-1} \end{aligned}$$

Integration scheme The data fusion algorithm is implemented on board a PC based system which performs the successive updates detailed above. Surprisingly enough, this (one step forward Euler) integration scheme exposed in the update above can reveal troublesome, and can be the cause of unexpectedly misleading results.

Simple investigations reveal that, more generally, usual explicit or implicit Euler numerical schemes are unable to reproduce pure rotational terms in the dynamics (2.6). For instance, a direct computation shows that, in the absence of any source term, while the analytical solution of

$$\frac{d}{dt} \begin{pmatrix} B_x \\ B_y \\ B_z \end{pmatrix} = - \begin{pmatrix} p \\ q \\ r \end{pmatrix} \times \begin{pmatrix} B_x \\ B_y \\ B_z \end{pmatrix}$$

has a constant norm, solutions determined using Euler schemes do not and, rather, feature clearly wrong values of this norm. An explicit Euler numerical scheme indeed yields

$$\begin{aligned} (B)_b [t_{n+1}] &= (B)_b [t_n] + \frac{d}{dt} (B)_b [t_n] \delta t \\ (B)_b [t_{n+1}] &= (B)_b [t_n] - (\Omega_{b/i})_b \times (B)_b [t_n] \delta t \end{aligned}$$

The norm of the integrated magnetic field thus evolves according to

$$\|(B)_b [t_{n+1}]\|^2 = \|(B)_b [t_n]\|^2 + \delta t^2 \left\| (\Omega_{b/i})_b \times (B)_b [t_n] \right\|^2$$

Whenever the rotation rate is not null, one thus has

$$\|(B)_b [t_{n+1}]\| > \|(B)_b [t_n]\|$$

In the data fusion algorithm, this numerical effect is promptly interpreted as a fictitious variation of the magnetic field, wrongly attributed to a displacement of the rigid body.

To address this problem, we have realized that one can simply use a numerical scheme well-suited for rotational dynamics such as the ones developed in celestial mechanics studies. One can for instance use a Gauss-Jackson scheme (see e.g. [10, 14, 98]). An alternative is to consider higher order schemes as Adam-Bashforth's extrapolation formula [1, §25.5.4, p.896]. This integration scheme is detailed in Appendix G.

5.3 Experimental results

5.3.1 1-dimensional in-lab experiments

1-dimensional experiments have been conducted to validate the accuracy of the velocity estimation. First, the MINAV system has been translated back and forth along an a-magnetic rail, by small increment of 1 cm every 5 s. The results are presented in Figure 5.2. The increment are clearly visible on the estimated velocity. This estimates reacts quickly to the small impulsion and comes back quickly to zero afterwards. Integrating this velocity provides an estimate of the position. The reconstructed position reproduces the steps rather accurately going over 5 cm in 5 steps, forward as well as backward.

To validate more accurately the estimated velocity obtained with the system, the MINAV system has been translated in a long corridor. The platform has been moved back and

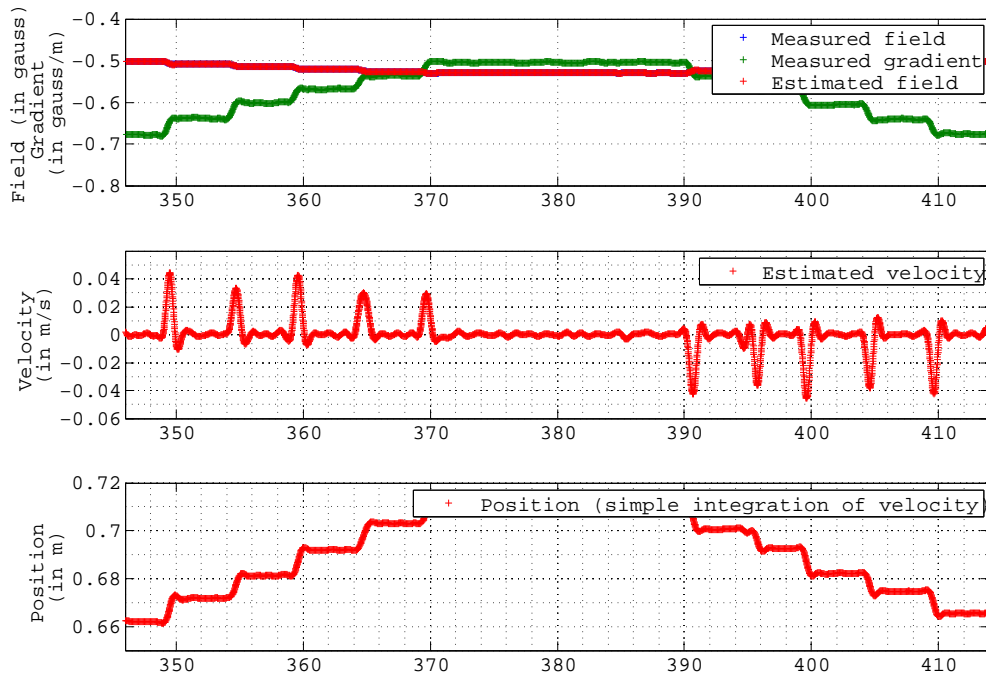


Figure 5.2: Experimental results. The platform is translated step by step in direction sensors are lined up. One step of 1 cm is made every 5 s, first forwards then backwards, after a rest of 20 s.

forth along a simple straight path in front of a reference laser telemeter. This allows to precisely evaluate the representativeness of the velocity estimate, and of the subsequent relative position reconstruction. The corresponding data are represented in Figure (5.3).

One can clearly see the very good quality of the velocity estimate, which, in particular, kindly reproduces the sharp accelerations. The position obtained by integration of the estimated velocity match the one provided by the laser telemeter with a precision of a few percents.

5.3.2 3-dimensional experiments in various urban environments

The previous 1-dimensional experiments against known, accessible and accurate references have validated that the velocity estimation is rather accurate, and that the subsequent relative position obtained by integration is relevant. Figure 5.4 where a pedestrian goes some stairs up two levels in an office building, stresses that the MINAV system can also provide interesting 3-dimensional trajectories reconstruction. Generally, getting accurate references for 3-dimensional in-the-field experiments is not as easy as in the 1-dimensional case in laboratory. Nonetheless, two types of reference can be used to evaluate the accuracy of the reconstructed position. Maps, when available, provide a first reference all along the

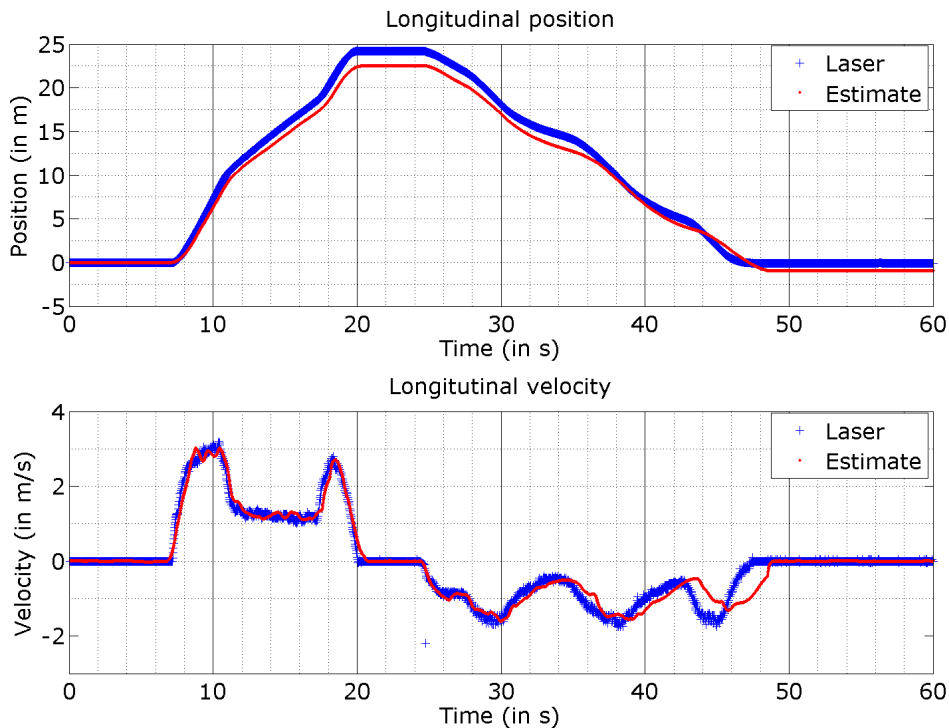


Figure 5.3: Experimental results - Velocity (and integrated position) in a long straight corridor. The estimated velocity (and position) are compared against a laser telemeter.

trajectory. Loop-shaped trajectories, on the other hand, can be used to evaluate the error after a certain time. When the trajectory comes back to its starting point, a “closure error” can be measured as the distance between the starting point and the end point. For every 3-dimensional trajectory presented now onward, at least one of these two references is available.

Depending on the type of buildings (e.g. freestone buildings, prefabs, traditional reinforced concrete buildings) and their usage (e.g. family housing, offices, buildings open to the public like supermarkets), one could have assumed they would present a more or less suitable ground for MINAV. Experiments reveals that magnetic disturbances are strong enough in all those buildings to allow the use of the “magnetic pedometer” described earlier. Figure 5.5 reports results obtained outdoors, close to buildings. The path is performed between the streets Auguste Comte and Michelet in Paris, France.

Figure 5.6 reports indoor results obtained around the main lecture hall at (Amphitheatre Poincaré) at MINES ParisTech, France.

Figure 5.7 reports experimental indoor results obtained in a long corridor (round trips) with intermediate path in an open space. The experiment was conducted in the tower “Tour de l’Horloge” above Gare de Lyon train station in Paris.

Figure 5.8 reports experiments conducted at EADS Cassidian main offices in Élancourt during a project review meeting of Locindoor project.

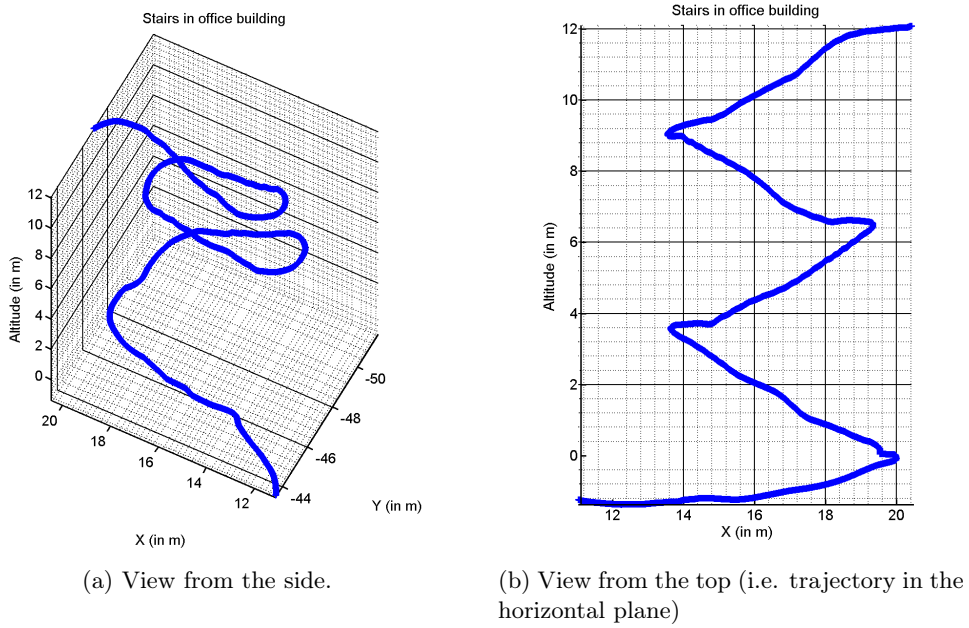


Figure 5.4: Experimental result. Pedestrian walking stairs two levels up in an office building.

Finally, Figure 5.9 reports results obtained in the CNIT building at La Défense. It is a high ceiling building with large open spaces and more narrow corridors and halls.

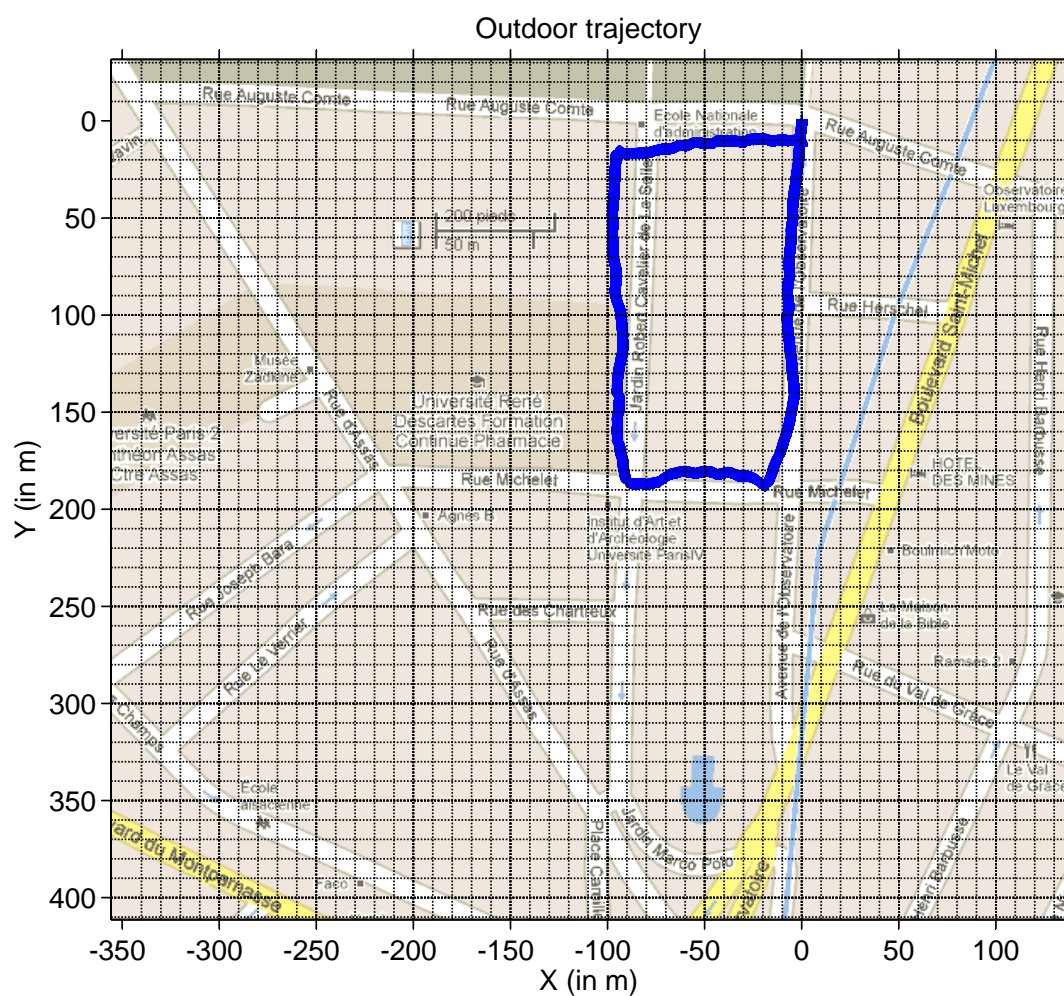


Figure 5.5: Experimental results in streets. Closed-path between the streets Auguste Comte and Michelet in Paris, France.

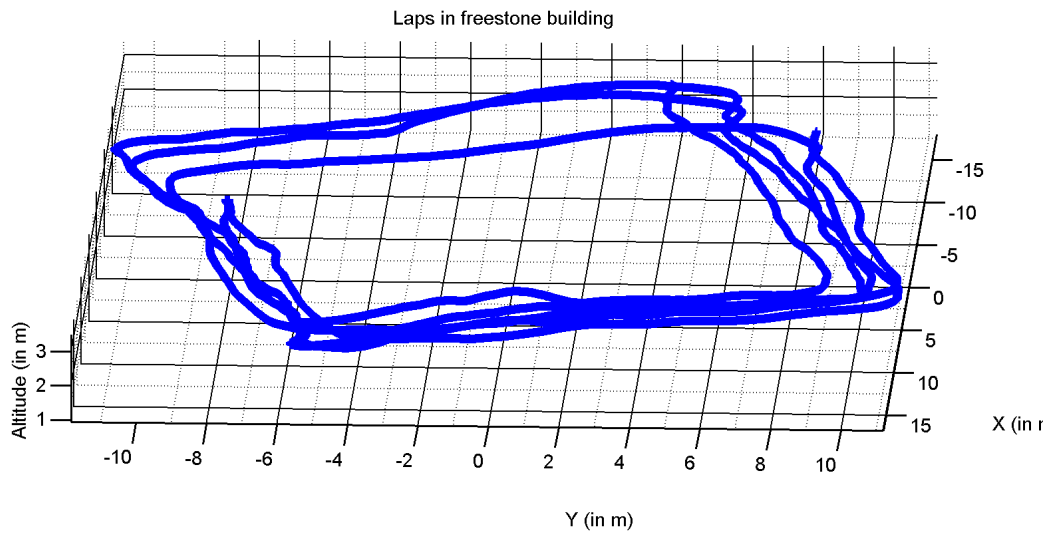


Figure 5.6: Experimental results in a freestone building (MINES ParisTech, 60 Bd S^t Michel, Paris). Distance: 373 m. Final error: 9.5 m

Starting in (0,0), the pedestrian walks about 2.5 laps in a loop-shaped corridor, then turns backs and gets back to (0,0) after about 1.5 laps and stops.

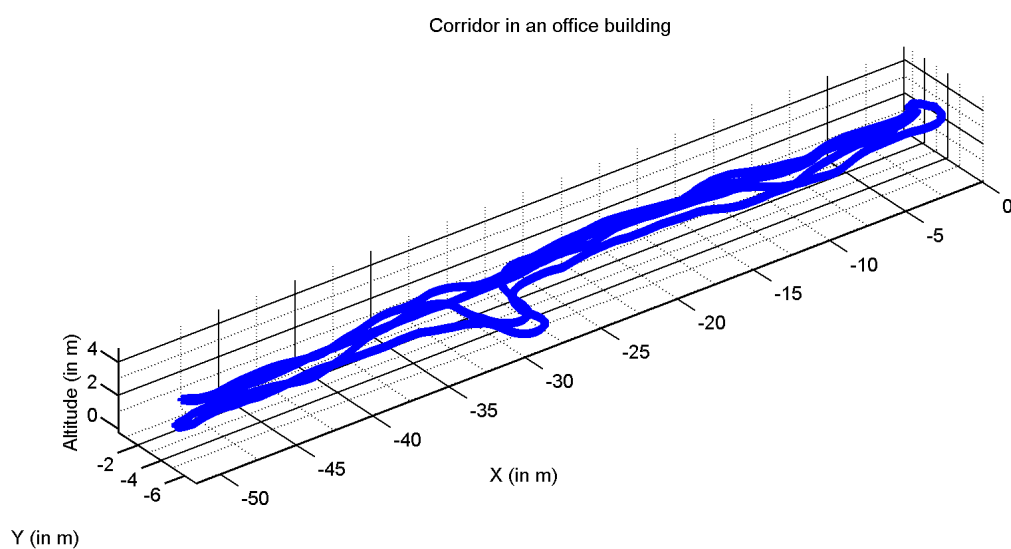


Figure 5.7: Experimental results in a prefab corridor at the Tour de l'Horloge above Gare de Lyon train station, in Paris, France. Distance: 217 m. Final error: 10 m
The pedestrian walks two round-trips in a corridor. During one of these round-trips, a small excursion in small open-space is made on both ways.

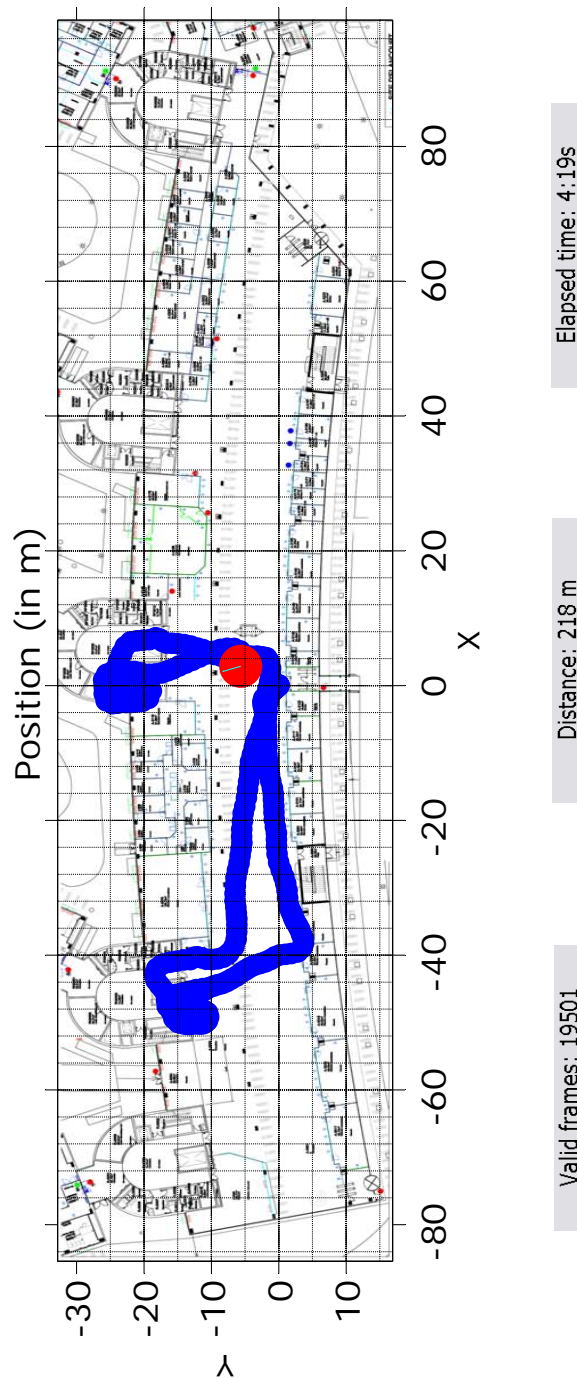


Figure 5.8: Experimental results in a modern traditional office building with reinforced concrete in Élancourt, France. Final error: 7 m.

Starting from (0,0), the pedestrian walks through the huge open-space to (-40,-8). Then he climbs the stairs one level up and crosses above the open-space to (3,40). Afterwards, he goes along the offices. When he is above the starting point, he crosses again above the open-space, goes the stairs one level down, and crosses once again the open-space to stop at the starting point.

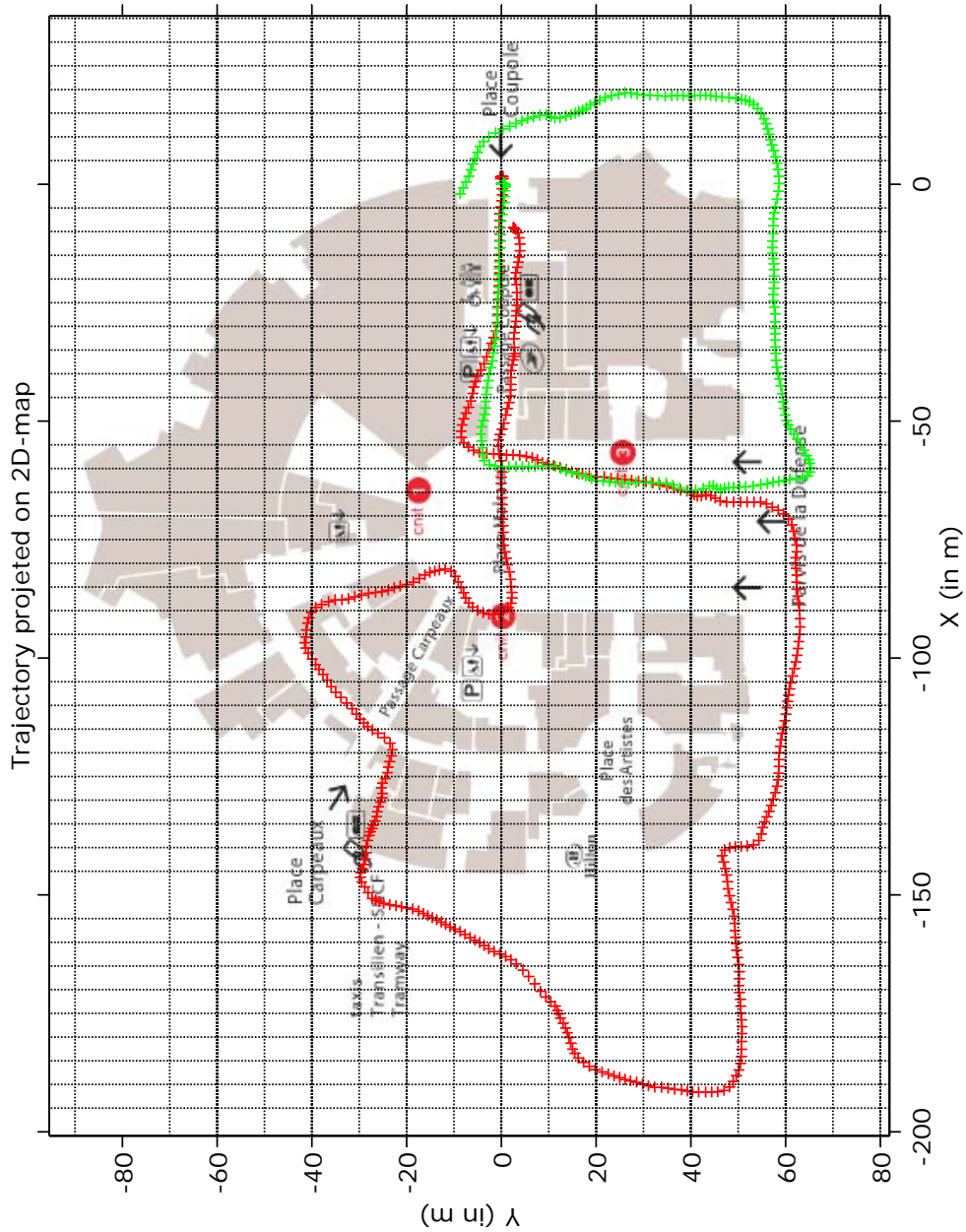


Figure 5.9: Experimental results inside and outside a shopping mall, the CNIT building in La Defense, France. The two trajectories (red and green) start in (0,0) at the entrance of the building, follow the first corridor, turn left and exit the building. The green trajectory turns left again and joins the starting entrance by the outside. The red trajectory goes in the opposite direction to find another entrance of the building and gets back to the starting point by crossing the entire building.

Appendix A

Unbiased calibration problem of a single sensor in 2-dimensions

Problème de la calibration d'un capteur non-biaisé en 2 dimensions

The propositions presented in Section 4.2 provide theoretical insight into the progression of the algorithm along the iterations: the data are better and better calibrated (Proposition 4), and make few progress in rotation (Proposition 5). It is in fact possible to go a bit further in the analysis. Let us now focus on a specific 2-dimensional case (i. e. where the measurements are performed in 2 dimensions), and further, let us make the following notational simplifying assumptions. We consider that the measurements constitute a closed and centered ellipse (i.e. that there is a continuum of data, and that a preliminary debiasing has been performed). The measurements are noted $y(\theta)$, $\theta \in [0, 2\pi[$, and the iteratively calibrated data are $y_k(\theta)$, $\theta \in [0, 2\pi[$. Then, we assume that no misalignment is present and consider only scale factors. Therefore, the measurements satisfy

$$Y(\theta) = Ay(\theta)$$

where A is an unknown diagonal matrix. By analogy to equation (4.4), the cost to be minimized at iteration k is

$$h(A, k) = \int_0^{2\pi} \left\| Ay_k(\theta) - \frac{y_k(\theta)}{\|y_k(\theta)\|} \right\|^2 d\theta$$

Note A_{k+1} the solution of this minimization problem, i.e.

$$A_{k+1} = \arg \min_{A \text{ diagonal}} h(A, k)$$

Iteratively, the data are calibrated using $y_{k+1}(\theta) = A_{k+1}y_k(\theta)$. At step k , let us note the inverse calibration equation

$$y_k(\theta) = \begin{pmatrix} \alpha_k & 0 \\ 0 & \beta_k \end{pmatrix} Y(\theta)$$

With the notation

$$f(y_k) = \int_0^{2\pi} \left| 1 - \|y_k(\theta)\|^2 \right| d\theta$$

a reasoning similar to the one in the proof of Proposition 5 directly yields

$$f(y_k) \geq h(A_{k+1}, k) \geq f(y_{k+1})$$

Further,

$$\begin{aligned} f(y_k) &= 2\pi \left(1 + \frac{\alpha_k^2}{2} + \frac{\beta_k^2}{2} \right) - 2 \int_0^{2\pi} \|y(\theta)\| d\theta \\ &= 2\pi \left(1 + \frac{\alpha_k^2}{2} + \frac{\beta_k^2}{2} \right) - 2P(\alpha, \beta) \end{aligned} \quad (\text{A.1})$$

where $P(\alpha, \beta)$ is the perimeter of an ellipse having $1/\alpha_k$ and $1/\beta_k$ as semi-axis. We wish to show that the inverse calibration matrix $\begin{pmatrix} \alpha_k & 0 \\ 0 & \beta_k \end{pmatrix}$ tends to the identity as k tends to infinity, i.e. that the proposed algorithm converges to exact calibration of the data. Similarly to Proposition 4, one can readily show that f decreases along the iterations and goes to a limit $\ell \geq 0$. Using an estimate for (A.1), it is possible to deduce convergence information on α_k and β_k . To simplify the exposition, let us first consider that this limit is $\ell = 0$.

Consider in equation (A.1), f as a function of (α_k, β_k) . It can be proved that f has $(1, 1)$ as unique local minimum (in a rather large neighborhood) and that its value there is 0. To prove that, one can simply use Peano's approximation of the perimeter of an ellipse [8] reproduced in Equation (A.2). This approximation is always over-estimating the true value.

$$P(\alpha, \beta) \approx \pi \left(\frac{3}{2} (\alpha + \beta) - \sqrt{\alpha\beta} \right) \quad (\text{A.2})$$

Accounting for the approximation implied by this formula, one can compute the following exact decomposition of f under the form

$$f(\alpha_k, \beta_k) = f_1(\alpha_k, \beta_k) + f_2(\alpha_k, \beta_k)$$

where

$$f_1(\alpha, \beta) = 2\pi \left(1 + \frac{\alpha^2}{2} + \frac{\beta^2}{2} \right) - 2\pi \left(\frac{3}{2} (\alpha + \beta) - \sqrt{\alpha\beta} \right) \quad (\text{A.3})$$

and where $f_2(\alpha_k, \beta_k)$ is strictly positive away from $\alpha_k = \beta_k$ and zero there. f_1 , given in (A.3), is convex on the considered domain $[3/4, 4/3]^2$ (its Hessian is given in (A.4)), is strictly positive away from $(1, 1)$ and zero there. Therefore, $(1, 1)$ is the only zeroing point of f , and one can conclude that (α_k, β_k) converges to $(1, 1)$. This estimate reveals handy in experimental results where ℓ can be evaluated numerically.

$$\frac{\nabla^2 f_1(\alpha, \beta)}{2\pi} = \begin{pmatrix} 1 - \frac{\beta}{4\alpha\sqrt{\alpha\beta}} & \frac{1}{4\sqrt{\alpha\beta}} \\ \frac{1}{4\sqrt{\alpha\beta}} & 1 - \frac{\alpha}{4\beta\sqrt{\alpha\beta}} \end{pmatrix} \quad (\text{A.4})$$

Now, let us extend the analysis to the case $\ell > 0$. A local expansion of f for (α, β) about $(1, 1)$ yields the following inequalities

$$\frac{\begin{pmatrix} \alpha - 1 & \beta - 1 \end{pmatrix} \begin{pmatrix} 3 & 1 \\ 1 & 3 \end{pmatrix} \begin{pmatrix} \alpha - 1 \\ \beta - 1 \end{pmatrix}}{16} \leq \ell \leq \frac{\begin{pmatrix} \alpha - 1 & \beta - 1 \end{pmatrix} \begin{pmatrix} 3 & 1 \\ 1 & 3 \end{pmatrix} \begin{pmatrix} \alpha - 1 \\ \beta - 1 \end{pmatrix}}{4}$$

and we deduce the estimation, where d is the distance of (α, β) to $(1, 1)$,

$$\frac{\sqrt{2}}{4}d \leq \sqrt{\ell} \leq d$$

meaning that both α_k and β_k approach 1 as the square root of ℓ approaches 0.

Appendix B

A technical result

Un résultat technique

To minimize the convex function (4.15), its derivative is required. The following lemma is useful.

Lemma 1: Denote $y \in \mathbb{R}^m$, $x \in \mathbb{R}^n$ and $S \in \mathbb{S}_n(\mathbb{R})$ a skew symmetric matrix. Define $f : M \in \mathbb{M}_{m,n}(\mathbb{R}) \rightarrow \|y - SMx\|^2$. Then, f is differentiable and its derivative is

$$Df(M) = \left[\frac{\partial f}{\partial M_{i,j}} \right]_{\substack{i=1..m \\ j=1..n}} = -2 \cdot S(y - SMx)x^T$$

□

Proof: First, one shall expand the expression of f ,

$$\begin{aligned} f(M) &= \sum_i \left(y_i - \sum_{j,k} S_{i,j} M_{j,k} x_k \right) \left(y_i - \sum_{p,q} S_{i,p} M_{p,q} x_q \right) \\ &= \sum_i y_i^2 - 2 \cdot \sum_{i,j,k} y_i S_{i,j} M_{j,k} x_k + \sum_{i,j,k,p,q} x_k^T M_{j,k} S_{i,j} S_{i,p} M_{p,q} x_q \end{aligned}$$

Then, for any $(u, v) \in [1, m] \times [1, n]$, the derivative of $f(M)$ with respect to any component $M_{u,v}$ is

$$\frac{\partial f}{\partial M_{u,v}}(M) = -2 \cdot \sum_i y_i S_{i,u} x_v + \sum_{i,p,q} x_v S_{i,u} S_{i,p} M_{p,q} x_q + \sum_{i,j,k} x_k M_{j,k} S_{i,j} S_{i,u} x_v$$

Because S is skew symmetric,

$$\begin{aligned} \frac{\partial f}{\partial M_{u,v}}(M) &= -2 \cdot \left(\sum_i S_{u,i} y_i \right) x_v + 2 \left(\sum_{i,p,q} S_{u,i} S_{i,p} M_{p,q} x_q \right) x_v \\ &= -2 \cdot (Sy)_u x_v + 2 \cdot (S^2 Mx)_u x_v \\ &= -2 \cdot (S(y - SMx))_u x_v \end{aligned}$$

which yields

$$D_f(M) = \left[\frac{\partial f}{\partial M_{u,v}} \right]_{u=1..m, v=1..n} - 2 \cdot S(y - SMx) x^T$$

$J(\tilde{A}, \tilde{B})$ is a convex and differentiable function. It thus reaches its minimum when its derivative is zero. As $(P_\gamma)_k$ is an orthogonal projector, its matrix is skew symmetric. Lemma 1 applies, leading to ■

$$0 = -2 \cdot \sum_{k=1}^K (P_\gamma)_k (Y_k - (P_\gamma)_k [Ab] X_k) (X_k)^T$$

and, thus

$$\sum_{k=1}^K Y_k (X_k)^T = \sum_{k=1}^K (P_\gamma)_k [Ab] X_k X_k^T \quad (\text{B.1})$$

Using the canonical base $(E_i)_{i=1..12}$ of $\mathbb{M}_{3,4}(\mathbb{R})$ defined in Lemma 2, and writing $[A \ b]$ under the form

$$[A \ b] = \begin{pmatrix} m_1 & m_4 & m_7 & m_{10} \\ m_2 & m_5 & m_8 & m_{11} \\ m_3 & m_6 & m_9 & m_{12} \end{pmatrix} = \sum_{j=1}^{12} m_j E_j$$

The relation (B.1) can be rewritten as

$$\underbrace{\sum_{k=1}^K Y_k X_k^T}_{\sum_{i=1}^{12} y_i E_i} = \sum_{j=1}^{12} m_j \cdot \underbrace{\left(\sum_{k=1}^K (P_\gamma)_k E_j X_k X_k^T \right)}_{\sum_{i=1}^{12} x_{i,j} E_i}$$

This yields

$$y_i = \sum_{j=1}^{12} x_{i,j} m_j \quad , \quad \forall i = 1..12$$

$$\mathbb{Y} = \mathbb{X} \begin{pmatrix} m_1 & m_2 & \dots & m_{12} \end{pmatrix}^T$$

Under the assumption that \mathbb{X} is invertible, one obtains

$$\begin{pmatrix} m_1 & m_2 & \dots & m_{12} \end{pmatrix}^T = \mathbb{X}^{-1} \mathbb{Y}$$

which concludes the proof.

Appendix C

Proof of convergence in the linear time varying case

Preuve de convergence dans le cas linéaire avec dépendance en temps

In Section 2.2, we consider a linear time-varying system whose dynamics is given by Equation (2.10). These equations are of the form studied below, with $J = \frac{\partial(B)_b}{\partial \mathcal{B}_b}$.

Consider the LTV error dynamics with state $(\tilde{B}, \tilde{V})^T \in \mathbb{R}^6$

$$\dot{\tilde{X}} = \begin{pmatrix} -\Omega(t) - l_1 J(t)J(t)^T & J(t) \\ -l_2 J(t)^T & -\Omega(t) \end{pmatrix} \tilde{X} = \tilde{A}(t)\tilde{X} \quad (\text{C.1})$$

With $l_1 > 0$, $l_2 > 0$, we know that $W(\tilde{X}) = \frac{1}{2} \|\tilde{B}\|^2 + \frac{1}{2l_2} \|\tilde{V}\|^2$ is such that

$$\dot{W} = -l_1 \tilde{B}^T J(t)J(t)^T \tilde{B} = -l_1 \tilde{X}^T \tilde{C}^T(t)\tilde{C}(t)\tilde{X}$$

with $\tilde{C} = [J(t)^T 0]$.

It is known (see [69, ex. 8.11]), that the global exponential stability of this LTV error dynamics with state \tilde{X} is guaranteed under the assumption of Uniform Observability (UO) of the pair (\tilde{A}, \tilde{C}) .

As has been shown in [19, thm4], Differential Observability (DO) implies Uniform Complete Observability (UCO) which implies UO. Therefore, we now investigate the DO property of the pair (\tilde{A}, \tilde{C}) .

For this, we consider the matrix $[Q_0(t), Q_1(t), \dots, Q_n(t)]$ composed using

$$Q_0(t) = \tilde{C}(t)^T, \quad Q_{i+1}(t) = \dot{Q}_i(t) + \tilde{A}(t)^T Q_i(t)$$

The DO property holds if $\sum_{i=0}^m Q_i(t)Q_i(t)^T \geq \mu I > 0$ for some $\mu > 0$, some $m \in \mathbb{N}$. As will be shown, this property holds for $m = 1$.

Consider $Q_0(t) = \tilde{C}(t)^T = \begin{pmatrix} J(t) \\ 0 \end{pmatrix}$, and $Q_1(t) = \begin{pmatrix} \dot{J}(t) + \Omega J - l_1 J(t) J(t)^T J(t) \\ J(t)^T J(t) \end{pmatrix}$.

Finally, constitute

$$Q_o = [Q_0(t)Q_1(t)] = \begin{pmatrix} J(t) & \dot{J}(t) + \Omega J - l_1 J(t) J(t)^T J(t) \\ 0 & J(t)^T J(t) \end{pmatrix} \quad (\text{C.2})$$

We now wish to establish that this matrix is such that

$$Q_o(t)Q_o(t)^T \geq \mu I > 0$$

for some $\mu > 0$ to be determined.

$Q_o(t)$ is of the triangular form

$$\begin{pmatrix} M(t) & B(t) \\ 0 & N(t) \end{pmatrix} \quad (\text{C.3})$$

for which we have the following result, where we note here $\|A\|_\infty = \max_{1 \leq i \leq n} \sum_{j=1}^n |a_{ij}|$ the max row sum norm.

Lemma 2: Consider a $2n \times 2n$ matrix $P(t)$ of the form (C.3) where $M(t)^T M(t) \geq \mu_1 I$, $N(t)^T N(t) \geq \mu_2 I$, $\|B(t)\|_\infty \leq \gamma$, then the lowest singular value of $P(t)$ is uniformly lower-bounded by $\sqrt{\mu}$ with

$$\mu = \left(\max \left(\frac{1}{\mu_1}, \frac{1}{\mu_2} \right) + \gamma \frac{n^{3/2}}{\mu_1 \mu_2} (\sqrt{\mu_1} + \gamma \sqrt{n}) \right)^{-1}$$

□

Proof: The largest singular value of P equals $\|P\|_2$. The singular values of P^{-1} are the inverse of the singular values of P . Then, one has

$$\|P\|_2 \geq \frac{1}{\|P^{-1}\|_2}$$

The inverse P^{-1} is

$$\begin{pmatrix} M(t)^{-1} & -M(t)^{-1}B(t)N(t)^{-1} \\ 0 & N(t)^{-1} \end{pmatrix}$$

Then, $\|P^{-1}\|_2$ can be upper-bounded as follows

$$\|P^{-1}\|_2^2 = \max_{\|x\|=1, x \in \mathbb{R}^6} x^T P^{-1}(t) P^{-T}(t) x \quad (\text{C.4})$$

Noting that

$$P^{-1}(t)P^{-T}(t) = \begin{pmatrix} M^{-1}M^{-T} + M^{-1}BN^{-1}N^{-T}B^T M^{-T} & -M^{-1}BN^{-1}N^{-T} \\ -N^{-1}N^{-T}B^T M^{-T} & N^{-1}N^{-T} \end{pmatrix}$$

Then, one has

$$x^T P^{-1}(t) P^{-T}(t) x = x^T \begin{pmatrix} M^{-1} M^{-T} & 0 \\ 0 & N^{-1} N^{-T} \end{pmatrix} x \\ + x^T \begin{pmatrix} M^{-1} B N^{-1} N^{-T} B^T M^{-T} & -M^{-1} B N^{-1} N^{-T} \\ -N^{-1} N^{-T} B^T M^{-T} & 0 \end{pmatrix} x$$

We now wish to consider this value for $\|x\| = 1$, to evaluate the sought after norm. Remembering that, by assumption¹

$$\|M^{-1}\|_2 \leq \frac{1}{\sqrt{\mu_1}}, \quad \|N^{-1}\|_2 \leq \frac{1}{\sqrt{\mu_2}}$$

and that for every $n \times n$ matrix G , one has

$$\|G\|_\infty \leq \sqrt{n} \|G\|_2$$

which gives $\|M^{-1}\|_\infty < \sqrt{\frac{n}{\mu_1}}$, $\|N^{-1}\|_\infty < \sqrt{\frac{n}{\mu_2}}$. Further, the $\|\cdot\|_\infty$ norm is consistent because it is a subordinate matrix norm (see [56, p.327]), i.e. $\|AB\|_\infty \leq \|A\|_\infty \|B\|_\infty$, for all matrices A and B . Besides, for all matrix M , for all $\|x\| = 1$, one has $x^T M x \leq \|M\|_\infty$. Finally, for all matrices A, B, C, D , one has

$$\left\| \begin{pmatrix} A & B \\ C & D \end{pmatrix} \right\|_\infty \leq \max(\|A\|_\infty + \|B\|_\infty, \|C\|_\infty + \|D\|_\infty)$$

Then, one obtains

$$\|P^{-1}\|_2^2 \leq \max\left(\frac{1}{\mu_1}, \frac{1}{\mu_2}\right) + \gamma \frac{n^{3/2}}{\mu_1 \mu_2} (\sqrt{\mu_1} + \gamma \sqrt{n})$$

■

From this lemma, we can now formulate the main result

Lemma 3: Consider $l_1 > 0$, $l_2 > 0$, and assume that $J(t)$ is such that there exists μ_1, γ_1 such that for all t , $J(t)^T J(t) \geq \mu_1 I$, $\|J(t)\|_\infty \leq \gamma_1$, $\|\dot{J}(t)\|_\infty \leq \gamma'_1$ and that $\Omega(t)$ is such that $\|\Omega(t)\|_\infty \leq \gamma_2$ for all t , then there exist $\mu > 0$ such that

$$Q_o(t) Q_o(t)^T \geq \mu I > 0$$

This shows that the pair (\tilde{A}, \tilde{C}) is DO, then it is UCO, then it is UO. Then, the error dynamics (C.1) is globally exponentially stable. □

Proof: The assumption that l_1 and l_2 are positive are required for W to be a Lyapunov function. We know from (C.2) that Lemma 2 applies with $\mu_1, \mu_2 = \mu_1^2, \gamma = \gamma'_1 + \gamma_1(\gamma_2 + l_1 \gamma_1^2)$, which gives the sought-after μ . ■

¹ $\frac{1}{\|M^{-1}(t)\|_2}$ is the smallest singular value of $M(t)$. Thus, there exists a vector $Z(t)$ such that $Z(t)^T M(t)^T M(t) Z(t) = \frac{1}{\|M^{-1}(t)\|_2^2}$. Following the hypothesis of the lemma, one thus has $\frac{1}{\|M^{-1}(t)\|_2^2} \geq \mu_1$.

Appendix D

Observability of accelerometer biases

Observabilité des biais des accéléromètres

As mentioned in Section 1.3, in low-cost inertial navigation, accelerometers drifts are a major source of error. Monitoring the variations of the magnetic field and its Jacobian is however a powerful tool that makes accelerometers biases observable, reducing greatly the drifts in low-cost inertial systems. We adopt here the same notations as in Chapter 2, noting B the vector magnetic field and $(B_x \ B_y \ B_z)^T$, X the position of the rigid body in \mathcal{R}_i , $V = \frac{dX}{dt}|_{\mathcal{R}_i}$ the velocity of the rigid body in the \mathcal{R}_i reference frame, and $\Omega_{b/i}$ the vector rotation of \mathcal{R}_b with respect to the \mathcal{R}_i reference frame. Denote $(B_x \ B_y \ B_z)^T$, $(u \ v \ w)^T$, and $(p \ q \ r)^T$ the respective projections of B , V , and $\Omega_{b/i}$ onto the \mathcal{R}_b reference frame.

From Chapter 2, one has the following dynamics for the magnetic field and the velocity

$$\left. \frac{dB}{dt} \right|_{\mathcal{R}_b} = -\Omega_{b/i} \wedge B + \frac{\partial B}{\partial X} V \quad (2.5)$$

$$\dot{V} = -\Omega_{b/i} \times V + F_m \quad (2.7)$$

Since accelerometers readings are available, the total forces per unit of mass F_m can be split in two parts, the specific acceleration Γ and the gravity g .

$$\dot{V} = -\Omega_{b/i} \times V + \Gamma + g$$

Once projected onto \mathcal{R}_b , it yields

$$\frac{d}{dt} \begin{pmatrix} u \\ v \\ w \end{pmatrix} = - \begin{pmatrix} p \\ q \\ r \end{pmatrix} \times \begin{pmatrix} u \\ v \\ w \end{pmatrix} + \begin{pmatrix} \Gamma_x \\ \Gamma_y \\ \Gamma_z \end{pmatrix} + \begin{pmatrix} g_x \\ g_y \\ g_z \end{pmatrix}$$

where $(\Gamma_x \ \Gamma_y \ \Gamma_z)^T$ and $(g_x \ g_y \ g_z)^T$ are the projection of Γ and g respectively onto the \mathcal{R}_b reference frame. $(\Gamma_x \ \Gamma_y \ \Gamma_z)^T$ corresponds to the measurements of the accelerometers attached to the rigid body. We note $(b_{\Gamma_x} \ b_{\Gamma_y} \ b_{\Gamma_z})^T$ the biases of these accelerometers.

The system writes in the state-space form

$$\begin{aligned} \frac{d}{dt} \begin{pmatrix} B_x \\ B_y \\ B_z \end{pmatrix} &= - \begin{pmatrix} p \\ q \\ r \end{pmatrix} \times \begin{pmatrix} B_x \\ B_y \\ B_z \end{pmatrix} + \left(\frac{\partial (B)_b}{\partial \mathcal{B}_b} \right) \begin{pmatrix} u \\ v \\ w \end{pmatrix} \\ \frac{d}{dt} \begin{pmatrix} u \\ v \\ w \end{pmatrix} &= - \begin{pmatrix} p \\ q \\ r \end{pmatrix} \times \begin{pmatrix} u \\ v \\ w \end{pmatrix} + \begin{pmatrix} \Gamma_x \\ \Gamma_y \\ \Gamma_z \end{pmatrix} + \begin{pmatrix} g_x \\ g_y \\ g_z \end{pmatrix} \\ \frac{d}{dt} \begin{pmatrix} \Gamma_x \\ \Gamma_y \\ \Gamma_z \end{pmatrix} &= 0 \\ \frac{d}{dt} \begin{pmatrix} b_{\Gamma_x} \\ b_{\Gamma_y} \\ b_{\Gamma_z} \end{pmatrix} &= 0 \\ y_B &= \begin{pmatrix} B_x \\ B_y \\ B_z \end{pmatrix} \\ y_\Gamma &= \begin{pmatrix} \Gamma_x \\ \Gamma_y \\ \Gamma_z \end{pmatrix} + \begin{pmatrix} b_{\Gamma_x} \\ b_{\Gamma_y} \\ b_{\Gamma_z} \end{pmatrix} \end{aligned}$$

The matrix of the dynamics A and the measurement matrix C of the system are thus.

$$\begin{aligned} A &= \begin{pmatrix} -[(\Omega)_b] & \left(\frac{\partial (B)_b}{\partial \mathcal{B}_b} \right) & 0_3 & 0_3 \\ -[(\Omega)_b] & 0_3 & I_3 & 0_3 \\ 0_3 & 0_3 & 0_3 & 0_3 \\ 0_3 & 0_3 & 0_3 & 0_3 \end{pmatrix} \\ C &= \begin{pmatrix} I_3 & 0_3 & 0_3 & 0_3 \\ 0_3 & 0_3 & I_3 & I_3 \end{pmatrix} \end{aligned}$$

where $[(\Omega)_b]$ is the matrix corresponding to the left-hand-side cross product by $\begin{pmatrix} p & q & r \end{pmatrix}^T$ (see Equation (2.9)).

It yields the following observability matrix \mathcal{O}

$$\mathcal{O} = \begin{pmatrix} I_3 & 0_3 & 0_3 & 0_3 \\ 0_3 & 0_3 & I_3 & I_3 \\ -[(\Omega)_b] & \left(\frac{\partial(B)_b}{\partial \mathcal{B}_b}\right) & 0_3 & 0_3 \\ 0_3 & 0_3 & 0_3 & 0_3 \\ [(\Omega)_b]^2 - \left(\frac{\partial(B)_b}{\partial \mathcal{B}_b}\right) [(\Omega)_b] & -\left(\frac{\partial(B)_b}{\partial \mathcal{B}_b}\right) [(\Omega)_b] & \left(\frac{\partial(B)_b}{\partial \mathcal{B}_b}\right) & 0_3 \\ 0_3 & 0_3 & 0_3 & 0_3 \\ \vdots & \vdots & \vdots & \vdots \end{pmatrix}$$

Provided that $\left(\frac{\partial(B)_b}{\partial \mathcal{B}_b}\right)$ has full rank, i.e. that the vector field is sufficiently non-uniform, the observability matrix \mathcal{O} has rank 12 because the block lines 1,2,3 and 5 are independent. The state is thus fully observable. In particular, the accelerometer biases are observable.

Appendix E

More on sensor set calibration

Compléments sur la calibration d'un jeu de capteurs

In this appendix, we consider a set of two 3-axis sensors (here magnetometers) to be calibrated, and expose two calibration methods. The methods discussed here can easily be extended to a wider array of sensors. The aim is to generalize the previously exposed (see Section 4.2) simple but effective on-the-field calibration procedure used for a single sensor to an array of sensors.

The calibration of the sensor array consists in determining calibration parameters (a matrix and a vector) for each sensor, such that, once these parameters are used as compensations,

- each sensor considered separately is well calibrated, i.e. its norm is constant if it is rotated in a constant field,
- and all the sensors have the same output when they are put at the same location, i.e. their measurements should have the same norm and the same orientation.

E.1 Method 1: first sensor taken as reference

This method proceeds in two steps. First, one of the two magnetometers is calibrated as a single sensor (following, e.g. one of the methods presented in Section 4.2. Note A_1 and B_1 its calibration parameters. Then, the second magnetometer is calibrated using the newly calibrated measurements from the first sensor as references. The sought-after calibration parameters are noted A_2 and B_2 . This second step is performed by minimizing the following cost function

$$f_1(A_2, B_2) = \sum_{i=1}^N \|A_2 y_2(i) + B_2 - (A_1 y_1(i) + B_1)\|^2$$

This is a classical least-squares problem which, despite the large number N of data, can be solved easily and promptly. The first table-free calibration is run only once for the sensor taken as reference (resulting in the parameters A_1 and B_1). Then, a simple least-square algorithm is used for the second sensor. In the general case of an array of sensors, the least square-algorithm is run once for each sensor of the array.

E.2 Method 2: two independent calibrations followed by an harmonization step

Another method is as follows. First, both sensors are calibrated separately. Then, an harmonization step is performed so that both frames of coordinates have the same orientation. In other words, a rotation matrix relating the measurements from the calibrated sensors is calculated. In this last step, the function to minimize is detailed below in Equation (E.1). O_{12} is the sought after rotation matrix, whereas A_1 , B_1 , A_2 and B_2 are the calibration parameters preliminarily obtained.

$$f_2(O_{12}) = \sum_{i=1}^N \|O_{12}(A_2 y_2(i) + B_2) - (A_1 y_1(i) + B_1)\|^2 \quad (\text{E.1})$$

E.3 Impact of experimental inaccuracies

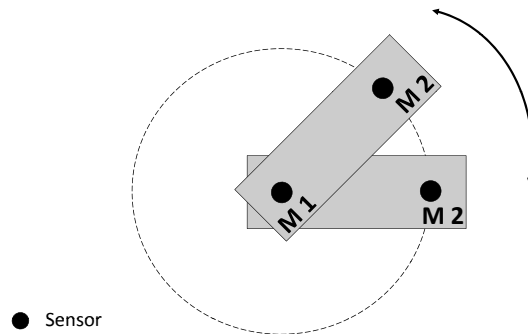


Figure E.1: When calibrating two sensors, rotations are performed around one of the sensor, while the other one is moving on a sphere (around the first sensor). The gradient of the sensed field has thus an impact on the measurements of the second sensor.

The previous presented methods give good results in theory. Yet, several practical issues must be considered. In particular, in view of actual on-the-field magnetometers calibration which may be performed in slightly (or worse) magnetically perturbed areas, it is important to determine whether these disturbances will significantly impact on the calibration results. We now investigate the impact of a non-zero magnetic gradient being at the place the calibration measurements are performed. For sake of simplicity, we consider that two 3-axis magnetometers are used. Except when explicitly mentioned, we assume, without any loss of generality, that the sensor 3-dimensional rotations are made around the first magnetometer, as pictured in Figure E.1. This magnetometer is rotated strictly around a fixed point. Therefore, it senses the exact same field during the rotations. By contrast, magnetometer 2, which is attached on the same board as magnetometer 1, is moving on a sphere centered on magnetometer 1. For this reason, magnetometer 2 does not measure the exact same field during the calibration experiment because of the presence of the field gradient.

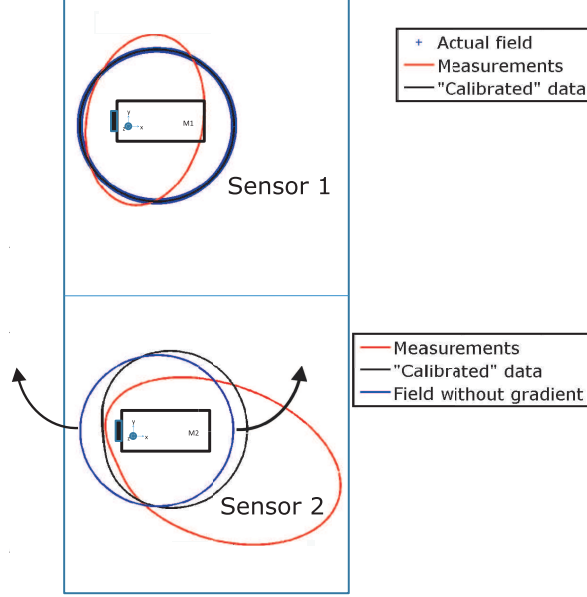


Figure E.2: Measurements and calibrated data for the two magnetometers. Sensor 1 is placed at the center of rotation whereas sensor 2 is rotated around sensor 1. Due to the nature of the center of rotation during the calibration, sensor 1 is well-calibrated while sensor 2 remains slightly ill-calibrated.

E.3.1 Method 1

As previously discussed, both sensors do not measure the exact same value of the field when its gradient is not zero. Consider $x_1(i)$ and $x_2(i)$ the (three dimensional) location of the sensors where the i^{th} measurement is performed. According to the discussed calibration procedure, x_1 is constant while x_2 is moving on a sphere. Note the vector

$$\delta_{12}(i) = x_2(i) - x_1(i)$$

and the radius $\delta = \|\delta_{12}(i)\|$.

Note H the (vector) sensed field which is not spatially constant. We have

$$H(x_1(i)) = H(x_2(i) - \delta_{12}(i)) = H(x_2(i)) - \frac{\partial H}{\partial X} \delta_{12}(i) + o(\delta^2)$$

The cost function to be minimized can be rewritten as follows

$$\begin{aligned}
 f_1(A_2, B_2) &= \sum_{i=1}^N \|A_2 y_2(i) + B_2 - H(x_1(i))\|^2 \\
 &= \sum_{i=1}^N \left\| A_2 y_2(i) + B_2 - H(x_2(i)) + \frac{\partial H}{\partial X} \delta_{12}(i) \right\|^2 + o(\delta^2) \\
 &= \sum_{i=1}^N \|A_2 y_2(i) + B_2 - H(x_2(i)) + \epsilon_{12}(i)\|^2
 \end{aligned} \tag{E.2}$$

with

$$\epsilon_{12}(i) = \frac{\partial H}{\partial X} \delta_{12}(i) + o(\delta)$$

Let us note (A_2^*, B_2^*) the parameters minimizing f_1 when δ is zero, i.e. the (ideal) calibration parameters when the field value is known at the precise location of the sensor. It is assumed to satisfy the following equation

$$A_2^* y_2(i) + B_2^* = H(x_2(i)), \quad \forall i = 1, \dots, N$$

A substitution in Equation (E.2) yields

$$f_1(A_2, B_2) = \sum_{i=1}^N \|(A_2 - A_2^*) y_2(i) + (B_2 - B_2^*) - \epsilon_{12}(i)\|^2$$

Consider

$$E = \begin{pmatrix} y_2(1)^T & 0 & 0 & \\ 0 & y_2(1)^T & 0 & I_3 \\ 0 & 0 & y_2(1)^T & \\ \vdots & \vdots & \vdots & \vdots \\ y_2(N)^T & 0 & 0 & \\ 0 & y_2(N)^T & 0 & I_3 \\ 0 & 0 & y_2(N)^T & \end{pmatrix}$$

and, with $A' = A - A^*$ and $B' = B - B^*$, consider the vector of their components

$$Z' = (a'_{1,1} \ a'_{1,2} \ a'_{1,3} \ a'_{2,1} \ \dots \ a'_{3,3} \ b'_1 \ b'_2 \ b'_3)^T$$

Then, with

$$\Sigma = (\epsilon_{12}(1)^T \ \epsilon_{12}(2)^T \ \dots \ \epsilon_{12}(N)^T)^T + o(\delta)$$

the cost function to be minimized can now be written

$$f_1 = \|EZ' - \Sigma\|^2$$

which is minimized by

$$Z' = (E^T E)^{-1} E^T \Sigma \quad (\text{E.3})$$

This last equation simply implies that the coefficients of the calibration parameters (A_2, B_2) differ from the optimal ones (A_2^*, B_2^*) (determined when the gradient of the sensed field is zero) by terms that are proportional to $\left\| \frac{\partial H}{\partial X} \right\|$.

E.3.2 Method 2

In the second method, both sensors are first calibrated separately before the harmonization step is performed. This requires two sets of data instead of a single one. The first set is obtained by rotating the system around magnetometer 1 and is used to calibrate this magnetometer, whereas the second set of data is acquired when rotating the whole system around magnetometer 2 in order to calibrate it. Of course, this procedure is more time-consuming, but it cancels the impact of the disturbances of the sensed field onto the separate calibration of the sensors. Yet, the following harmonization step still suffers from the presence of a gradient, because the two distinct sets of data under consideration are slightly inconsistent. Further, we shall note that, in view of practical implementation, this method has two drawbacks. First, the time spent to acquire data for the calibration phase is proportional to the number of sensors in the array (which can be as large as 9 in the application considered in Chapter 5). Including the necessary position shifts of the center of rotation of the whole system, this tedious work can take several hours. Secondly, it is difficult to perform the full rotations exactly around the center of each of the sensors, especially with custom built systems.

For these two reasons, we often prefer to leave out this second method in practical applications.

E.3.3 Global iterative method

A last method is the one presented in details in Chapter 4.4. When the second magnetometer does not see a field of constant norm during the rotations the error propagates through the formula

$$\left(\frac{y_{1,k}(i) + y_{2,k}(i)}{2 \cdot \|y_{1,k}(i) + y_{2,k}(i)\|} \right) = H(x_2(i)) + \epsilon_{2,k}(i)$$

where $\epsilon_{2,k}(i)$ vanishes when $x_2(i) = x_1(i)$. Both magnetometers are thus impacted by the sensed field disturbances in a way similar to magnetometer 2 in method 1 (but with a lower magnitude because of the averaging).

E.3.4 Comparison of the proposed methods

Method 1 leads to the quickest computation among the three candidate methods. It requires only one set of experimental data. However, the sensor taken as reference plays a special role. Changing this reference sensor leads to different calibration parameters. Method 2 is the longest one to put into practice: one set of data has to be acquired for each sensor. Moreover, it is difficult to actually make the rotations exactly around one sensor. But, if carefully performed, it can be more accurate, at least regarding the bias. Finally, the iterative

method requires only one set of data but lasts a bit longer than method 1. However, all sensors play similar roles. The method is completely symmetric.

In summary, method 1 or the iterative one can be preferred, to minimize tedious calibration experiments, provided that the gradient of the sensed field remains reasonably small in the area where the sensors are to be calibrated. The effects of this gradient is also diminished if the sensors are located close to one another, as shown in Equation (E.3), though this is not always possible to set them up like this in practice. With these methods, an array of sensors can be efficiently and quickly calibrated using a single acquisition of data. A pictorial representation of the calibration results for method 1 is presented in Figure E.2. In this simplified planar scheme, two sensors are considered and a full rotation is performed. Raw data which suffer from bias and misalignments take the form of two ellipses. The first sensor, which is the one around which the rotation is performed, can be completely calibrated. This yields a circle of calibrated measurements. On the other hand, due to presence of a non-zero gradient of the sensed field, the data of the second sensor can not be perfectly calibrated. This results is a *close to circular set of* calibrated data. The results presented here were obtained in simulation. The errors have been magnified to stress the role of the field disturbances.

Appendix F

A Kalman filter for attitude determination

Un filtre de Kalman pour la détermination d'attitude

In this section, we detail an algorithm to estimate the attitude of a rigid body from two or three sources of measurements. In the case where accelerometers and gyroscopes are used, only two of three attitude angles can be obtained. As is well known (see Wahba's problem [113] and a survey of solutions [59, 60] for a complete description), a second independent vector measurement is needed to fully determine the orientation. This very simple algorithm, which is presented here in a tutorial spirit, is the basis of many other implementations accounting for biases and misalignments, models of noises, nonlinearities. . . Extensions and other approaches are presented in [27, 75]. Magnetometers are often added to estimate the heading. However, their use in building where there are magnetic disturbances can reveal erroneous. This case of particular interest is addressed in [3].

The principles of the discussed attitude estimation problem (i.e. the orientation of the body frame \mathcal{R}_b with respect to \mathcal{R}_i) is to present the attitude by a quaternion $Q = (q_0 \ q_1 \ q_2 \ q_3)^T$ (see [99] for alternate representations of the attitude) and to assume that accelerometers embedded onto the rigid body measure the opposite of the gravity vector $(0 \ 0 \ g)^T$, here expressed in \mathcal{R}_i , projected onto \mathcal{R}_b . The embedded gyroscopes, whose reading are $(p \ q \ r)^T$, are used to account for the rotation dynamics.

The model of the rigid body rotation is

$$\dot{Q} = \frac{1}{2}M(p, q, r)Q$$

where

$$M = \begin{pmatrix} 0 & -p & -q & -r \\ p & 0 & r & -q \\ q & -r & 0 & p \\ r & q & -p & 0 \end{pmatrix}$$

The accelerometer readings are

$$Y = -R(Q) \begin{pmatrix} 0 \\ 0 \\ g \end{pmatrix}$$

where

$$R(Q) = \begin{pmatrix} 2 \cdot (q_0^2 + q_1^2) - 1 & 2 \cdot q_1 \cdot q_2 + 2 \cdot q_0 \cdot q_3 & 2 \cdot q_1 \cdot q_3 - 2 \cdot q_0 \cdot q_2 \\ 2 \cdot q_1 \cdot q_2 - 2 \cdot q_0 \cdot q_3 & 2 \cdot (q_0^2 + q_2^2) - 1 & 2 \cdot q_2 \cdot q_3 + 2 \cdot q_0 \cdot q_1 \\ 2 \cdot q_1 \cdot q_3 + 2 \cdot q_0 \cdot q_2 & 2 \cdot q_2 \cdot q_3 - 2 \cdot q_0 \cdot q_1 & 2 \cdot (q_0^2 + q_3^2) - 1 \end{pmatrix}$$

To estimate the attitude using a KF, one simply has to linearize the equations above (dynamics and measurement equation). At the discrete time k , using the time step δt , consider $\hat{X}_p[k]$ the vector containing estimates at index k of the quaternion Q , $\Sigma_p[k]$ a 4×4 matrix being the estimate of the covariance of $\hat{X}_p[k]$, $\hat{X}_e[k]$ a vector of the same size as $\hat{X}_p[k]$ and $\Sigma_e[k]$ a matrix of the same size as $\Sigma_p[k]$.

Update (propagate) \hat{X}_p and Σ_p as follows

$$\begin{aligned} \hat{X}_p[k+1] &= (I + A \cdot \delta t) \hat{X}_e[k] \\ A &= \frac{1}{2} M(p, q, r) \\ \Sigma_e[k+1] &= \left(\Sigma_p[k+1]^{-1} + C^T M_\rho^{-1} C \right)^{-1} \end{aligned}$$

M_ρ is a constant symmetric semi-definite 4×4 matrix standing for the covariance of uncertainties on the dynamics equation.

Update (using measurements)

$$K = \Sigma_p[k+1] C^T (C \Sigma_p[k+1] C^T + M_\rho)^{-1}$$

M_ρ is a constant symmetric definite 3×3 matrix standing for the covariance of uncertainties on the measurements

$$C = -2 \cdot g \cdot \begin{pmatrix} -q_2 & q_3 & -q_0 & q_1 \\ q_1 & q_0 & q_3 & q_2 \\ 2q_0 & 0 & 0 & 2q_3 \end{pmatrix}$$
$$\hat{X}_e[k+1] = \hat{X}_p[k+1] + K \left(Y - C \hat{X}_p[k+1] \right)$$
$$\Sigma_e[k+1] = \left(\Sigma_p[k+1]^{-1} + C^T M_\rho^{-1} C \right)^{-1}$$

Appendix G

Details on Adams-Bashforth integration scheme

Détails sur le schéma d'intégration d'Adams-Bashforth

In this Appendix, we detail the integration scheme used for discrete time implementation of the filter equations. A point of particular interest is that the risks of divergence that normally arise with explicit or implicit Euler schemes applied to rotational dynamics (producing on the simple equation $\dot{X} = -\Omega \times X$ a diverging or a converging spiraling trajectory, e.g. with $\Omega = \begin{pmatrix} 0 & 1 \\ -1 & 0 \end{pmatrix}$), the integration scheme must be of order higher than 1.

Due to its ease of implementation, the Adams-Bashforth scheme [1, §25.5.4, p.896] is a very good choice. Analytic formulas for the weight of past values of the derivatives are available in the literature, e.g. in [1, §25.5.4, p.896], but when one sample is missing, as can occur in real-time implementation, other formulas, dealing with non-uniform time grids, can be used. They are derived here.

Adams-Bashforth integration scheme uses an extrapolation technique from the knowledge of past values of the right-hand side of the differential equation.

G.1 General principle

Consider a function y and its time derivative f such that

$$\dot{y}(t) = f(t)$$

One wishes to extrapolate the value of y at time t_4 from $y(t_3) = y_3$ with $t_3 < t_4$, and past values of f at time t_0, t_1, t_2 and t_3 , i.e. estimate the integral

$$y_4 = y_3 + \int_{t_3}^{t_4} f(t)dt \tag{G.1}$$

In the Adams-Bashforth integration scheme, the function f is first approximated by a Lagrange polynomial of degree 4 (in the case of the integration scheme of the 4th order), denoted $p(t)$. It takes the values $f_0 = f(t_0)$, $f_1 = f(t_1)$, $f_2 = f(t_2)$ and $f_3 = f(t_3)$ at previous times $t_0 < t_1 < t_2 < t_3$. y_3 , f_0 , f_1 , f_2 and f_3 are assumed to be known.

The Lagrange polynomial writes

$$p(t) = \sum_{i=0}^3 f_i \cdot \left(\prod_{j=0, j \neq i}^3 \frac{t - t_j}{t_i - t_j} \right)$$

Integral (G.1) can thus be approximated by replacing the function $f(t)$ by the polynomial $p(t)$. One has

$$y_4 = y_3 + \int_{t_3}^{t_4} p(t) dt$$

With the notations

$$\beta_i = \prod_{j=0, j \neq i}^3 \frac{1}{t_i - t_j} \quad (\text{G.2})$$

and

$$\alpha_i = \beta_i \cdot \left[\frac{t_4^4 - t_3^4}{4} - \frac{t_4^3 - t_3^3}{3} \cdot \left(\sum_{j=0, j \neq i}^3 t_j \right) + \frac{t_4^2 - t_3^2}{2} \cdot \left(\sum_{j=0, j \neq i}^3 \prod_{k=0, k \neq i, j}^3 t_k \right) - (t_4 - t_3) \cdot \left(\prod_{j=0, j \neq i}^3 t_j \right) \right] \quad (\text{G.3})$$

giving for instance

$$\alpha_0 = \beta_0 \cdot \underbrace{\left[\frac{t_4^4 - t_3^4}{4} - \frac{t_4^3 - t_3^3}{3} \cdot (t_1 + t_2 + t_3) + \frac{t_4^2 - t_3^2}{2} \cdot (t_1 \cdot t_2 + t_2 \cdot t_3 + t_3 \cdot t_1) - (t_4 - t_3) \cdot (t_1 \cdot t_2 \cdot t_3) \right]}_A \quad (\text{G.4})$$

one obtains

$$y_4 = y_3 + \sum_{i=1}^3 \alpha_i \cdot f_i$$

The coefficients β_i , which depends on the time grid, correspond to the denominator of the Lagrange polynomial. They can be computed for any time grid through Equation (G.2) and only serve as intermediate variables in the computation of the coefficients α_i . These coefficients can be computed for any time-grid from Equation (G.3). The computation of one such coefficient will now be exposed in the particular case of a uniform time grid.

G.2 Determining the weights for a regular time grid

Over a regular time grid, one has

$$\delta t = t_4 - t_3 = t_3 - t_2 = t_2 - t_1 = t_1 - t_0$$

Then Equation (G.3) can be rewritten in terms of t_3^1 and δt only. It yields

$$\begin{aligned} \frac{t_4^4 - t_3^4}{4} &= \frac{12 \cdot t_3^3 \cdot \delta t + 18 \cdot t_3^2 \cdot \delta t^2 + 12 \cdot t_3 \cdot \delta t^3 + 3 \cdot \delta t^4}{12} \\ \frac{t_4^3 - t_3^3}{3} \cdot (t_1 + t_2 + t_3) &= \frac{36 \cdot t_3^3 \cdot \delta t - 24 \cdot t_3 \cdot \delta t^3 - 12 \cdot \delta t^4}{12} \\ \frac{t_4^2 - t_3^2}{2} \cdot (t_1 \cdot t_2 + t_2 \cdot t_3 + t_3 \cdot t_1) &= \frac{36 \cdot t_3^3 \cdot \delta t - 54 \cdot t_3^2 \cdot \delta t^2 - 60 \cdot t_3 \cdot \delta t^3 + 12 \cdot \delta t^4}{12} \\ (t_4 - t_3) \cdot t_1 \cdot t_2 \cdot t_3 &= \frac{12 \cdot t_3^3 \cdot \delta t - 36 \cdot t_3^2 \cdot \delta t^2 + 24 \cdot t_3 \cdot \delta t^3}{12} \end{aligned}$$

The factor A in Equation (G.4) thus writes

$$\begin{aligned} A &= \frac{12 \cdot t_3^3 \cdot \delta t + 18 \cdot t_3^2 \cdot \delta t^2 + 12 \cdot t_3 \cdot \delta t^3 + 3 \cdot \delta t^4}{12} - \frac{36 \cdot t_3^3 \cdot \delta t - 24 \cdot t_3 \cdot \delta t^3 - 12 \cdot \delta t^4}{12} \\ &+ \frac{36 \cdot t_3^3 \cdot \delta t - 54 \cdot t_3^2 \cdot \delta t^2 - 60 \cdot t_3 \cdot \delta t^3 + 12 \cdot \delta t^4}{12} - \frac{12 \cdot t_3^3 \cdot \delta t - 36 \cdot t_3^2 \cdot \delta t^2 + 24 \cdot t_3 \cdot \delta t^3}{12} \\ &= \frac{27 \cdot \delta t^4}{12} \end{aligned}$$

On the other hand

$$\beta_0 = \frac{1}{(t_0 - t_1) \cdot (t_0 - t_2) \cdot (t_0 - t_3)} = \frac{-1}{6 \cdot \delta t^3}$$

which finally gives

$$\alpha_0 = \frac{-1}{6 \cdot \delta t^3} \cdot \frac{27 \cdot \delta t^4}{12} = \frac{-9}{24}$$

Coefficients $\alpha_1, \alpha_2, \alpha_3$ can be computed in similar ways. The explicit formula for the 4th order Adams-Bashforth integration scheme is simply (as given in [1, §25.5.4, p.896])

$$\boxed{y_4 = y_3 + \frac{\delta t}{24} \cdot (55 \cdot f_3 - 59 \cdot f_2 + 37 \cdot f_1 - 9 \cdot f_0)}$$

As exposed in [61], the error of the s^{th} order Adams-Bashforth scheme is of order $O(\delta t^s)$.

G.3 Coefficients in case of a missing sample

Equation (G.2) and Equation (G.3) allow to compute the coefficients involved in the integration scheme for any grid. We provide here the result, useful in practice, of a uniform grid where one sample is missing. The position of the missing sample yields different coefficient sets, used the one after the other as the missing sample gets in the past.

Sample missing between t_3 and t_4 In this case, one has $t_3 - t_2 = t_2 - t_1 = t_1 - t_0 = \delta t$ but $t_4 - t_3 = 2 \cdot \delta t$, and the corresponding integration scheme is

$$y_4 = y_3 + \frac{\delta t}{3} \cdot (27 \cdot f_3 - 44 \cdot f_2 + 31 \cdot f_1 - 8 \cdot f_0)$$

¹The choice of t_3 is arbitrary, one could have chosen any other point in the time grid.

Sample missing between t_2 and t_3 In this case, one has $t_4 - t_3 = t_2 - t_1 = t_1 - t_0 = \delta t$ but $t_3 - t_2 = 2 \cdot \delta t$, and the corresponding integration scheme is

$$y_4 = y_3 + \frac{\delta t}{96} \cdot (161 \cdot f_3 - 206 \cdot f_2 + 200 \cdot f_1 - 59 \cdot f_0)$$

Sample missing between t_1 and t_2 In this case, one has $t_4 - t_3 = t_3 - t_2 = t_1 - t_0 = \delta t$ but $t_2 - t_1 = 2 \cdot \delta t$, and the corresponding integration scheme is

$$y_4 = y_3 + \frac{\delta t}{144} \cdot (293 \cdot f_3 - 206 \cdot f_2 + 94 \cdot f_1 - 37 \cdot f_0)$$

Sample missing between t_0 and t_1 In this case, one has $t_4 - t_3 = t_3 - t_2 = t_2 - t_1 = \delta t$ but $t_1 - t_0 = 2 \cdot \delta t$, and the corresponding integration scheme is

$$y_4 = y_3 + \frac{\delta t}{96} \cdot (211 \cdot f_3 - 200 \cdot f_2 + 94 \cdot f_1 - 9 \cdot f_0)$$

Appendix H

Publications

Conference paper

- [1] Eric Dorveaux, Thomas Boudot, Mathieu Hillion, and Nicolas Petit. Combining inertial measurements and distributed magnetometry for motion estimation. In *Proc. of the 2011 American Control Conference*, 2011.
- [2] Eric Dorveaux and Nicolas Petit. Harmonization of a multi-sensor navigation system. In *Proc. of the 2nd Indoor Positioning & Indoor Navigation Conference*, 2011.
- [3] Eric Dorveaux, David Vissière, Alain-Pierre Martin, and Nicolas Petit. Iterative calibration method for inertial and magnetic sensors. In *Proc. of the 48th IEEE Conf. on Decision and Control*, pages 8296 –8303, dec. 2009.
- [4] Eric Dorveaux, David Vissière, Alain-Pierre Martin, and Nicolas Petit. Time-stamping for an array of low-cost sensors. In *Proc. of the PDES 2009, IFAC workshop on Programmable Devices and Embedded Systems*, 2009.
- [5] Eric Dorveaux, David Vissière, and Nicolas Petit. On-the-field calibration of an array of sensors. In *Proc. of the 2010 American Control Conference*, 2010.

Journal paper

- [1] Pierre-Jean Bristeau, Eric Dorveaux, David Vissière, and Nicolas Petit. Hardware and software architecture for state estimation on an experimental low-cost small-scaled helicopter. *Control Engineering Practice*, 18(7):733–746, 2010.

Bibliography

- [1] M. Abramowitz and I. Stegun. *Handbook of mathematical functions*. Dover, New York, 1965.
- [2] M. J. Abzug and E. E. Larrabee. *Airplane stability and control*. Cambridge University Press, 2002.
- [3] M. H. Afzal. *Use of Earth's magnetic field for pedestrian navigation*. PhD thesis, Department of Geomatics Engineering, The University of Calgary, 2011.
- [4] Z. Altamimi, P. Sillard, and C. Boucher. Itrf2000: A new release of the International Terrestrial Reference Frame for Earth science applications. *Journal of Geophysical Research*, 107, 2002.
- [5] Analog Devices. *ADIS16405 - Tri-axis inertial sensor with magnetometer*, revision 0 edition, 2009.
- [6] G. Arechavaleta, J.-P. Laumond, H. Hicheur, and A. Berthoz. On the non-holonomic nature of human locomotion: a modeling study. In *Proc. of the 1st IEEE/RAS-EMBS International Conference on Biomedical Robotics and Biomechatronics*, 2006.
- [7] D. Aufderheide and W. Krybus. Towards real-time camera egomotion estimation and three-dimensional scene acquisition from monocular image streams. In *Indoor Positioning and Indoor Navigation (IPIN), 2010 International Conference on*, pages 1–10, sept. 2010.
- [8] R. W. Barnard, K. Pearce, and L. Schovanec. Inequalities for the perimeter of an ellipse. *Journal of Mathematical Analysis and Applications*, 260(2):295 – 306, 2001.
- [9] C. Barton. Revision of International Geomagnetic Reference Field Release. *EOS Transactions*, 77, April 1996.
- [10] R. R. Bate, D. D. Mueller, and J. E. White. *Fundamentals of astrodynamics*, chapter 9.6.4 The Gauss-Jackson method, pages 414–419. Dover Publications Inc., 1971.
- [11] P. Batista, C. Silvestre, and P. Oliveira. Position and velocity navigation systems for unmanned vehicles. *Control Systems Technology, IEEE Transactions on*, 17(3):707–715, may 2009.
- [12] P. Batista, C. Silvestre, and P. Oliveira. Sensor-based complementary globally asymptotically stable filters for attitude estimation. In *Decision and Control, 2009 held*

- jointly with the 2009 28th Chinese Control Conference. *CDC/CCC 2009. Proceedings of the 48th IEEE Conference on*, pages 7563–7568, dec. 2009.
- [13] P. Batista, C. Silvestre, P. Oliveira, and B. Carneira. Accelerometer calibration and dynamic bias and gravity estimation: analysis, design, and experimental evaluation. *IEEE Transactions on Control Systems Technology*, 19(5):1128–1137, 2011.
- [14] M. M. Berry and L. M. Healy. Implementation of Gauss-Jackson integration for orbit propagation. *The Journal of the Astronautical Sciences*, 52(3):331–357, July-September 2004.
- [15] J. Blankenbach and A. Norrdine. Position estimation using artificial generated magnetic fields. In *Indoor Positioning and Indoor Navigation (IPIN), 2010 International Conference on*, pages 1–5, sept. 2010.
- [16] P.-J. Bristeau, F. Callou, D. Vissière, and N. Petit. The navigation and control technology inside the AR.Drone micro UAV. In *Proc. of the 18th IFAC World Congress*, 2011.
- [17] P.-J. Bristeau, E. Dorveaux, D. Vissière, and N. Petit. Hardware and software architecture for state estimation on an experimental low-cost small-scaled helicopter. *Control Engineering Practice*, 18(7):733–746, 2010.
- [18] P.-J. Bristeau and N. Petit. Navigation system for ground vehicles using temporally interconnected observers. In *Proc. of the 2011 American Control Conference*, 2011.
- [19] P.-J. Bristeau, N. Petit, and L. Praly. Design of a navigation filter by analysis of local observability. In *Proc. of the 49th IEEE Conference on Decision and Control (CDC)*, 2010.
- [20] M. Caccamo, T. Baker, A. Burns, G. Buttazzo, and L. Sha. Real-time scheduling for embedded systems. In D. Hristu-Varsakelis and W. S. Levine, editors, *Handbook of networked and embedded control systems*, Boston, Basel, Berlin, 2005. Birkhäuser.
- [21] J. J. Caffery. *Wireless location in CDMA cellular radio systems*. Springer, 2000.
- [22] B. Carlsson, A. Ahlen, and M. Sternad. Optimal differentiation based on stochastic signal models. *IEEE Transactions on Signal Processing*, 39(2):341–353, 1991.
- [23] B. Carlsson, M. Sternad, and A. Ahlen. Digital differentiation of noisy data measured through a dynamic system. *IEEE Transactions on Signal Processing*, 40(1):218–221, 1992.
- [24] N. Castaneda and S. Lamy-Perbal. An improved shoe-mounted inertial navigation system. In *Indoor Positioning and Indoor Navigation (IPIN), 2010 International Conference on*, pages 1–6, sept. 2010.
- [25] A. B. Chatfield. *Fundamentals of high accuracy inertial navigation*, volume 174 of *Progress in Astronautics and Aeronautics Series*. AIAA, 1997.
- [26] D. Choukroun. *Novel methods for attitude determination using vector observations*. PhD thesis, Israel Institute of Technology, 2003.

-
- [27] J. Crassidis, F. Landis Markley, and Y. Cheng. Survey of nonlinear attitude estimation methods. *Journal of Guidance, Control, and Dynamics*, 30(1):12–28, 2007.
- [28] A. Davison and D. Murray. Simultaneous localization and map-building using active vision. *Pattern Analysis and Machine Intelligence, IEEE Transactions on*, 24(7):865–880, jul 2002.
- [29] A. Davison, I. Reid, N. Molton, and O. Stasse. MonoSLAM: real-time single camera SLAM. *Pattern Analysis and Machine Intelligence, IEEE Transactions on*, 29(6):1052–1067, june 2007.
- [30] E. Dorveaux, T. Boudot, M. Hillion, and N. Petit. Combining inertial measurements and distributed magnetometry for motion estimation. In *Proc. of the 2011 American Control Conference*, 2011.
- [31] E. Dorveaux and N. Petit. Harmonization of a multi-sensor navigation system. In *Proc. of the 2nd Indoor Positioning & Indoor Navigation Conference*, 2011.
- [32] E. Dorveaux, D. Vissière, A.-P. Martin, and N. Petit. Iterative calibration method for inertial and magnetic sensors. In *Proc. of the 48th IEEE Conf. on Decision and Control*, pages 8296–8303, dec. 2009.
- [33] E. Dorveaux, D. Vissière, A.-P. Martin, and N. Petit. Time-stamping for an array of low-cost sensors. In *Proc. of the PDES 2009, IFAC workshop on Programmable Devices and Embedded Systems*, 2009.
- [34] E. Dorveaux, D. Vissière, and N. Petit. On-the-field calibration of an array of sensors. In *Proc. of the 2010 American Control Conference*, 2010.
- [35] M. El-Diasty and S. Pagiatakis. A rigorous temperature-dependent stochastic modelling and testing for mems-based inertial sensor errors. *Sensors*, 9(11):8473–8489, 2009.
- [36] D. Elliott. The Euler-Maclaurin formula revisited. *Journal of the Australian Mathematical Society*, B40(E):2776, 1998.
- [37] D. Elliott and E. Venturino. Sigmoidal transformations and the Euler-Maclaurin expansion for evaluating certain Hadamard finite-part integrals. *Numerische Mathematik*, 77:453–465, 1997.
- [38] J. Farrell and M. Barth. *The global positioning system & inertial navigation*. McGraw-Hill Professional, 1999.
- [39] P. Faure. *Navigation inertielle et filtrage stochastique*. Méthodes mathématiques de l’informatique. Dunod, 1971.
- [40] R. Feynman. *Cours de physique: électromagnétisme 1*. InterEdition, Paris, 1979.
- [41] R. Feynman. *Cours de physique: électromagnétisme 2*. InterEdition, Paris, 1979.
- [42] C. Finlay, S. Maus, C. Beggan, T. Bondar, A. Chambodut, T. Chernova, A. Chulliat, V. Golovkov, B. Hamilton, M. Hamoudi, R. Holme, G. Hulot, W. Kuang, B. Langlais, V. Lesur, F. Lowes, H. Lühr, S. Macmillan, M. Mandeia, S. McLean, C. Manoj,

- M. Menvielle, I. Michaelis, N. Olsen, J. Rauberg, M. Rother, T. Sabaka, A. Tangborn, L. Tøffner-Clausen, E. Thébault, A. Thomson, I. Wardinski, Z. Wei, and T. Zvereva. International Geomagnetic Reference Field: the eleventh generation. *Geophysical Journal International*, 183(3):1216–1230, 2010.
- [43] C. Fischer, K. Muthukrishnan, and M. Hazas. SLAM for pedestrians and ultrasonic landmarks in emergency response scenarios. *Advances in Computer, Academic Press, Burlington, MA*, pages 103–160, 2011.
- [44] W. T. Fong, S. K. Ong, and A. Y. C. Nee. Methods for in-field user calibration of an inertial measurement unit without external equipment. *Measurement Science and Technology*, 19(8):085202–+, Aug. 2008.
- [45] C. Foster and G. Elkaim. Extension of a non-linear, two-step calibration methodology to include non-orthogonal sensor axes. In *IEEE Journal of Aerospace Electronic Systems*, volume 44, July 2008.
- [46] E. Foxlin. Pedestrian tracking with shoe-mounted inertial sensors. *IEEE Computer Graphics and Applications*, 25:38–46, 2005.
- [47] M. Gamini Dissanayake, P. Newman, S. Clark, H. Durrant-Whyte, and M. Csorba. A solution to the simultaneous localization and map building (SLAM) problem. *IEEE Transactions on Robotics and Automation*, 17(3):229–241, 2001.
- [48] D. Gebre-Egziabher, G. Elkaim, J. Powell, and B. Parkinson. A non-linear, two-step estimation algorithm for calibrating solid-state strapdown magnetometers. In *8th International St. Petersburg Conference on Navigation Systems (IEEE/AIAA)*, May 2001.
- [49] S. Gezici and H. Poor. Position estimation via ultra-wide-band signals. *Proceedings of the IEEE*, 97(2):386–403, feb. 2009.
- [50] B. Gozick, K. P. Subbu, R. Dantu, and T. Maeshiro. Magnetic maps for indoor navigation. *Instrumentation and Measurement, IEEE Transactions on*, PP(99):1–9, 2011.
- [51] P. D. Groves. *Principles of GNSS, inertial, and multi-sensor integrated navigation systems*. Artech House, 2008.
- [52] J. Guerrieri, M. Francis, P. Wilson, T. Kos, L. Miller, N. Bryner, D. Stroup, and L. Klein-Berndt. RFID-assisted indoor localization and communication for first responders. In *Antennas and Propagation, 2006. EuCAP 2006. First European Conference on*, pages 1–6, nov. 2006.
- [53] F. Gustafsson and F. Gunnarsson. Mobile positioning using wireless networks: possibilities and fundamental limitations based on available wireless network measurements. *IEEE Signal Processing Magazine*, 22(4):41–53, 2005.
- [54] T. Hamel and R. Mahony. Attitude estimation on SO[3] based on direct inertial measurements. In *Proc. of the IEEE International Conference on Robotics and Automation (ICRA)*, 2006.

-
- [55] T. Hamel, R. Mahony, and A. Tayebi. Introduction to the special issue on aerial robotics. *Control Engineering Practice*, 18(7):677 – 678, 2010. Special Issue on Aerial Robotics.
- [56] N. J. Higham. *Functions of Matrices: Theory and Computation*. SIAM, 2008.
- [57] Honeywell. *HMR2300 - Smart digital magnetometer*, 900139 02-04 rev. h edition, 2004.
- [58] B. Horowitz, J. Liebman, C. Ma, T. Koo, A. Sangiovanni-Vincentelli, and S. Sastry. Platform-based embedded software design and system integration for autonomous vehicles. *Proc. of the IEEE*, 91:198–211, January 2003.
- [59] M.-D. Hua. Attitude observers for accelerated rigid bodies based on GPS and INS measurements. In *Decision and Control, 2009 held jointly with the 2009 28th Chinese Control Conference. CDC/CCC 2009. Proceedings of the 48th IEEE Conference on*, pages 8071 –8076, dec. 2009.
- [60] M. D. Hua. *Contributions au contrôle automatique de véhicules aériens*. These, Université de Nice Sophia-Antipolis, Dec. 2009.
- [61] A. Iserles. *A first course in the numerical analysis of differential equations*. Cambridge University Press, 2nd edition, 2008.
- [62] J. D. Jackson. *Classical electrodynamics*. John Wiley & Sons, Inc., 3rd edition, 1999.
- [63] A. H. Jazwinski. Stochastic processes and filtering theory. volume 64 of *Mathematics in Science and Engineering*. Elsevier, 1970.
- [64] C. Jekeli. Precision free-inertial navigation with gravity compensation by an onboard gradiometer. *J. Guidance, Control and Dynamics*, 29(3):704–713, 2006.
- [65] A. Jimenez, F. Seco, J. Prieto, and J. Guevara. Indoor pedestrian navigation using an INS/EKF framework for yaw drift reduction and a foot-mounted IMU. In *Proceedings of the 2010 7th Workshop on Positioning, Navigation and Communication, WPNC'10*, pages 135–143, 2010.
- [66] A. Jouy. Chercheur de nord en milieu perturbé et estimation de déplacement par des mesures électromagnétiques. Rapport de stage recherche, Ecole Polytechnique, September 2010.
- [67] E. Kaplan and C. Hegarty. *Understanding GPS: principles and applications*. Artech House, 2nd edition, 2006.
- [68] M. Kayton and W. R. Fried, editors. *Avionics Navigation Systems*. John Wiley & Sons, Inc., 2nd edition, 2007.
- [69] H. K. Khalil. *Nonlinear systems*. MacMillan, 1992.
- [70] O. Koch. *Body-relative navigation using uncalibrated cameras*. PhD thesis, Massachusetts Institute of Technology, June 2010.
- [71] D. Launer. *Navigation through the ages*. Sheridan House Inc., 2009.

- [72] J. Lenz and A. S. Edelstein. Magnetic sensors and their applications. *Sensors Journal, IEEE*, 6(3):631–649, june 2006.
- [73] J. Lyness. The Euler-Maclaurin expansion for the cauchy principal value integral. *Numerische Mathematik*, 46:611–622, 1985.
- [74] R. Mahony, T. Hamel, and J.-M. Pflimlin. Complementary filter design on the special orthogonal group $SO(3)$. In *Proc. of the 44th IEEE Conf. on Decision and Control, and the European Control Conference 2005*, 2005.
- [75] R. Mahony, T. Hamel, and J.-M. Pflimlin. Nonlinear complementary filters on the special orthogonal group. *Automatic Control, IEEE Transactions on*, 53(5):1203–1218, june 2008.
- [76] R. Mautz. Overview of current indoor positioning systems. *Geodesy and Cartography*, 35(1):18–22, 2009.
- [77] R. Mautz. Survey of optical indoor positioning systems. In *Proceedings of the 2011 International Conference on Indoor Positioning and Indoor Navigation (IPIN)*, 2011.
- [78] J. C. Maxwell. *Treatise on electricity and magnetism*, volume 1 & 2. Oxford, 1904.
- [79] B. Mettler. *Identification modeling and characteristics of miniature rotorcraft*. Boston: Kluwer Academic Publishers, 2003.
- [80] Microstrain. *3DMG-X1 Data communications protocol*, March 2006.
- [81] Motorola. MPC555 / MPC556 user’s manual. User’s manual, Motorola, 2000.
- [82] M. Muffert, J. Siegemund, and W. Förstner. The estimation of spatial positions by using an omnidirectional camera system. In *2nd International Conference on Machine Control & Guidance*, pages 95–104, March 2010.
- [83] A. Mulloni, D. Wagner, I. Barakonyi, and D. Schmalstieg. Indoor positioning and navigation with camera phones. *Pervasive Computing, IEEE*, 8(2):22–31, april-june 2009.
- [84] L. Ojeda and J. Borenstein. Non-GPS navigation for security personnel and first responders. *Journal of Navigation*, 60(3):391–407, September 2007.
- [85] W. Olson and K. Pfitzer. A quantitative model of the magnetospheric magnetic field. *Journal of Geophysical Research A: Space Physics*, 79(25):3739–3748, 1974.
- [86] A. V. Oppenheim and R. W. Schaffer. *Discrete-time signal processing*. Signal Processing Series. Prentice Hall, Englewood Cliffs, NJ, 1989.
- [87] A. Pascoal, P. Oliveira, C. Silvestre, L. Sebastiao, M. Rufino, V. Barroso, J. Gomes, G. Ayala, P. Coince, M. Cardew, A. Ryan, H. Braithwaite, N. Cardew, J. Treppe, and e. a. Seube, Nicolas. Robotic ocean vehicles for marine science applications: the European ASIMOV project. In *Proc. of the IEEE Conference and Exhibition OCEANS 2000 MTS*, volume 1, pages 409–415, 2000.

-
- [88] V. Peterka. Predictor-based self-tuning control. *Automatica*, 20(1):39–50, 1984.
- [89] N. Praly, N. Petit, and J. Laurent-Varin. Using distributed magnetometry in navigation of heavy launchers and space vehicles. In *in Proc. of the 4th European Conference for Aerospace Sciences*, 2011.
- [90] J.-C. Radix. *Techniques inertielles*. Masson, 1972.
- [91] R. Rajamani. *Vehicle dynamics and control*. Birkhäuser, 2006.
- [92] V. Renaudin, M. Afzal, and G. Lachapelle. Complete triaxis magnetometer calibration in the magnetic domain. *Journal of Sensors*, 2010, 2010.
- [93] V. Renaudin, O. Yalak, P. Tomé, and B. Merminod. Indoor navigation of emergency agents. *European Journal of Navigation*, 5(3):36–45, 2007.
- [94] P. Ripka, editor. *Magnetic sensors and magnetometers*. ed. Boston: Artech House, 1. edition, 2001.
- [95] P. Savage. Strapdown sensors. *Strapdown Inertial Sensors, NATO AGARD Lecture Series*, (95), May 1978.
- [96] P. G. Savage. *Strapdown analytics*. Strapdown Associates, Maple Plain, Minn, 2000.
- [97] G. Sechi, M. Buonocore, F. Cometto, M. Saponara, A. Tramutola, B. Vinai, G. Andrè, and M. Fehring. In-flight results from the drag-free and attitude control of COGE satellite. In *Proc. of the IFAC World Congress*, 2011.
- [98] A. Sharif. GPS satellite orbit integration by the Gauss-Jackson process. *Buletin Ukur*, 3:35–48, 1992.
- [99] M. D. Shuster. Survey of attitude representations. *Journal of the Astronautical Sciences*, 41(4):439–517, 1993.
- [100] I. Skog and P. Händel. Calibration of a MEMS inertial measurement unit. In *XVII IMEKO World Congress Metrology for a Sustainable Development*, Sept. 2006.
- [101] I. Skog, J.-O. Nilsson, and P. Händel. Evaluation of zero-velocity detectors for foot-mounted inertial navigation systems. In *Proc. of the 1st Indoor Positioning and Indoor Navigation Conference (IPIN)*, 2010.
- [102] W. F. Storms and J. F. Raquet. *Magnetic field aided indoor navigation*. Master’s thesis, Air Force Institute of Technology, March 2009.
- [103] M. Szczot, M. Serfling, O. Löhlein, F. Schüle, M. Konrad, and K. Dietmayer. Global positioning using a digital map and an imaging radar sensor. pages 406–411, 2010.
- [104] S. Thrun, M. Montemerlo, H. Dahlkamp, D. Stavens, A. Aron, J. Diebel, P. Fong, H. M. Gale, J. and, G. Hoffmann, O. C. Lau, K., M. Palatucci, V. Pratt, P. Stang, S. Strohband, C. Dupont, L.-E. Jendrossek, C. Koelen, C. Markey, C. Rummel, J. van Niekerk, E. Jensen, P. Alessandrini, G. Bradski, B. Davies, S. Ettinger, A. Kaehler, A. Nefian, and P. Mahoney. Stanley: The robot that won the DARPA Grand Challenge. *Journal of Field Robotics*, 23(9):661–692, 2006.

- [105] D. Titterton and J. Weston. *Strapdown inertial navigation technology*. The American Institute of Aeronautics and Astronautics, Reston, USA, 2 edition, 2004.
- [106] N. Tsyganenko. A model of the near magnetosphere with a dawn-dusk asymmetry. *Journal of Geophysical Research A: Space Physics*, 107(A8), 2002.
- [107] B. Vasconcelos, J.F. and Cardeira, C. Silvestre, P. Oliveira, and P. Batista. Discrete-time complementary filters for attitude and position estimation: design, analysis and experimental validation. *IEEE Transactions on Control Systems Technology*, 19(1):181–198, 2011.
- [108] J. Vasconcelos, G. Elkaim, C. Silvestre, P. Oliveira, and B. Cardeira. Geometric approach to strapdown magnetometer calibration in sensor frame. *IEEE Transactions on Aerospace and Electronic Systems*, 47(2):1293–1306, 2011.
- [109] D. Vissière. *Solution de guidage-navigation-pilotage pour véhicules autonomes hétérogènes en vue d’une mission collaborative*. Phd thesis, MINES ParisTech, June 2008.
- [110] D. Vissière, A. P. Martin, and N. Petit. Using magnetic disturbances to improve IMU-based position estimation. In *Proc. of the 9th European Control Conf.*, 2007.
- [111] D. Vissière, A.-P. Martin, and N. Petit. Using spatially distributed magnetometers to increase IMU-based velocity estimation in perturbed areas. In *Proc. of the 46th IEEE Conf. on Decision and Control*, 2007.
- [112] D. Vissière, A.-P. Martin, and N. Petit. Système fournissant la vitesse et la position d’un corps en utilisant les variations du champ magnétique évaluées grâce aux mesures de un ou des magnétomètres et de une ou des centrales inertielles. Patent FR2914739 (A1), 10 2008.
- [113] G. Wahba. Problem 65-1 - A least squares estimate of spacecraft attitude. *SIAM Review*, 7(3):409, 1965.
- [114] Widyawan, M. Klepal, and S. Beauregard. A backtracking particle filter for fusing building plans with pdr displacement estimates. In *Positioning, Navigation and Communication, 2008. WPNC 2008. 5th Workshop on*, pages 207 –212, march 2008.
- [115] Xsens. *MTI - Miniature attitude and heading reference system*.
- [116] N. Zarrouati, M. Hillion, and N. Petit. Velocity estimation using low-quality stereo-vision systems. In *submitted to the 2012 American Control Conference*, 2012.

Navigation Magnéto-Inertielle

Principes et application à un système podométrique indoor

Résumé: Cette thèse présente la technique de navigation magnéto-inertielle (MINAV) qui utilise les perturbations du champ magnétique en complément de capteurs inertiels (accéléromètres et gyromètres) pour la localisation d'un corps rigide en mouvement. On étudie des règles de conception, ainsi que des procédures opératoires nécessaires à la mise en pratique dans des conditions réelles. Un exemple de système complet, le "podomètre magnéto-inertiel", permettant la localisation d'un piéton évoluant dans des zones où le GPS est indisponible, est présenté.

Mots clés: navigation inertielle, navigation dans les bâtiments, positionnement dans les bâtiments

Magneto-Inertial Navigation

Principles and application to an indoor pedometer

Abstract: This thesis presents the magneto-inertial navigation technique (MINAV) using magnetic disturbances and inertial sensors (accelerometers and gyrometers) to address the positioning problem of a rigid body in motion. The manuscript provides design guidelines and procedures enabling the creation of a system implementing this technique in real conditions. An example of operational system, the "magneto-inertial pedometer", providing a GPS-free indoor navigation solution is presented.

Keywords: inertial navigation, indoor navigation, indoor positioning

